Summer 2016

Prediction of distortions and pattern allowances in steel sand castings

Daniel Joseph Galles
University of Iowa

Recommended Citation

Galles, Daniel Joseph. "Prediction of distortions and pattern allowances in steel sand castings." PhD (Doctor of Philosophy) thesis, University of Iowa, 2016.
https://doi.org/10.17077/etd.1vr08qwp

www.manaraa.com

PREDICTION OF DISTORTIONS AND PATTERN ALLOWANCES IN STEEL

SAND CASTINGS

by

Daniel Joseph Galles

A thesis submitted in partial fulfillment
of the requirements for the Doctor of
Philosophy degree in Mechanical Engineering
in the Graduate College of
The University of Iowa

August 2016

Thesis Supervisor: Christoph Beckermann

Graduate College
The University of Iowa
Iowa City, Iowa

CERTIFICATE OF APPROVAL

Ph.D. THESIS

This is to certify that the Ph.D. thesis of

Daniel Joseph Galles

has been approved by the Examining Committee
for the thesis requirement for the Doctor of Philosophy
degree in Mechanical Engineering at the August 2016 graduation.

Thesis Committee: _____
Christoph Beckermann, Thesis Supervisor

_____
H.S. Udaykumar

_____
Jia Lu

_____
Hongtao Ding

_____
Colby Swan

ACKNOWLEDGEMENTS

ABSTRACT

Modeling the thermomechanical behavior of the bonded sands used for steel sand casting is of great importance for the prediction of distortions and pattern allowances. In this study, distortions created by mechanical interactions between the casting and sand mold are measured from two experimental setups and then predicted by finite element stress analyses. The casting geometries involve a hollow cylinder for the first experiment and U-shaped bracket for the second. The temporal evolutions of 1) the cylinder's inner diameter and 2) the gap opening between the bracket legs are measured *in situ* utilizing LVDTs (Linear Variable Differential Transformers) connected to quartz rods. The considerable distortions measured during the cylinder and bracket experiments are mainly caused by core expansion and core restraint, respectively. For the simulations, a one-way temperature-displacement coupling is adopted, in which temperatures are predicted using commercial casting simulation software and then used as inputs for the finite element stress analyses. The steel is modeled as an elasto-visco-plastic material, whereas the Drucker Prager Cap model is employed for the bonded sand. It is found that sand dilation (i.e., the volumetric expansion of a granular media due to a shear force) must be considered for the cylinder experiments. Otherwise, the inner diameter expansion observed during solidification is far under-predicted. For the bracket, a crack plane must be included in the stress simulation model. If not, the outer mold restrains the bracket legs from being pushed outward and distortions are under-predicted. By matching the predicted displacements with the measurements, a constitutive dataset for bonded sands is developed, whose predictive capability is then demonstrated through a case study.

PUBLIC ABSTRACT

Steel thermally contracts during casting. These contractions induce mechanical interactions between the casting and mold, which in turn generate distortions that affect the casting dimensions. The inability to predict these distortions lead to dimensional inaccuracies and cause inefficiencies and waste throughout the casting process. In this study, displacement measurements are taken during casting experiments, which are subsequently used for model validation in a finite element stress analysis. By matching the finite element predictions with the measurements, the model is calibrated to simulate industrial casting processes and predict casting dimensions.

TABLE OF CONTENTS

LIST OF TABLES

Table

LIST OF FIGURES

Figure

vii

CHAPTER 1: INTRODUCTION AND LITERATURE REVIEW

1.1 Motivation and Literature Review

During sand casting, mechanical interactions between the casting and mold generate distortions, which in turn influence pattern allowances (*PA*):

$$PA[\%] = \frac{feature\,length_{initial} - feature\,length_{final}}{feature\,length_{initial}} \times 100 \qquad [1]$$

In Eq. [1], *feature length* is the dimension for a particular feature. The *initial* and *final* subscripts refer to the pattern and casting, respectively. In the absence of distortions, pattern allowances are determined solely by thermal strains and commonly referred to as the patternmaker's shrink (e.g., the patternmaker's shrink is approximately 2.1 % for steel), which is commonly used during pattern design as a first estimate to predict casting dimensions. From this viewpoint, distortions can be defined as deviations from the patternmaker's shrink. Examples of these deviations are illustrated in Figure 1.1, where measured pattern allowances from numerous castings are plotted over a range of feature lengths (taken from Voigt [1]). The considerable scatter of pattern allowances seen in the figure demonstrates that, due to the influence of distortions, the patternmaker's shrink cannot reliably predict pattern allowances. Therefore, another strategy is needed.

Distortions create dimensional inaccuracies in the as-cast part, which in turn lead to inefficiencies and waste throughout the casting process. For example, patterns are designed using a time-consuming trial-and-error method in which several design iterations may be needed to achieve the desired casting dimensions. Also, distortions are sensitive to process conditions (e.g., packing density of the mold and cores), causing variations in pattern allowances that may require post-casting operations such as welding or grinding. Furthermore, distortions occurring near the end of solidification may generate cracks, necessitating that the casting be scrapped. Thus, minimizing the uncertainties associated with distortions will not only improve quality but also have a positive economic impact on

www.manaraa.com

industry.

Distortions are created by several physical phenomena, including uneven cooling, mold (or core) restraint, and mold (or core) expansion. Uneven cooling occurs in castings with different section thicknesses. The thinner sections of the casting cool (and thus contract) faster than the thicker sections, generating stresses and associated distortions. Mold restraint constrains thermal contractions in the casting and generates distortions at times ranging from the end of solidification until shakeout. The influence of mold restraint is a well-known problem that has been the focus for previous *in situ* experimental studies [2-7]. The studies usually involved casting a slender bar with a flanges on both ends to induce mold restraint. The experiments were carried out with different metals (steel [2], grey iron [3], ductile iron [4], and aluminum [5,6]) and bonded sands (sodium silicate [3-5], furan [6], and green sand [3-5]). In addition, Monroe and Beckermann [7] studied the effect of mold restraint on hot tears by casting a T-shaped bar in a no-bake sand mold.

In contrast to mold restraint, mold expansion occurs at early casting times, shortly after filling. Because the casting is mostly liquid, the sand mold can easily expand into the mold cavity and reduce the casting volume. This expansion is not only due to thermal expansion of the sand, but also dilation, which is the volumetric expansion of a granular material due to a shear force. Dilative behavior is illustrated in Figure 1.2; the initial state of dense sand contains small air voids between the grains (Figure 1.2(a)). After a shear force is applied, however, the irregularly-shaped sand grains translate and/or rotate and cause the voids to grow, resulting in volumetric expansion of the sand aggregate (Figure 1.2(b)). Peters et al. [8] studied mold expansion through *in situ* casting experiments in which a hollow cylinder was produced using silica and zircon sand cores. Distortions were attributed to thermal expansion of the bonded sands as well as core restraint. However, dilation was not considered.

Computational advances in recent years have stimulated the development of complex constitutive models capable of predicting distortions and pattern allowances for

2

castings of arbitrary size and shape. The accuracy of such models, however, remains uncertain, due in part by the limited availability of realistic mechanical properties and model parameters. This is particularly true at high temperatures where the majority of distortions can be expected to occur. These deficiencies have spurred researchers to study high-temperature properties of bonded sands, including compressive strength [9], tensile strength [10], and elastic modulus [11]. Compressible materials such as sand should be modeled using a constitutive law that considers pressure-dependent yield behavior. This added complexity introduces extra parameters that must be determined through additional testing. The only high-temperature parameters for such models were determined by by Saada et al. [12], who performed triaxial, uniaxial compression, isotropic compression, and die pressing tests on green sand at elevated temperatures to determine parameters for Cam Clay and Hujex constitutive models.

In spite of the contributions from previous studies, the capability of stress analyses to accurately predict distortions and pattern allowances for production castings remains uncertain due in part to the extreme conditions encountered during casting. In particular, the high heating rates near the mold-metal interface cannot be recreated by mechanical tests. Thus, data from these tests may not be appropriate for stress modeling of casting processes. Thole and Beckermann [11] reported significant variations in the elastic modulus for heating rates ranging from 0.8ºC/min to 8ºC/min. In reality, however, heating rates in the bonded sand within a few millimeters of the mold-metal interface can reach several hundred ºC/min. For this reason, the calibration of computational models with data from *in situ* experiments is preferable to calibration from mechanical testing.

1.2 Objective of Present Study

In this study, *in situ* casting experiments involving a hollow cylinder and U-shaped bracket are performed and then simulated in order to predict distortions and pattern allowances in steel sand castings. During both sets of experiments, the temporal evolution

of selected casting features are measured *in situ* by utilizing LVDTs (Linear Variable Differential Transformers) connected to fused quartz rods. In addition, temperatures are measured in the castings, molds, and cores. For the cylinder experiments, distortions are generated by core expansion during solidification. For the bracket experiments, distortions are generated mainly at later times, as the mold restrains thermal contractions in the bracket.

For the simulations, distortions are predicted using a one-way temperature-displacement coupling. Temperatures are calculated first using casting simulation software and then inputted into a finite element stress analysis. The steel is modeled using an elasto-visco-plastic constitutive law, whose parameters were calibrated in a previous study [13]. The bonded sands are modeled using the Drucker-Prager Cap (DPC) constitutive law. Mechanical properties are taken from the literature or estimated through room temperature mechanical testing. By matching the measured and predicted feature lengths for the cylinder and bracket experiments, a constitutive dataset is developed that can be used to predict pattern allowances for production steel sand castings. This capability is then demonstrated through a case study.
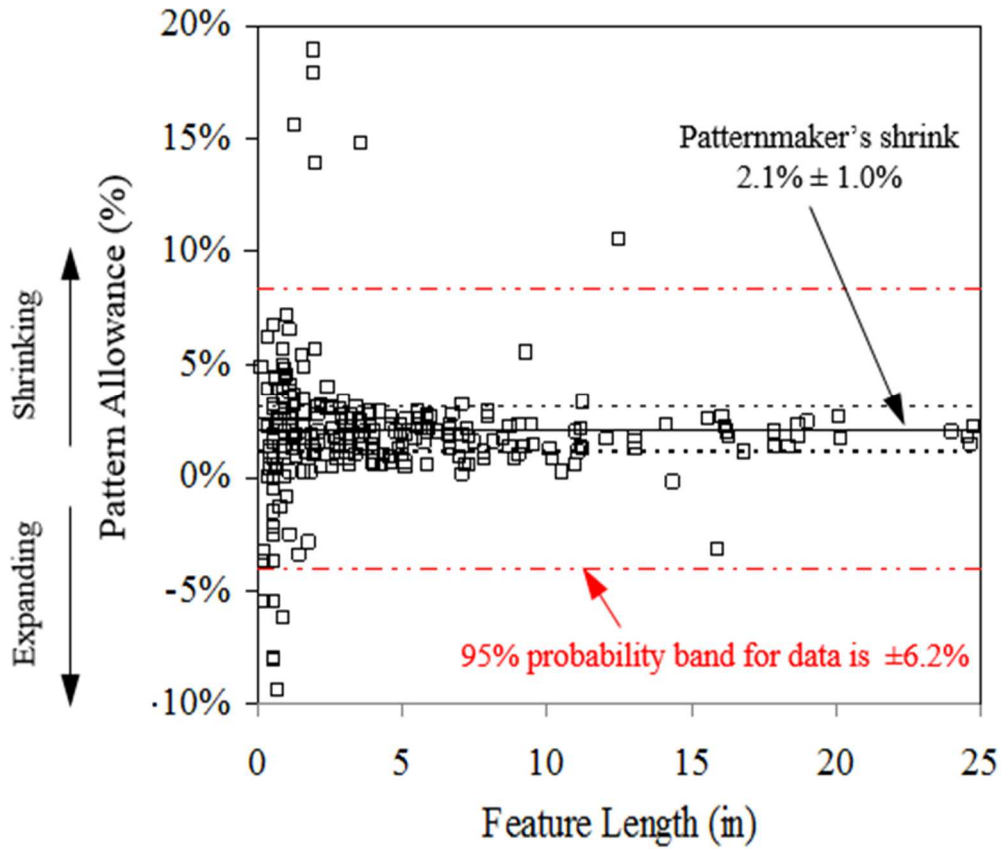
Figure 1.1.   Measured pattern allowances plotted as a function of feature length (taken from Voigt [1]). The scatter in the data demonstrates the effect of distortions.

5

a) Undisturbed state   b) Dilated state
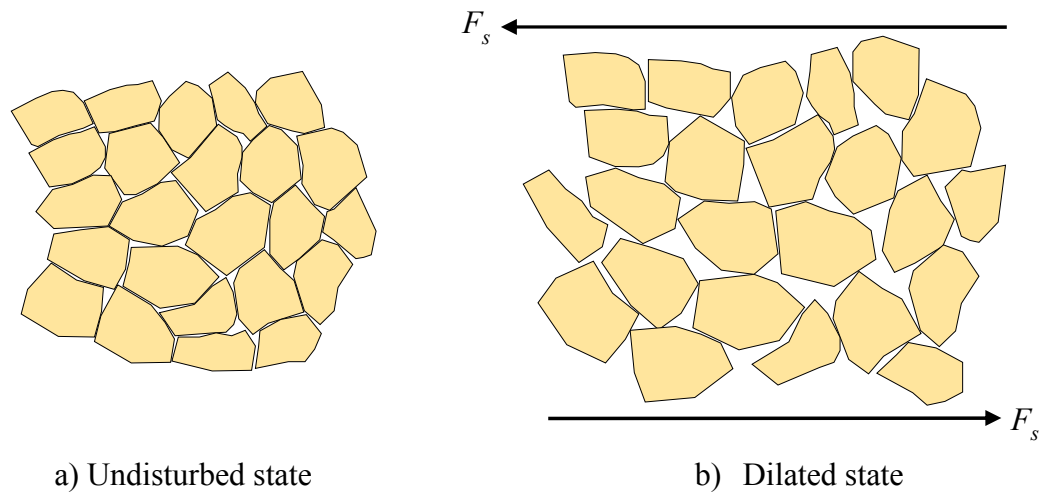
Figure 1.2.   Sand dilation. After a shear force, F_s, is applied to the undisturbed state (a), the voids between sand grains increase, resulting in dilation (i.e., volumetric expansion of the sand aggregate), as shown by the dilated state (b).

CHAPTER 2: DESCRIPTION OF EXPERIMENTS

2.1 Introduction

In order to quantify distortions, two *in situ* casting experiments were designed. For the first experiment, a hollow thick-walled cylinder was produced to investigate the effect of core expansion during solidification. The second experiment involved a U-shaped bracket, from which distortions were created primarily by mold restraint. The experimental setups, casting procedure, and results are described in this chapter.

2.2 Experimental Setup

2.2.1 Thick-walled Cylinder

The casting geometry (50 mm ID × 125 mm OD × 100 mm height) and experimental setup for the thick-walled cylinder are shown in Figure 2.1(a) and (b), respectively. The outer mold dimensions are 280 mm (length) × 280 mm (width) × 75 mm (height) for the cope and 280×280×200 for the drag. Experiments were conducted using cores built with either silica or zircon sand. The choice of these two materials was based on their vastly different thermal expansion coefficients.

The change in the inner diameter at the mid-height of the cylinder was continuously measured by utilizing two identical assemblies consisting of a quartz rod, quartz tube, and LVDT. One end of the quartz rod was flattened into a disc (7 mm in diameter) using an oxy-acetylene torch and inserted through pre-drilled holes in the drag and core. The disc was butted to the outer diameter of the core, as shown in Figure 2.1(b). In order to transmit displacement, the quartz rod passed through a quartz tube, which traversed the mold cavity. The other end of the quartz rod was attached to an LVDT, which continuously measured the displacement from one side of the inner diameter. The other assembly measured displacement on the opposite side of the cylinder. The LVDT measurements were added together to calculate the temporal evolution of the inner diameter. It is obvious from Figure 2.1(b) that both LVDT measurements could not be

7

taken at the same height. Therefore, one measurement was taken approximately 5 mm above the cylinder mid-height, while the other was taken 5 mm below the mid-height.

Temperatures were measured at several locations; type K thermocouples were inserted through the bottom of the drag and into the core at radial distances of 6, 9, 15, and 25 mm from the vertical core-casting interface. Also, the thermocouples were staggered circumferentially to minimize the influence from other thermocouples. Finally, a type B thermocouple was encased in a quartz tube and inserted into the mold cavity to measure the temperature of the steel.

To build the molds (i.e., cope and drag) and silica sand cores, Unimin® IC55 silica lake sand was bonded with a phenolic urethane no-bake (PUNB) binder system. The binder (1.25% of mold weight) was mixed using a 55:45 ratio of part 1 (PEPSET® 1000) to part 2 (Techniset® 6435). The zircon cores were created with zircon sand using the same PUNB binder system and part 1/part 2 ratio used for the silica sand. The cope and drag were hand packed, whereas the cores were manually rammed. The core weights varied less than 0.5% among all cylinder experiments.

In total, 5 cylinders of each core type were produced (10 cylinders in total). For the first 4 cylinders, displacement was measured, as well as temperatures in the steel and at the 25 mm location in the core. For the final cylinder of each core type, no displacement or temperatures in the steel were recorded; only temperatures at the 4 core locations (shown in Figure 2.1(b)) were measured.

2.2.2 U-shaped Bracket

The geometry and experimental setup for the U-shaped bracket is shown in Figure 2.2(a) and 3.2(b), respectively. The outer mold dimensions are 254 mm (length) × 254 mm (width) × 75 mm (height) for the cope and 254×254×230 for the drag. In total, 4 brackets were cast. A simple gating system consisting of a sprue (25 mm radius × 50 mm height) and pouring cup (which also served as a feeder) was utilized.

8

Displacement was measured by utilizing same LVDT-quartz rod assemblies used in the cylinder experiments. The ends of the quartz rods were bulged into spherical shapes (to firmly anchor the rods into the steel and eliminate any slippage) using an oxy-acetylene torch and inserted through pre-drilled holes in the drag (at the casting mid-plane) and extended approximately 3 mm into and 5 mm above the bottom of the mold cavity. As in the cylinder experiments, the LVDT measurements were then added to calculate the temporal evolution of the distance between the bulged ends of the quartz rods, henceforth known as the "outer length" (see Figure 2.2(b)).

Temperatures were measured at the vertical casting mid-plane. Type K thermocouples were inserted midway between the bracket legs at 25, 50, 75, and 100 mm from the bottom horizontal casting surface, as shown in Figure 2.2(b). Additionally, a type B thermocouple was encased in a quartz tube and inserted underneath the sprue, albeit slightly offset to prevent inertial forces from molten stream to potentially break the quartz tube during filling.

The molds were built using the same materials that were used for the cylinder experiments (Unimin® IC55 silica lake sand bonded with a PUNB binder system). The drag was constructed as a single piece and hand packed; hence, no core was used.

2.3 Casting Procedure

Experimental casting trials were performed at the University of Northern Iowa's Metal Casting Center. The target chemistry was ASTM A216 grade WCB carbon steel. The castings were poured from a 250 lb heat and prepared in an induction furnace. Because of the heat loss encountered during the transfer from the furnace to pouring ladle, the molten steel was heated to approximately 1700°C. The castings were poured within four hours after building the molds. Immediately before pouring, any slag was removed from the ladle. For the cylinder experiments, the liquid steel was transferred from the pouring ladle to a smaller hand-held ladle and then poured directly into the mold cavity, after which

the cope was placed on top of the drag. This methodology was utilized to avoid additional mold-metal interactions from the sprue. For the bracket experiments, the castings were poured directly from the pouring ladle into the pouring cup.

2.4 Experimental Results

2.4.1 Thick-walled cylinder

Temperatures are plotted as a function of time in Figure 2.3 for the first 4 silica (red curves) and zircon (blue curves) core experiments. Recall that temperature measurements for these experiments were only taken in the steel and at the 25-mm location in the core (see Figure 2.1(b)). Temperatures for the final silica and zircon core experiments (in which only core temperatures were measured) are plotted vs. time in Figure 2.4. The reference time ($t = 0$) denotes when the molten steel was poured into the mold cavity. The results are plotted on two different time scales. The complete time scale (Figure 2.3(a) and Figure 2.4(a)) represents the approximate time needed to cool the castings to room temperature. The 600 s time scale (Figure 2.3(b) and Figure 2.4(b)) captures the large cooling (heating) rates in the casting (core) during the early stages of casting.

The curves in Figure 2.3 can be explained by several characteristic features. A few seconds after pouring, the steel temperatures rapidly increased to a maximum value of approximately 1550°C. A small temperature decrease of approximately 50°C was then observed, after which the steel temperatures remained nearly constant until 250 s. The minimum cooling rate during this period was due to an abundant release of latent heat that accompanied the onset of solidification. During the later stages of solidification, additional latent heat was released, albeit at a reduced rate. As a result, the cooling rate increased throughout solidification and reached a maximum value at the fully solid temperature. This behavior is illustrated in Figure 2.5, which plots the cooling rate of the steel as a function of temperature. The cooling rate was calculated by taking the discreet time derivative of the measured steel temperatures. The minimum and maximum cooling rates in Figure 2.5

10

correspond to the so-called liquidus (T_{liq}) and solidus (T_{sol}) temperatures, respectively, which define the solidification interval. To obtain representative values, the average solidus ($T_{sol,avg}$) and liquidus ($T_{liq,avg}$) temperatures were calculated and are denoted by horizontal dashed lines in Figure 2.3(a) and vertical dashed lines in Figure 2.5. After solidification, the steel temperatures decreased at an exponentially decaying rate until a solid state phase transformation (at ~4000 s) caused a brief temperature arrest, after which the casting cools to room temperature. The core temperatures in Figure 2.3 generally increase until 600 s, after which the core and steel temperatures are in equilibrium for the remainder of cooling. One characteristic of the core temperature curves is a temperature arrest that occurs when the core reaches 200°C (at 100 s) and is due to the endothermic reaction needed to pyrolize the binder in the core. The temperatures for the other core locations (see Figure 2.4) behavior similarly to those in Figure 2.3. As can be expected, the locations nearest to the core-casting interface heat at a higher rate than those farther away.

For all experiments, excellent repeatability of measured temperatures was observed. In addition, very little difference in temperatures can be seen between the silica and zircon experiments. In other words, all zircon and silica curves from any particular thermocouple location essentially lie on top of each other (see Figure 2.3 and Figure 2.4). This result will be beneficial for the purpose of performing thermal simulations, as one representative set of simulations can be performed for all cylinder experiments.

The changes in the inner diameter measured by the LVDTs are plotted in Figure 2.6(a) and (b) on complete and 600 s time scales, respectively. The complete time scale (40000 s) shows the approximate time needed to cool the casting to room temperature. Shortly after the onset of filling ($t=0$), the inner diameters for the silica cores expanded to a maximum value (ranging from 1.15 mm to 1.3 mm) after 200 s. For the zircon core experiments, the inner diameters in experiments 1 and 2 expanded at approximately the same rate as the silica cores during the initial 25 s, whereas minimal expansion was measured in experiments 3 and 4 during this period. After 25 s, little additional expansion

11

was measured for all zircon core experiments, as the curves are nearly horizontal until 250 s. In general, the zircon cores expanded far less than the silica cores, which can be attributed to differences in the thermal expansion coefficients. Phase transformations in silica sand generate considerably more thermal expansion than zircon, which is stable at all casting temperatures. At approximately 250 s, the inner diameters for all experiments (silica and zircon) began to contract, as solidification neared completion and thermal contractions commenced in the steel. As a result, the inner diameters decreased until a local minimum at approximately 4000 s, followed by a local maximum at roughly 5000 s. This "wiggle" is a manifestation of the volumetric expansion in the casting that accompanies a solid-state phase transformation. After 5000 s, the inner diameters decreased until room temperature. After 250 s, it is evident that all curves in Figure 2.6 contract (or expand during the phase transformation) at the same rate, i.e., all curves are parallel after 250 s. Also, the measured inner diameter contraction in the period $250 < t < 40,000$ s is equal to the patternmaker's shrink for steel. Thus, only thermal strains (i.e., no distortions) contributed to the LVDT measurements after 250 s. This is validated by thermal strain predictions (see Chapter 5). Therefore, it can be concluded from the LVDT measurements all distortions were generated by core expansion before and during solidification. Core restraint did not generate distortions during the cylinder experiments.

In addition to the LVDT measurements, pattern allowances for the inner diameters were measured using Eq. [1] and are shown for the silica and zircon cores in Figure 2.7(a) and (b), respectively. The core (rather than pattern) dimensions were used to calculate pattern allowances in order to remove any variability due to the molding process. Measurements were taken with digital calipers at the feature locations shown in Figure 2.7(c). The pattern allowances are shown as circular symbols, with each color representing a different experiment. Several feature locations contained large cracks or defects that prevented accurate measurement and are not included in the figures. Scatter in the plots can be attributed to surface roughness of the casting and slight differences in the core bulk

12

densities. The average standard deviation for the measurements was approximately 0.15 mm (0.3% *PA*). The dashed horizontal line in Figure 2.7(a) and (b) denote the patternmaker's shrink of the steel (~2.3% due to a circular geometry) and serves as a reference; distortion is quantified as the deviation of any pattern allowance from this line. In general, the silica cores distorted more than the zircon cores, as the silica core pattern allowances are less than those for the zircon cores. Recall that the LVDT measurements revealed that core restraint did not generate distortions. This likely the case at all inner diameter heights. Differences in pattern allowances between the silica and zircon cores can again be attributed to differences in thermal expansion coefficients. The largest core expansions (for both silica and zircon cores) were observed at the mid-height, while smaller expansions occurred near the ends. As a result, the inner diameter surface of the cylinder evolved into a barrel-shaped profile (see Figure 2.7(d)). This transformation can be explained by the local solidification times. At early casting times, the steel was mostly liquid and provided little restraint. As a result, the core easily expanded into the mold cavity. As solidification progressed, the solid fraction increased until the steel reached coherency, which was accompanied by a dramatic increase in steel strength that prevented any farther mold expansion. Since the inner diameter near the top and bottom of the cylinder solidified before than the mid-height inner diameter, the largest expansion should be expected to occur at the mid-height.

Another observation from Figure 2.7(a) and (b) is the large amount of scatter seen in the pattern allowances near the top of the cylinder. Recall that the mold was filled by pouring molten steel directly into the mold cavity (i.e., no gating system was used). In order to prevent spilling steel on the foundry floor, the mold cavity was never completely filled, which resulted in an air gap between the casting and cope. The thickness of this gap varied somewhat among the experiments, which affected cooling rates and associated times to coherency.

Pattern allowances at the mid-height of the cylinder can also be calculated by

13

replacing the numerator in Eq. [1] with the room temperature LVDT measurements (i.e., the change in inner taken at 40000 s in Figure 2.6). These values are shown as triangular symbols in Figure 2.7(a) and (b). Unfortunately, a discrepancy can be seen between the LVDT and calipers pattern allowances, as the LVDT values are significantly higher than those from the calipers. In other words, the calipers measured more core expansion than the LVDTs. The LVDT measurements after 300 s (see Figure 2.6) are credible based on their repeatability. Therefore, the discrepancy presumably occurred during the initial 300 s. Most likely, the quartz rods were not embedded in the mostly liquid steel at early times and "slipped". As a result, some amount of core expansion was not measured. To remedy this, the LVDT measurements in Figure 2.6 were shifted upwards so that the LVDT and calipers pattern allowances coincided. The adjusted curves are shown in Figure 2.8. Note that the circular symbols on the secondary vertical axis in Figure 2.8(a) represent the calipers measurements. Then, the LVDT curves were modified during the initial 100 s to smoothly increase from zero to the shifted measurements which are shown as dashed lines in Figure 2.8(b). The resulting curves will be used below to validate the stress model predictions.

2.4.2 U-shaped Bracket

Temperatures for the brackets are plotted as functions of time in Figure 2.9 on 3 time scales. As in the cylinder experiments, the complete time scale represents the time needed to cool the casting to room temperature. Temperatures are also presented on two additional time scales.

In general, the temperature curves are similar to those from the cylinder experiments. The characteristic features that were observed for the cylinder experiments are also seen in the bracket experiments. From the cooling curves (see Figure 2.10), average liquidus temperatures (T_{liq} =1500°C) and solidus temperatures (T_{sol} =1390°C) were determined as in the cylinder experiments.

14

The LVDTs measured the change in outer length (see Figure 2.2(b)) and are plotted in Figure 2.11 on complete, 5000 s, and 1000 s time scales. For experiment 3 (green curve), a quartz rod failed at approximately 1000 s. After this time, the curve was recreated using data from experiment 1 and is represented by a dashed line.

The decrease in outer length (ranging from 0.1 to 0.4 mm for all brackets) that occurred during the initial 50 s is due to mold expansion into the mold cavity. After 100 s, the LVDT curves increase until 1000 s, as the core acted as a lever and pushed the legs outward. Complete solidification of the bracket (denoted by the vertical dashed line in Figure 2.11(c)) was approximated from the cooling curves to be 325 s, after which the bracket legs were pushed outward by roughly 0.5 mm. At approximately 1000 s, the outer length began to decrease, as the cooling steel had sufficiently increased in strength to overcome the core restraint and pull the bracket legs inward. This decrease continued until a local minimum, which denotes the onset of the solid state phase transformation. The subsequent increase was the result of the volumetric expansion in the steel that accompanies the transformation. The end of the transformation is manifested as a local maximum in the curves, after which the outer lengths decreased monotonically until room temperature. The beginning and end of the solid state phase transformation for experiment 1 are denoted as vertical dashed lines. Depending on the experiment, the time at the onset and duration of the transformation varied, which can be attributed to differences in casting chemistries. After the solid state transformation was complete, the steel had considerably strengthened and the core restraint could no longer induce plastic strains in the casting. As a result, all ensuing measurements were thermal strains.

Pattern allowances for the brackets are shown in Figure 2.12(a). Measurements were taken on three planes (see Figure 2.12(b)) for the leg thickness (L), gap opening (G), and outer length (O). The subscripts in the figure refer the bottom (b), middle (m), and top (t) of the bracket legs. The measured pattern allowances are also distinguished by whether they were measured on the inner or outer planes. In the absence of mold and core effects,

15

only thermal strains will contribute to dimensional changes in the casting. In such a case, all pattern allowances should be equal to the patternmaker's shrink, which is denoted by the horizontal dashed line in Figure 2.12(a). The average pattern allowances for the leg thicknesses are 3.9, 4.6, and 5.4 percent for the bottom, middle, and top of the legs, respectively. These large values coincide with the negative change in outer length during the initial 100 s shown in Figure 2.11(c) and are the result of mold and core expansion into the mold cavity. It is important to note that these large values are not associated with plastic strains. Immediately after pouring, the steel has not yet reached coherency and cannot transmit stresses. The molten steel is simply displaced by expansion of the mold and core. Once coherency occurs, the steel constrains any further mold expansion. Because the outer planes solidify before the inner planes, the mold has less time to expand and as a result, the average pattern allowances (for the leg thickness) on the outer planes are less than those for the inner plane. The leg thicknesses (L) contain considerably more scatter than the gap opening (G) and outer length (O). This can be attributed to the surface roughness of the casting, which leads to variations in the measurements. The magnitude of these variations should be similar for L, G, and O. However, since the pattern dimension of L is much smaller than G and O, these variations lead to more scatter in L. The pattern allowances for the gap opening average -2.2%, -0.8%, and 0.5 % at the bottom, middle, and top, respectively. This result makes sense; assuming the legs remain mostly planar, the bottoms should push out more than the middle, and the middle should push out more than the top. Finally, the pattern allowances for the outer length averaged 0.1%, 1.3%, and 2.4% at the bottom, middle, and top. Although these values are somewhat close to the patternmaker's shrink line, it is clear from Figure 2.12(b) that the outer length is a combination of the gap opening and leg thickness ($O = 2L + G$). Essentially, the pattern allowances of the leg thickness and gap opening cancel each other out, resulting in a pattern allowance for the outer length that is close to the patternmaker's shrink.

From Figure 2.2(b) and Figure 2.12(b), it can be seen that the feature O_b is the same

16

dimension that was measured by the LVDTs. These values are compared in Figure 2.13. Small discrepancies can be seen, particularly for brackets 1, 2, and 3. As in the cylinder experiments, this discrepancy can be attributed to slippage between the quartz rods and casting during solidification. To remedy this, the LVDT measurements will be adjusted slightly during the initial 100 s to match the calipers measurements. These adjustments, however, are minor and do not affect the overall shapes of the measurement curve. Through these adjustments, the variation in the initial decrease in the outer lengths that occurred during the initial 50 s (see Figure 2.11(c)) is minimized. The adjusted curves can be seen in all subsequent LVDT bracket measurements (see Chapter 5).
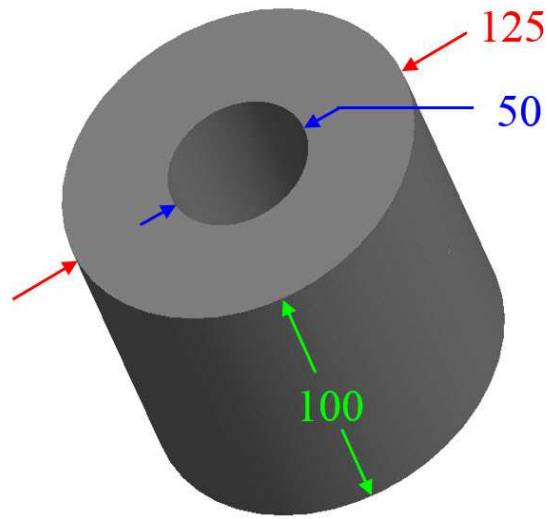
(a) Casting geometry
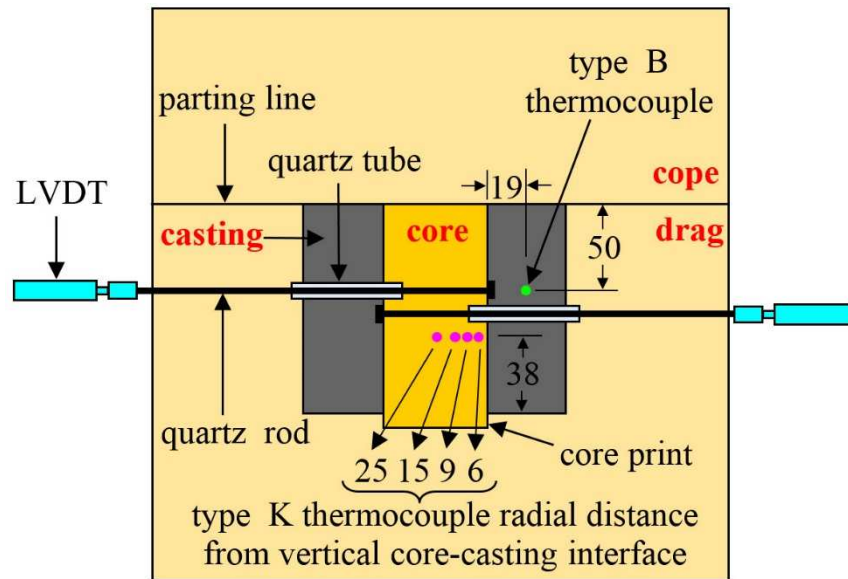
(b) Experimental setup

Figure 2.1.   Casting geometry (a) and experimental setup at the casting mid-plane (b) for cylinder experiments. Units in mm.
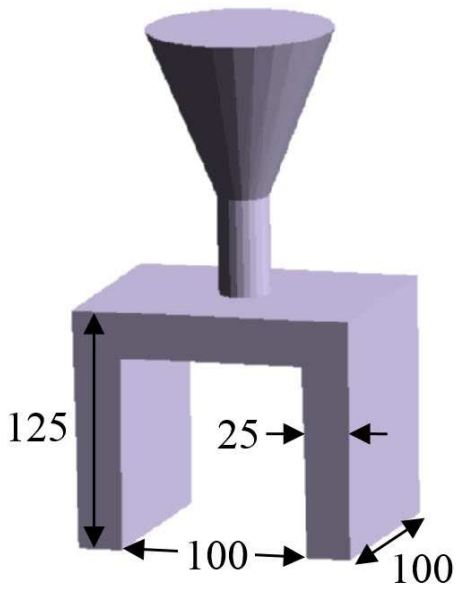
(a) Casting Geometry
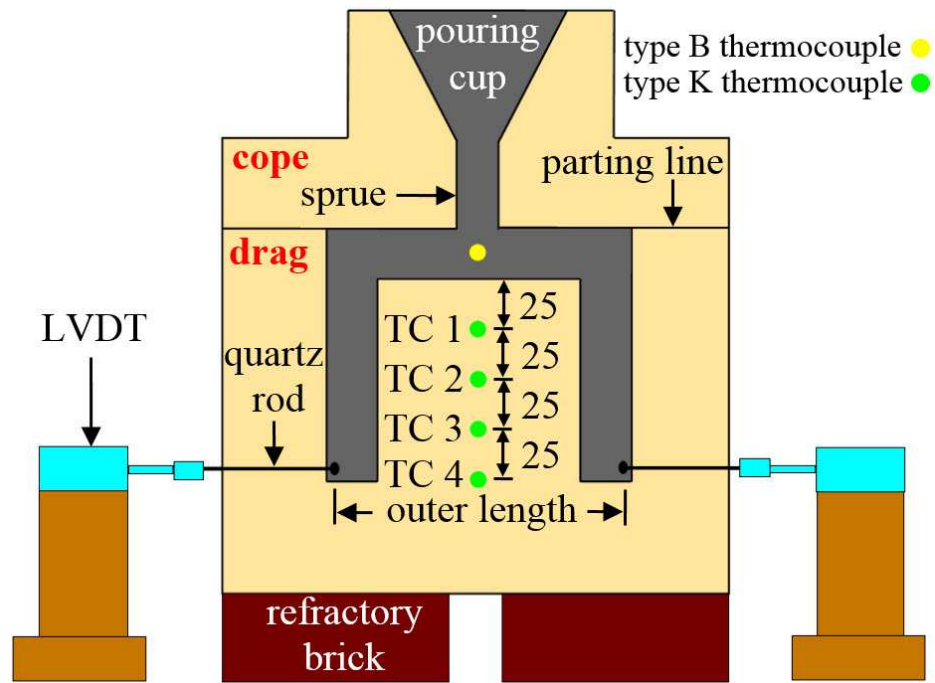
(b) Experimental Setup

Figure 2.2.   Casting geometry (a) and experimental setup at the casting mid-plane (b) for the bracket experiments. Units in mm.
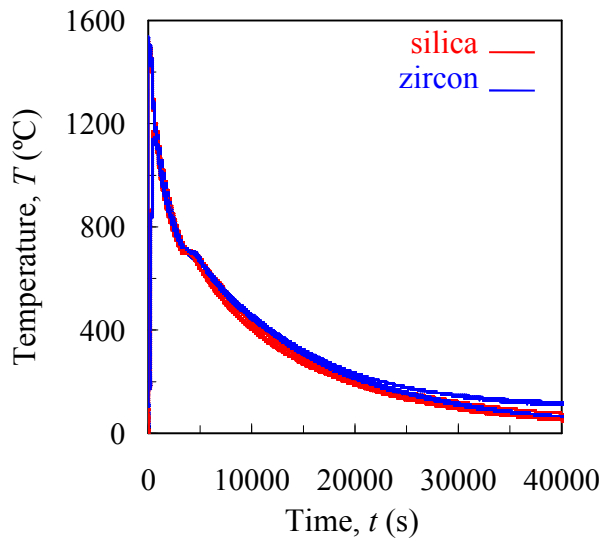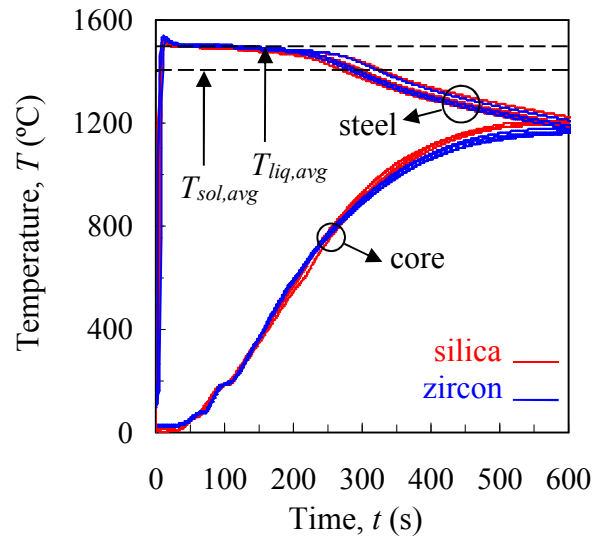
(a) Complete time scale (b) 600 s time scale

Figure 2.3.   Measured temperatures in the steel and center of core for silica and zircon cores for the cylinder experiments.

(a) Complete time scale   (b) 600 s time scale
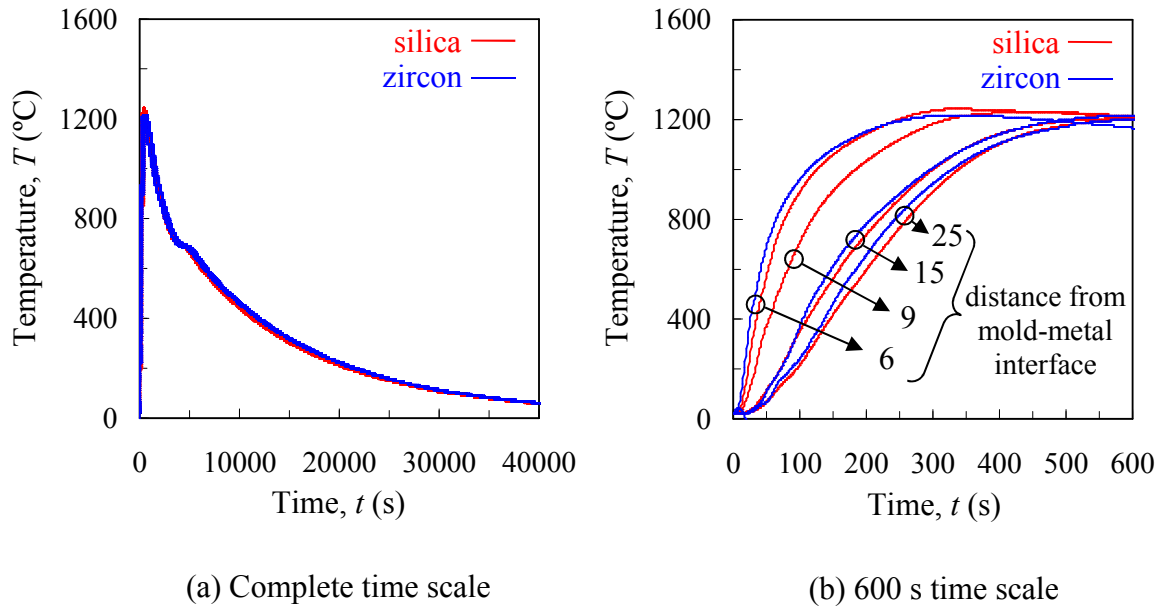
Figure 2.4.   Measured temperatures in the core for the cylinder experiments.
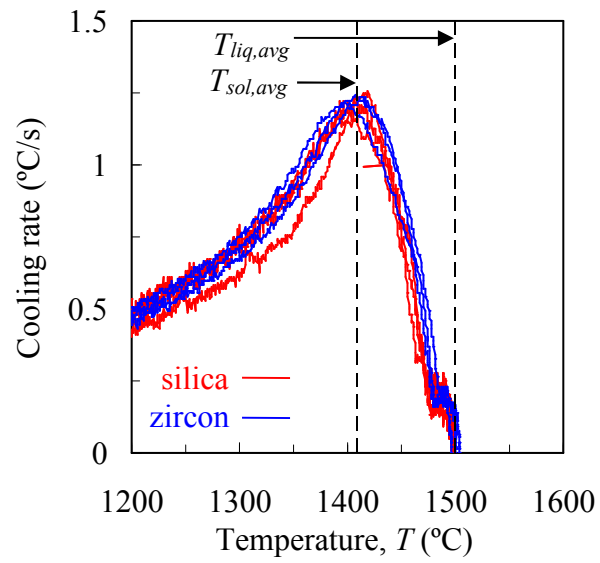
Figure 2.5.   Measured cooling rates for the cylinder experiments.
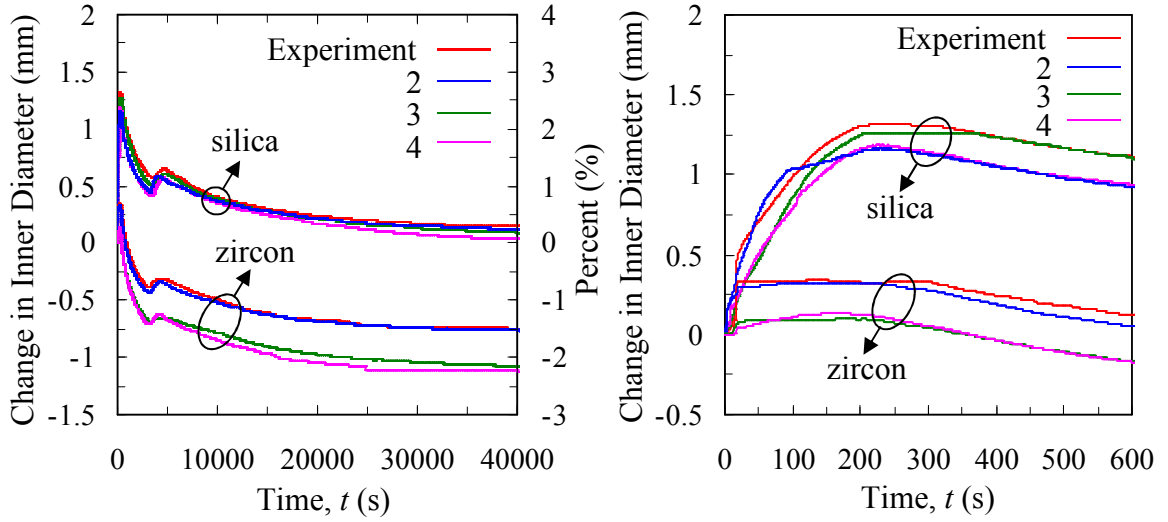
(a) Complete Time Scale   (b) 600 s Time Scale

Figure 2.6.   Measured change in the inner diameter at the cylinder's mid-height for the silica and zircon core experiments plotted on complete (a) and 600 s (b) time scales.

23
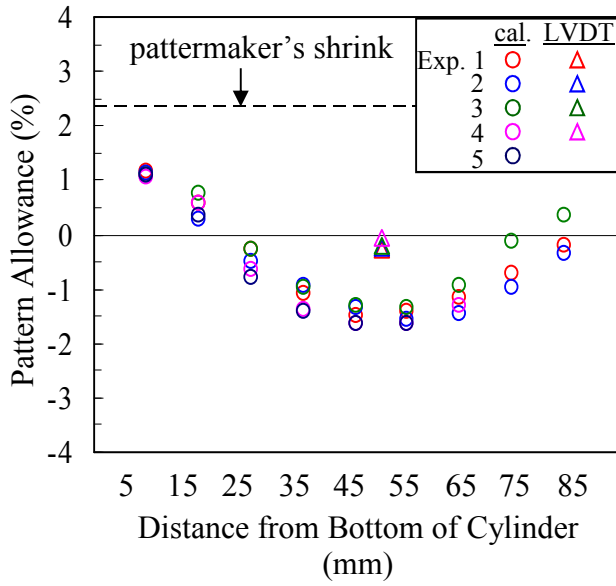
(a) Inner diameter pattern allowances
for silica core experiments

(c) Feature locations
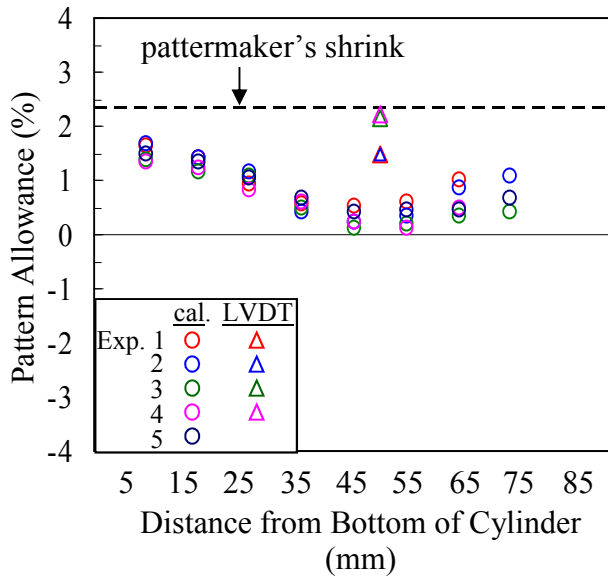
(b) Inner diameter pattern allowances
for zircon core experiments
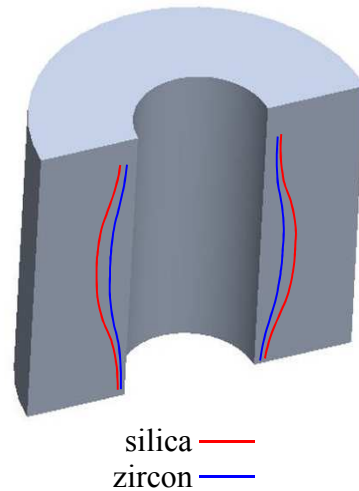
(d) Final inner diameter
profile

Figure 2.7.   Inner diameter pattern allowances for the silica (a) and zircon (b) core experiments (feature locations shown in (c)) were measured with digital calipers (cal.). Measurements revealed the barrel-shaped inner diameter profiles in (d).
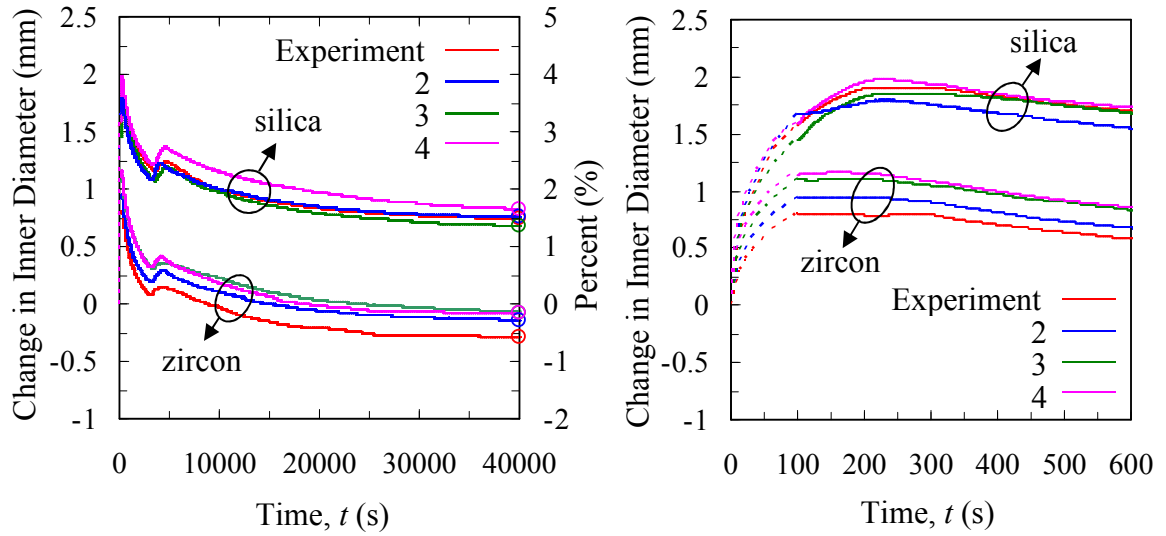
(a) Complete Time Scale (b) 600 s Time Scale

Figure 2.8.   Adjusted LVDT measurements. The LVDT curves in Figure 3 were modified to match the pattern allowances measured with calipers, which are represented by the circular symbols on the secondary axis in (a).
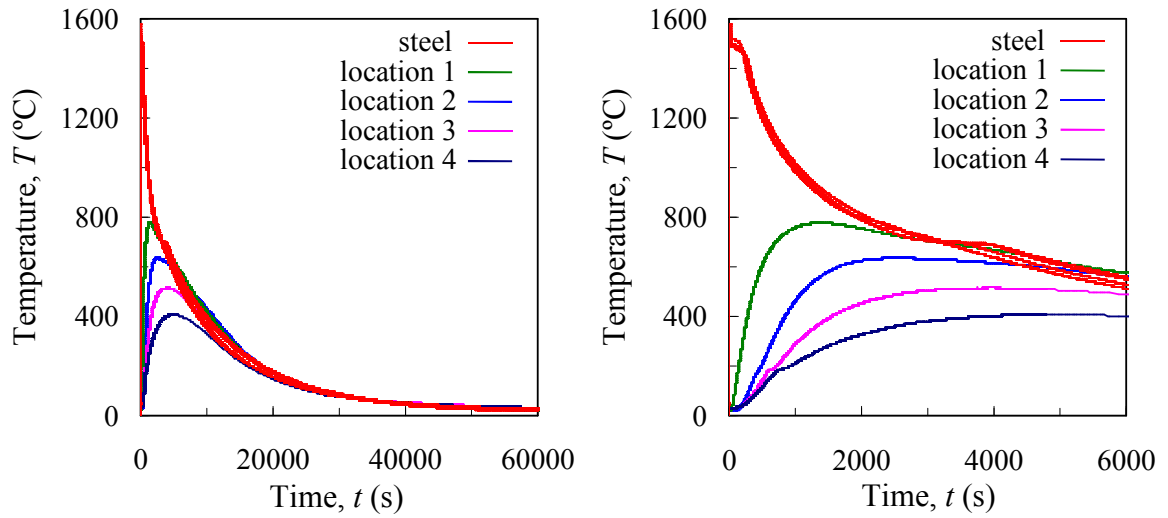
(a) Complete time scale

(b) 6000 s time scale
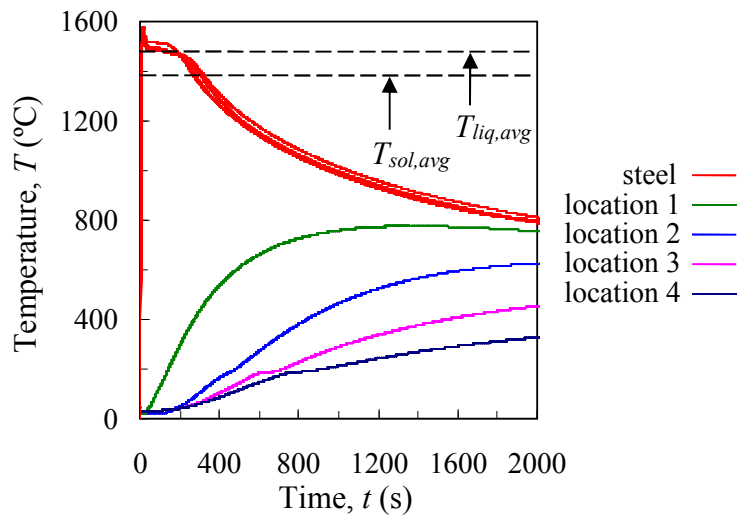
(c) 2000 s time scale

Figure 2.9.   Measured temperatures from the bracket experiments.
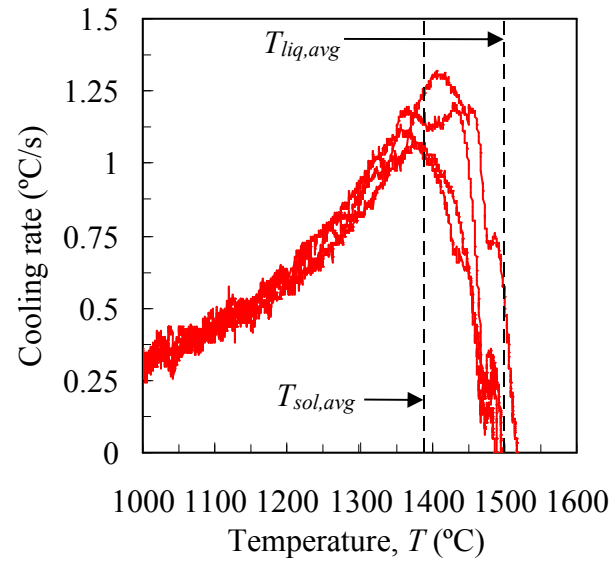
Figure 2.10.   Cooling curves for the bracket experiments.
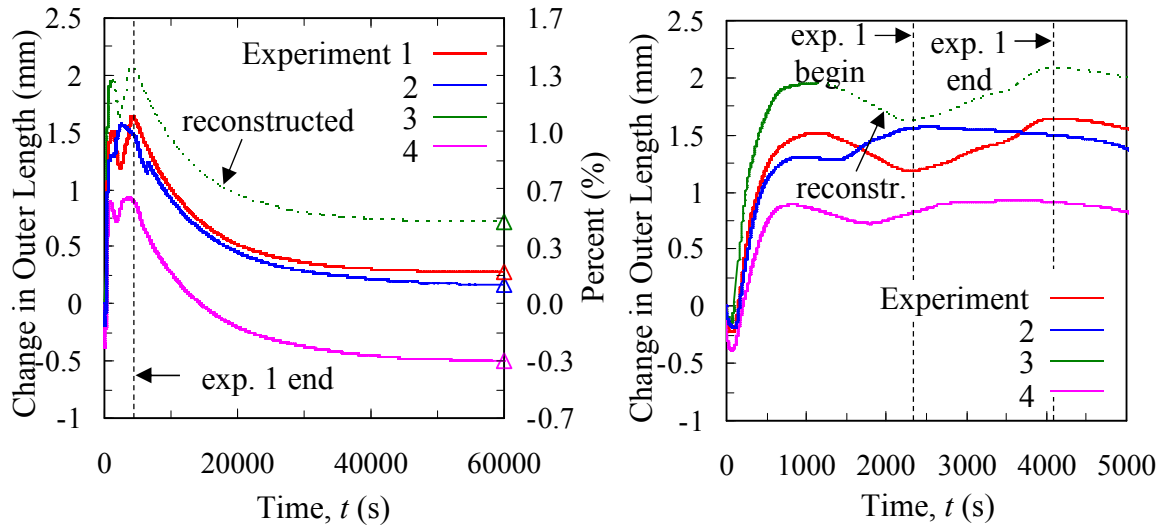
(a) Complete Time Scale
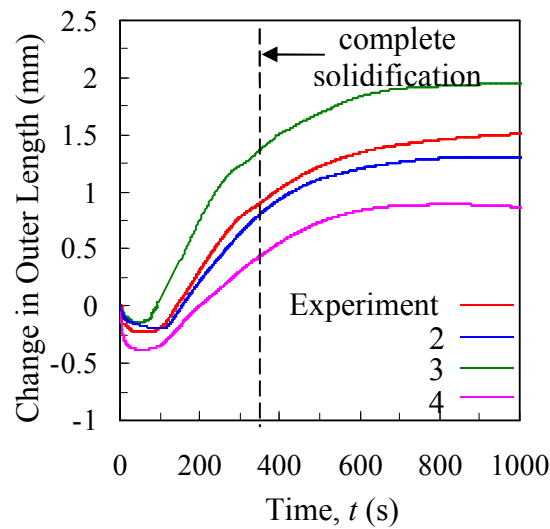
(b) 5000 s Time Scale

(c) 1000 s Time Scale

Figure 2.11.   Measured change in outer length of the brackets plotted on complete (a), 5000 s (b), and 1000 s (c) time scales.
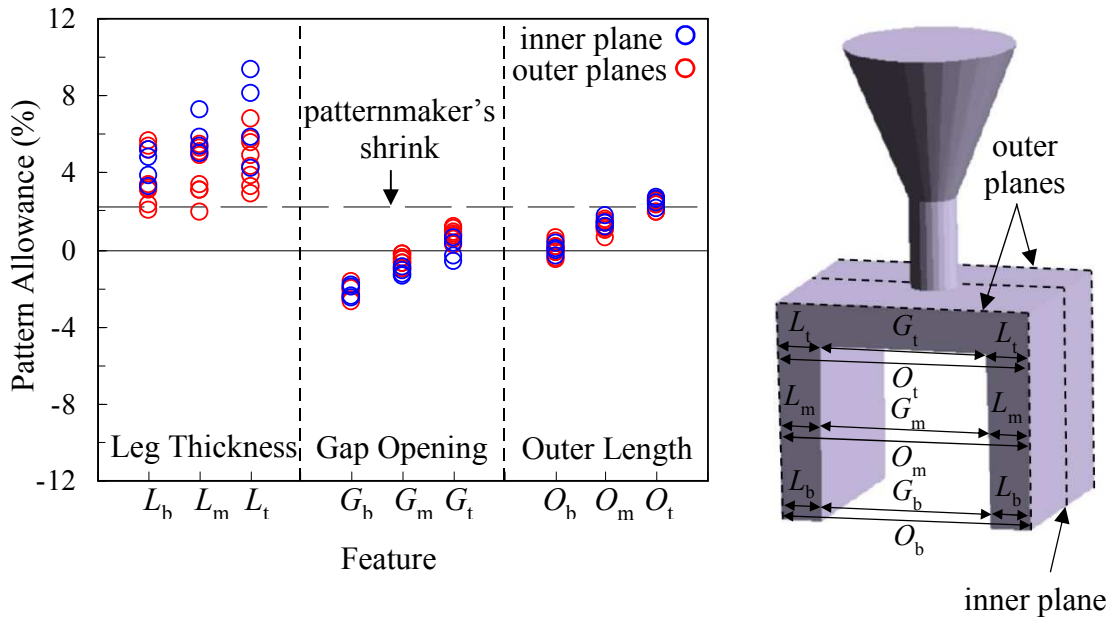
(a) Inner diameter pattern allowances for silica core experiments

(b) Bracket Feature Locations

Figure 2.12.   Pattern allowances for the brackets (a) were measured at the feature locations shown in (b).
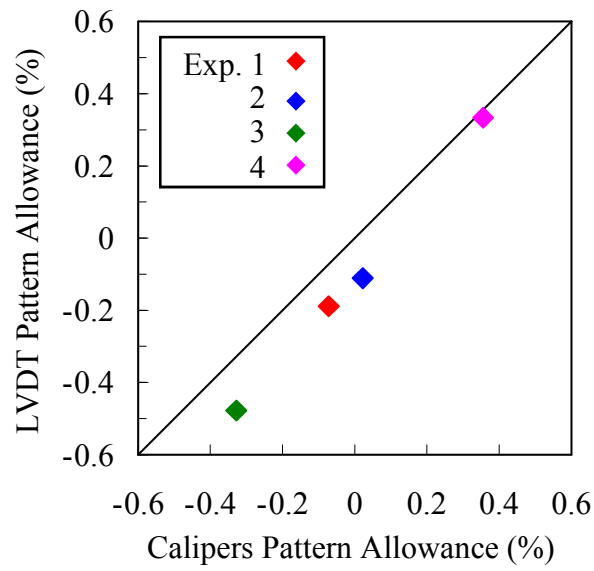
Figure 2.13. Pattern allowance comparisons between the LVDT and calipers measurements for feature O_b.

CHAPTER 3: THERMAL SIMULATIONS

Sand casting processes are characterized by a temperature-displacement coupling. Displacements are strongly influenced by temperatures, as the transient temperature fields are needed to calculate thermal strains in the casting and mold. In addition, the material properties used for the mechanical model are highly temperature-dependent. In contrast, temperatures are only weakly influenced by displacements. This influence is due to the formation of an air gap between the casting and mold caused by thermal contractions in the casting, which in turn affects the heat transfer between the casting and mold. The casting simulation software package used to predict temperatures in this study (MAGMASOFT® [14]) uses an additional boundary condition (i.e., interfacial heat transfer coefficient (IHTC)) at the mold-metal interface that accounts for the effect of the air gap. The inclusion of the IHTC allows the mechanical and thermal problems to be decoupled. As a result, a one-way coupling is used for this study in which transient temperature fields are calculated in the casting simulation software MAGMASOFT® and then used as inputs for the finite element stress simulations.

For the thermal simulations, virtual thermocouples were placed in the MAGMASOFT® model at the same locations as in the experiments (see Figure 2.1 and Figure 2.2). Using a finite volume formulation, temperatures in the metal were solved using the energy equation:

$$\overline{\rho}\left[\overline{c} - L_f \frac{df_s}{dT}\right]\frac{\partial T}{\partial t} = \nabla \cdot \left(\overline{k}\nabla T\right) \qquad [2]$$

where T is the temperature, t is the time, and f_s is the solid mass fraction. For fully liquid and fully solid metal, $f_s=0$ and $f_s=1$, respectively. In addition, L_f is the latent heat of solidification and $\overline{\rho}$, $\overline{c}$, and $\overline{k}$ are the density, specific heat, and thermal conductivity, respectively. The over bars denote the values are mixture quantities that depend on the amount of phase (i.e., liquid or solid) present in the control volume. Temperatures were

31

also solved in the mold using Eq. [2] without the term containing L_f.

For the initial thermal simulations, the temperature-dependent thermophysical properties, latent heat of solidification, and temperature-dependent solid mass fraction for the steel were calculated using IDS [15] software, a solidification analysis package for steels. Thermophysical properties for the bonded sands were taken from FURAN located in the MAGMASOFT® material database. The measured liquidus and solidus temperatures, which were determined from cooling curves (see Figure 2.5 and Figure 2.10), were used rather than the predicted values.

In general, using the estimated properties did not result in good agreement between measured and predicted temperatures. In particular, the simulated temperatures cooled slower than the experimental temperatures. Therefore, in order to match the measured and predicted temperatures, an iterative trial-and-error process was utilized, in which several adjustments were made to the simulation inputs. The entire process is discussed in detail elsewhere [16,17]. The main modifications included a reduction to the latent heat of solidification and adjustments to the temperature-dependent thermal conductivity of the bonded sand. Adjustments to the interfacial heat transfer coefficient were performed last in order to fine-tune the simulated temperatures so they were in excellent agreement with the measurements.

The final thermophysical properties (i.e., thermal conductivity, effective specific heat, and density) for the steel are shown in Figure 3.1. A spike in the specific heat can be seen at approximately 700ºC in Figure 3.1(b), which was added to model the effect of the solid state phase transformation. Essentially, the spike causes a temperature arrest that was observed in the experimental results. For this reason, the specific heat should be viewed as an effective value, which is denoted by the subscript *eff*. The solid fraction for the steel and interfacial heat transfer coefficient are shown in Figure 3.2(a) and (b), respectively. The thermophysical properties for the bonded sand are shown in Figure 3.3. The latent heat of solidification used in the simulations ranged from 190-200 kJ/kg. Using these properties

32

resulted in excellent agreement between measured and predicted temperatures for the cylinder and bracket experiments, as shown in Figure 3.4 and Figure 3.5. In addition, contours of the fraction of solid volume are shown for the cylinder and bracket experiments at several times in Figure 3.4(c) and Figure 3.5(c), respectively. These contours illustrate the uneven cooling in the castings, which will have considerable impact on the prediction of distortions. The temperature fields were output at a sufficient number of time steps (to give a smooth temperature profile at all locations) and then copied onto the finite element mesh.
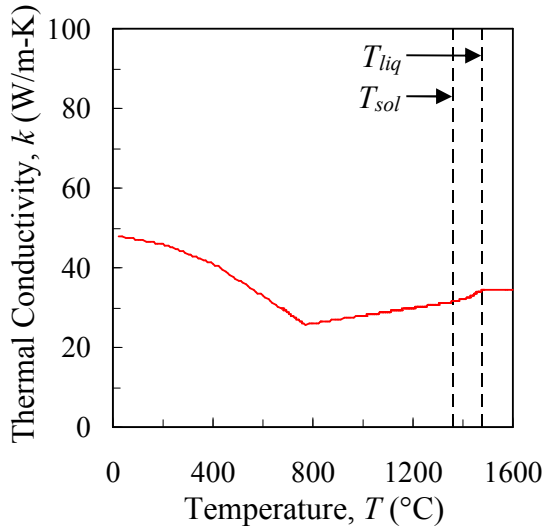
(a) Thermal Conductivity
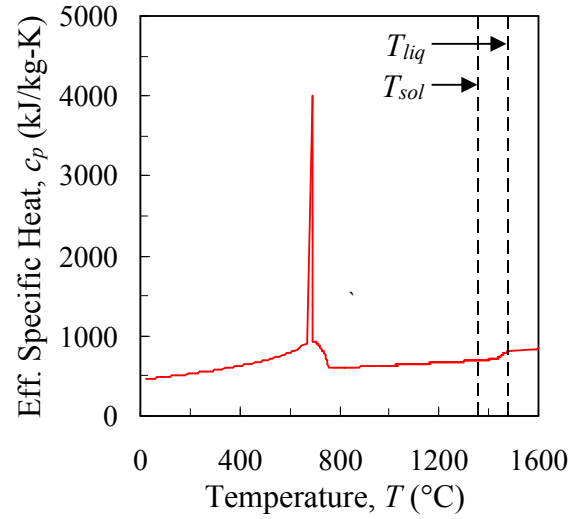
(b) Effective Specific Heat
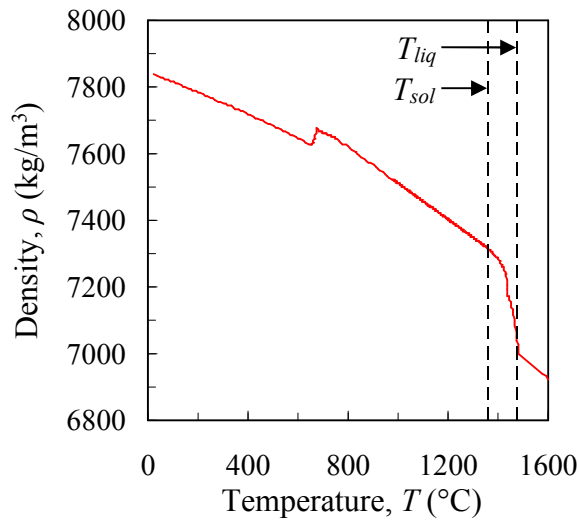
(c) Density

Figure 3.1.   Thermophysical properties for the steel.
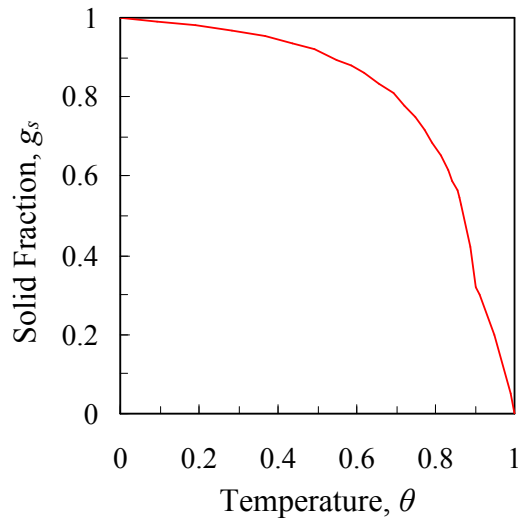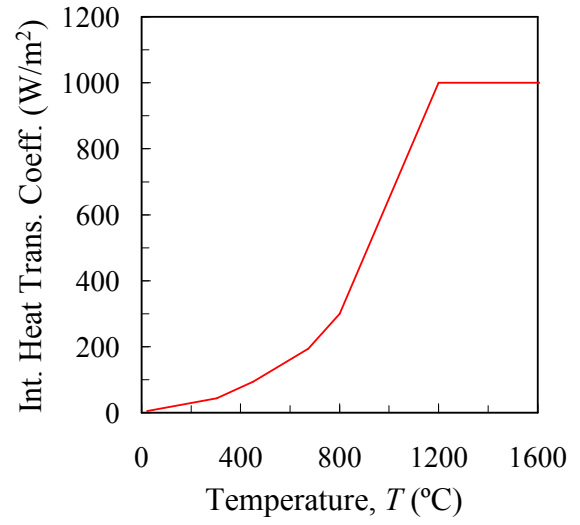
| (a) Solid fraction | (b) Interfacial heat transfer coefficient |

Figure 3.2.   Solid fraction (a) and interfacial heat transfer coefficient (b).
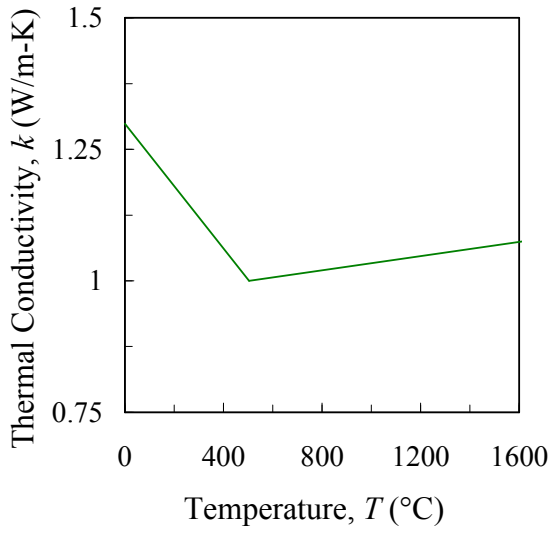
(a) Thermal Conductivity
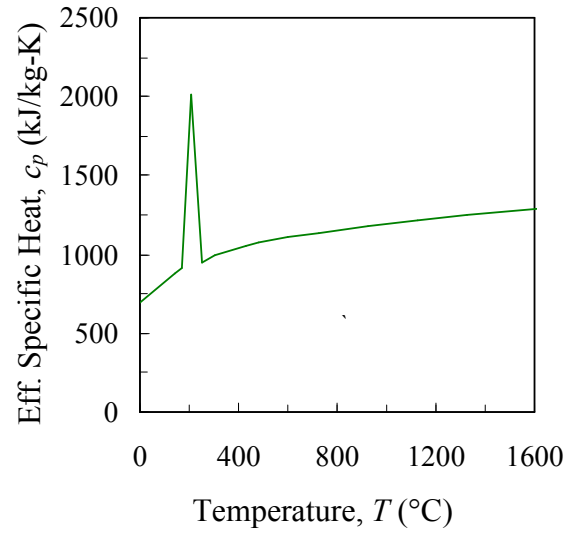
(b) Effective Specific Heat
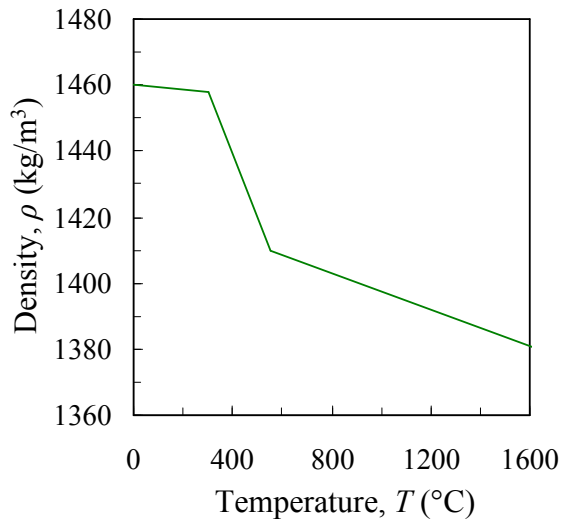
(c) Density

Figure 3.3.   Thermophysical properties for the bonded sand.

(a) Complete time scale (b) 600 s time scale

0.0   0.14   0.29   0.43   0.57   0.71   0.86   1.0
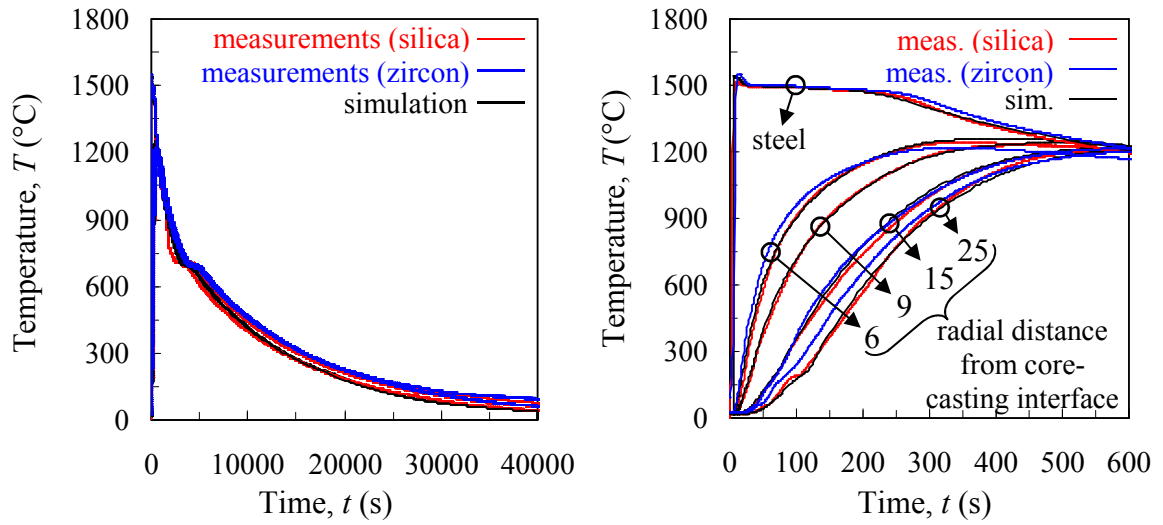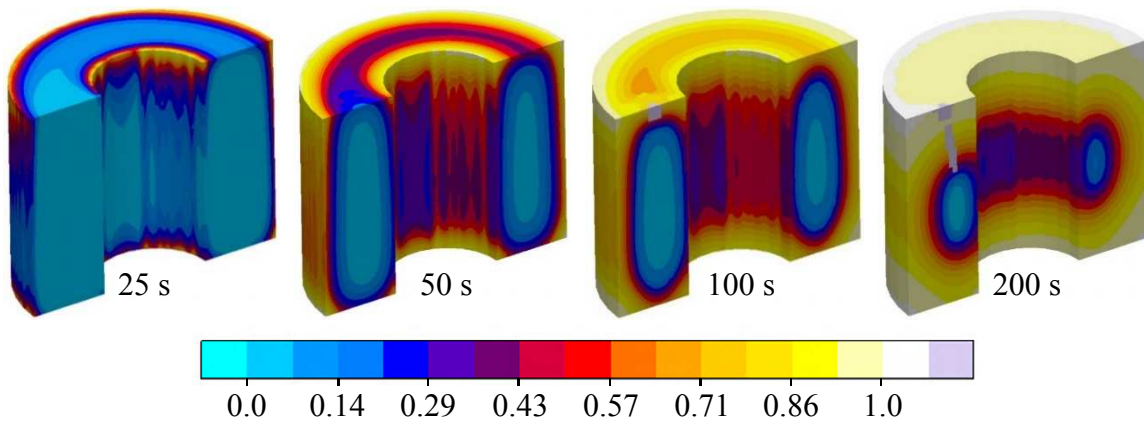
(c) Fraction Solid

Figure 3.4. Comparison between measured and predicted temperatures on complete (a) and 600 s (b) time scales. The thermocouple at the 9 mm location for the zircon core experiment failed. Solid fraction contours (c) illustrate uneven cooling.

(a) Complete time scale   (b) 2500 s time scale

25 s   50 s   100 s   200 s

0.0   0.14   0.29   0.43   0.57   0.71   0.86   1.0
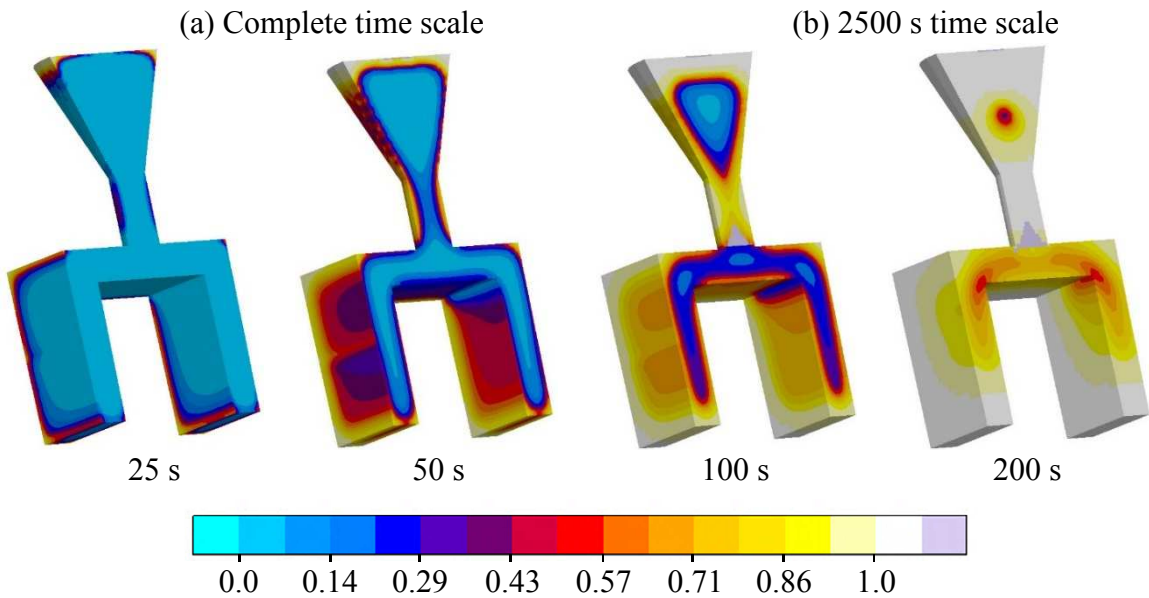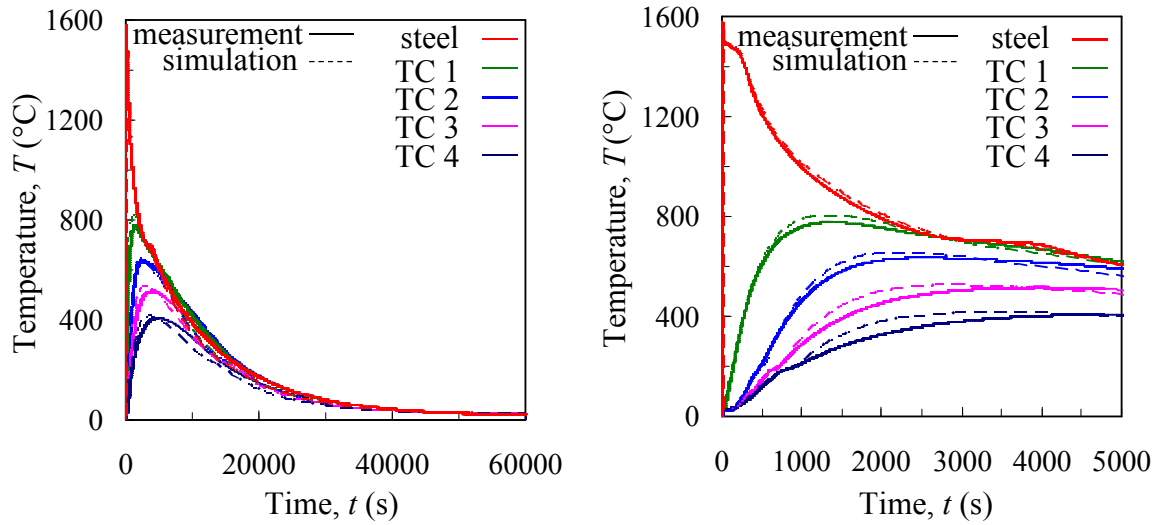
(c) Fraction Solid

Figure 3.5.   Comparison between measured and predicted temperatures for the bracket experiments. The fraction solid contours in (c) illustrate uneven cooling in the bracket.

CHAPTER 4: MECHANICAL MODEL AND PROPERTIES

4.1 Governing Equations

The stress model solves for the evolutions of stresses and displacements in the casting, core, and mold from the time of filling until shakeout. Assuming small strains, negligible inertial effects, body forces, and momentum transport between the solid and liquid during solidification, the strain tensor and mechanical equilibrium equation are given as

$$\boldsymbol{\varepsilon} = \frac{1}{2}\left[\nabla\boldsymbol{u} + (\nabla\boldsymbol{u})^{\mathrm{T}}\right] \qquad\qquad [3]$$

and

$$\nabla \cdot \boldsymbol{\sigma} = 0 \qquad\qquad [4]$$

where $\boldsymbol{u}$ is the displacement vector and σ is the Cauchy stress tensor.

The strain tensor is decomposed into the elastic $(\boldsymbol{\varepsilon}_e)$, inelastic $(\boldsymbol{\varepsilon}_{in})$, and thermal $(\boldsymbol{\varepsilon}_{th})$ components as

$$\boldsymbol{\varepsilon} = \boldsymbol{\varepsilon}_e + \boldsymbol{\varepsilon}_{in} + \boldsymbol{\varepsilon}_{th} \qquad\qquad [5]$$

The elastic strain is determined from Hooke's law as

$$\boldsymbol{\sigma} = \boldsymbol{C}_e : \boldsymbol{\varepsilon}_e \qquad\qquad [6]$$

where $\boldsymbol{C}_e$ is the elastic stiffness tensor. Assuming the mold, core, and casting are isotropic, homogeneous materials, it is given as

$$\boldsymbol{C}_e = \frac{E}{3(1-2\nu)}\boldsymbol{I} \otimes \frac{E}{3(1+\nu)}\boldsymbol{I}_{dev} \qquad\qquad [7]$$

where E is Young's modulus, ν is Poisson's ratio, $\boldsymbol{I}$ is the fourth-order identity tensor, and $\boldsymbol{I}_{dev}$ is the fourth-order deviatoric identity tensor.

4.2 Thermal Strains

Thermal strains arise from the volume changes in the casting, mold and core due to the large temperature changes during casting. They are calculated using the relation

$$\varepsilon_{th} = \int_{T_{th}}^{T} \alpha(T) dT \; \mathbf{1} \qquad\qquad\qquad [8]$$

where $\alpha(T)$ is the temperature-dependent coefficient of linear thermal expansion.

4.3 Constitutive Model and Properties for Steel

The constitutive relation for the steel is adopted from Monroe and coworkers [21,22] in which the steel is modeled as an elasto-visco-plastic material that features rate, hardening, and temperature effects. In addition, the solidification interval is modeled as a porous medium that exhibits pressure-dependent yielding. During solidification, the yield strength is a function of the solid volume fraction. This strategy allows for a single robust constitutive relation capable of modeling the steel in the liquid, semi-solid, and solid phases. A detailed description of the model and mechanical properties is given by Galles and Beckermann [13]. For the elastic mechanical properties, Young's modulus for the steel was taken from Li and Thomas [23] and is shown in Figure 4.1. A constant value of 0.3 was taken for Poisson's ratio. Parameters for the dynamic yield equation [13] are shown in Figure 4.2. In addition, the linear thermal expansion for the steel was calibrated by Galles and Beckermann [13] and is shown in Figure 4.3.

4.4 Constitutive Model for Bonded Sands

The bonded sands used in the mold and core are modeled using the Drucker-Prager Cap model, which is commonly used to model granular media that exhibit pressure-dependent yielding. The model is taken from the ABAQUS®[24] material library and reviewed here for completeness.

The Drucker-Prager Cap model is defined by a multi-surface yield function, shown in the meridional (i.e., deviatoric stress vs. pressure) plane in Figure 4.4(a). The shear

40

failure (F_s) surface is defined as

$$F_s = t - p \tan \beta - d = 0 \qquad [9]$$

where, $p = -1/3\,\text{trace}(\boldsymbol{\sigma})$ is the pressure and $\tan \beta$ is the slope of the failure surface. The cohesion parameter (d), defines the intersection of the shear failure surface with the deviatoric stress axis. The deviatoric shear stress (t) is given as

$$t = \frac{1}{2}q\left[1 + \frac{1}{K} - \left(1 - \frac{1}{K}\right)\left(\frac{r}{q}\right)^3\right] \qquad [10]$$

where the von Mises stress, $q = \sqrt{3/2(\boldsymbol{\tau} : \boldsymbol{\tau})}$, is determined from the deviatoric stress tensor, $\boldsymbol{\tau} = \boldsymbol{\sigma} + p\boldsymbol{1}$. Also, $r = (9/2\boldsymbol{\tau} : \boldsymbol{\tau} \cdot \boldsymbol{\tau})^{1/3}$ is the third stress invariant, and K governs the shape of the yield surface in the deviatoric stress plane (see Figure 4.4(b)). For the present study, $K=1$ (i.e., a circle in the deviatoric plane) is required for ABAQUS®/explicit, which reduces Eq. [10] to $t = q$. The Drucker-Prager yield surface is taken to circumscribe the Mohr-Coulomb failure envelope in deviatoric stress space.

The cap (F_c) and transition (F_t) surfaces in Figure 4.4(a) are defined as

$$F_c = \sqrt{[p - p_a]^2 + \left[\frac{Rt}{(1 + \alpha - \alpha/\cos \beta)}\right]} - R(d + p_a \tan \beta) = 0 \qquad [11]$$

and

$$F_t = \sqrt{[p - p_a]^2 + \left[t - \left(1 - \frac{\alpha}{\cos \beta}\right)(d + p_a \tan \beta)\right]^2} - \alpha(d + p_a \tan \beta) = 0 \qquad [12]$$

where R is the eccentricity of the elliptical cap, α is a small number (typically 0.01 to 0.05) that defines the shape of the transition surface, and the evolution parameter, p_a, is given as

$$p_a = \frac{p_b - Rd}{(1 + R \tan \beta)} \qquad [13]$$

41

where p_b is the yield stress under hydrostatic compression and defines the position of the cap in Figure 4.4(a). The hardening/softening behavior is characterized by the evolution of p_b, which was determined for this study with a 1-D compression test (see section 4.6).

The plastic strain increment is determined from the flow rule, given as

$$d\varepsilon_{pl} = d\lambda \frac{\partial G}{\partial \boldsymbol{\sigma}}$$ [14]

In Eq. [14], the subscript *pl* on the left side term replaces *in* (used in Eq. [5]) because creep is not considered in this study. In addition, $d\lambda$ is the magnitude of the plastic strain increment, *G* is the plastic potential, and $\partial G/\partial \boldsymbol{\sigma}$ is the direction of the plastic flow. The Drucker-Prager Cap model uses different plastic potentials for the failure surface (G_s) and cap surface (G_c), which are shown in Figure 4.4(c) and given as

$$G_s = \sqrt{[(p_a - p)\tan\beta]^2 + \left[\frac{t}{(1 + \alpha - \alpha/\cos\beta)}\right]^2}$$ [15]

and

$$G_c = \sqrt{[p_a - p]^2 + \left[\frac{Rt}{(1 + \alpha - \alpha/\cos\beta)}\right]^2}$$ [16]

Note that in Eqs. [15] and [16] no new parameters have been defined. The parameters used to characterize the yield surface also define the plastic potential. Comparing Figure 4.4(a) and (c), it is obvious that $F_c = G_c$, which implies associated flow in the cap region. For the shear failure region, non-associated flow is used, as the yield surface is different from the plastic potential, which is typical for materials that exhibit dilative behavior.

4.5 Properties for Bonded Sands

The accuracy of the computational model hinges largely on the selection of realistic material properties. In this study, mold and core expansion were induced by large

42

temperature increases, which suggests the high-temperature mechanical properties play an important role in determining an accurate solution. Unfortunately, no commercially available mechanical testing machines used for geological materials possess high-temperature measurement capabilities. Consequently, no high-temperature mechanical testing was performed in this study. Instead, as a first estimate, the high-temperature mechanical properties of the bonded sands were determined from room temperature tests on un-bonded, densely-packed sands. Using un-bonded sand to estimate properties is reasonable because pyrolysis of the binder essentially reduced the mold and core to un-bonded sands at high temperatures. Although some amount of temperature dependency can be expected in the bonded sands, it is reasonable as a first estimate to use room temperature values.

Several properties (β, α, R, v) were set as constants. Based on the findings of Saada et al. [12], the friction angle (β) was held constant. The shape parameter for the transition surface ($\alpha=0.01$) only governs a small portion of the yield surface and will have little impact on the simulation results. The cap eccentricity ($R=0.45$ [25]) defines the yield envelope at high pressures. This value is difficult to determine, as limited room temperature data is available. However, setting R as a constant is a reasonable first estimate because dense sand should be relatively incompressible even at high temperatures. Therefore, minimal yielding on the cap surface can be expected. Poisson's ratio ($v=0.3$) was also taken as a constant.

The remaining properties (E and d) were estimated over the entire casting temperature using the following procedure. The room temperature bonded sand properties ($E_{R.T.}$ and $d_{R.T.}$) were linearly decreased to their high-temperature values ($E_{H.T.}$ and $d_{H.T.}$) at some critical temperature, T_{crit}, and then held constant for all $T > T_{crit}$. The critical temperature represents the onset of pyrolysis of the binder, after which the mold and core are degraded to un-bonded sands. Although the properties can be expected to exhibit some degree of temperature dependency above T_{crit}, it is reasonable to expect minimal variations

43

over the temperature range for which distortions occurred. Therefore, using constant values above T_crit is justifiable as a first estimate.

The room temperature Young's modulus $(E_\text{R.T.})$ for bonded sands was determined from Thole and Beckermann [11]. The high temperature value $(E_\text{H.T.})$ was estimated from Hettler [26]. The same values were used for both silica and zircon bonded sands.

The friction angle (β) and high temperature cohesion $(d_\text{H.T.})$ for the Drucker-Prager Cap model were estimated from triaxial compression tests. The un-bonded cylindrical test specimen (70 mm long and 38 mm diameter) was contained in a 1-mm thick elastomer membrane during the test and housed in a triaxial cell. The test was carried out in 2 steps. First, a confining pressure was applied by filling the triaxial cell with water and then pressurizing it. This created a hydrostatic stress state, i.e., $\sigma_1 = \sigma_2 = \sigma_3$ (where the subscripts denote the principal directions). Next, a displacement controlled piston compressed the test specimen in the axial direction at a constant rate of 0.01 mm/min. Failure occurred after the measured axial force reached a peak value and began to decrease. The peak axial stress, σ_1, was a calculated by dividing the peak axial force by the cross-sectional area and adding the result to the confining pressure, i.e., $\sigma_1 = F/A + \sigma_3$. In total, 5 tests were performed, each at different confining pressures (100, 200, 300, 400, and 600 kPa), for each sand. For each test, a Mohr's circle can be constructed from the confining pressure, σ_3, and peak axial stress, σ_1. The friction angle can then be determined using the Mohr-Coulomb failure criterion. However, obtaining a best-fit failure envelope using statistical methods is difficult using this method. A convenient alternative is to plot the triaxial data on a modified Mohr-Coulomb diagram in which $1/2(\sigma_1 - \sigma_3)$ is plotted versus $1/2(\sigma_1 + \sigma_3)$. This diagram is advantageous because a single point represents each test, which enables a best-fit line to be easily constructed. Since dry sand has no cohesion, the cohesion parameter was set to zero by forcing the best-fit line through the origin. The results of the silica and zircon triaxial tests are shown on the modified Mohr-Coulomb diagram in Figure 4.5(a). The angles of the best-fit lines for the silica and zircon sand tests

44

were found to be $\psi = 35.3°$ and $32.7°$, respectively. Then, using the relation

$$\phi = \sin^{-1}(\tan\psi) \hspace{4cm} [17]$$

the Mohr-Coulomb friction angles were calculated as $\phi = 45.0°$ and $39.9°$ for silica and zircon, respectively. Finally, the Drucker-Prager friction angle was calculated using the relation

$$\tan\beta = \frac{6\sin\phi}{\sqrt{3}(3-\sin\phi)} \hspace{4cm} [18]$$

To give $\beta = 55°$ and $52°$ for silica and zircon, respectively. Conversion of the cohesion parameter from the modified Mohr-Coulomb diagram to the Drucker-Prager cohesion, d, resulted in $d = 0$ for both sands. Eq. [18] assumes the Drucker-Prager yield surface circumscribes the Mohr-Coulomb failure surface in deviatoric space, as shown in Figure 4.4(b). The room temperature cohesion ($d_{R.T.}$) was determined from a uniaxial compression test of bonded sand [10]. The failure stress ($\sigma_1 = 4.2$ MPa) and confining pressure ($\sigma_3 = 0$) were then used to generate a Mohr's circle. Using the friction angles obtained from the triaxial tests in conjunction with the Mohr's circle, the failure surface at room temperature was shifted upward until it was tangent to the Mohr's circle. The intersection of the failure surface with the deviatoric stress axis was taken as the room temperature cohesion value.

Hardening/softening behavior for the Drucker-Prager Cap model is associated with plastic volumetric strains and was determined for both sands from room temperature 1-D compression tests. A 1-D compression test is equivalent to an oedometer test. The former refers to tests on dry sands, whereas the latter is reserved for water-saturated specimens. For the test, an un-bonded cylindrical test specimen (25.4 mm tall and 38.1 mm in diameter) was compressed in the axial direction at a rate of 0.254 mm/min. By housing the sample in a rigid ring, displacement was prevented in the radial direction. Initial bulk densities (ρ_b) were measured to be 1858 kg/m^3 and 3169 kg/m^3 for the silica and zircon sands,

45

respectively. Although the test specimens were not packed, their bulk densities were higher than the measured room temperature core bulk densities used in the experiments (1751 kg/m^3 for silica and 3062 kg/m^3 for zircon). These differences are attributed to the binder in the cores, which reduced the volume of the sand grains. 1-D compression test results are shown in Figure 4.5(b) and (c) for the silica and zircon sands, respectively, and are plotted as void ratio (e) vs. ln p. The void ratio (e) is defined as the ratio of voids volume (V_v) to solids volumes (V_s) for the aggregate, i.e., $e = V_v / V_s$. The initial void ratio (e_0) is calculated from the bulk density using the relation $e_0 = \left(\rho_p / \rho_b \right) - 1$, where ρ_p is the particle density (ρ_p = 2650 kg/m^3 and 4700 kg/m^3 for silica and zircon respectively). The tests were carried out in the sequence (A-B-C-D-E) shown in Figure 4.5(b). The silica test specimen (e_0= 0.424) was loaded in segment A-B, unloaded in B-C, loaded again in C-D, and unloaded in D-E. From this procedure, a family of nearly-parallel curves can be seen in Figure 4.5(b) and (c) at pressures less than 10 MPa. In particular, segment B-C contains one unloading line and one reloading line, and both follow the same path. This implies that the unloading-reloading lines characterize the elastic response of the sand. This segment was then used as a guide to generate an idealized loading-reloading curve, whose slope is independent of the initial bulk density. The idealized loading-reloading curves were then shifted upward to correspond to the initial void ratios from the experiments (0.52 for silica and 0.54 for zircon).

A normal consolidation line (NCL) was determined from the slope of the measured 1-D compression curve at high pressures and assumed to be a linear function of log p. In order to include all pressure ranges, the curve was then extrapolated to low pressures, as shown in Figure 4.5(b) and (c). The position of the cap (see Figure 7(a)) at the onset of casting represents the initial isotropic compressive strength, p_{b0}, and is determined by the intersection of the idealized loading-reloading line and the virgin consolidation line in Figure 4.5(b) and (c). Any increase or decrease in p_b from the initial state is constrained to lie on the virgin consolidation line. The change in the void ratio that accompanies the

46

change in p_b can be used to determine the plastic volumetric strain increment ($\Delta\varepsilon_v^{pl}$) using the relation $\Delta\varepsilon_v^{pl} = (e_2 - e_1)/(1 + e_1)$, where the subscripts denote the initial (1) and final (2) states. From this relation, hardening curves were generated by plotting the isotropic compressive strength as a function of plastic volumetric strain for both sands (see Figure 4.5(d)). The estimated elastic properties and Drucker-Prager Cap model parameters for the silica and zircon bonded sands are summarized in Table 4.1 and Table 4.2, respectively.

The linear thermal expansion for the silica and zircon bonded sands was measured using a dilatometer. The results are shown in Figure 4.6.
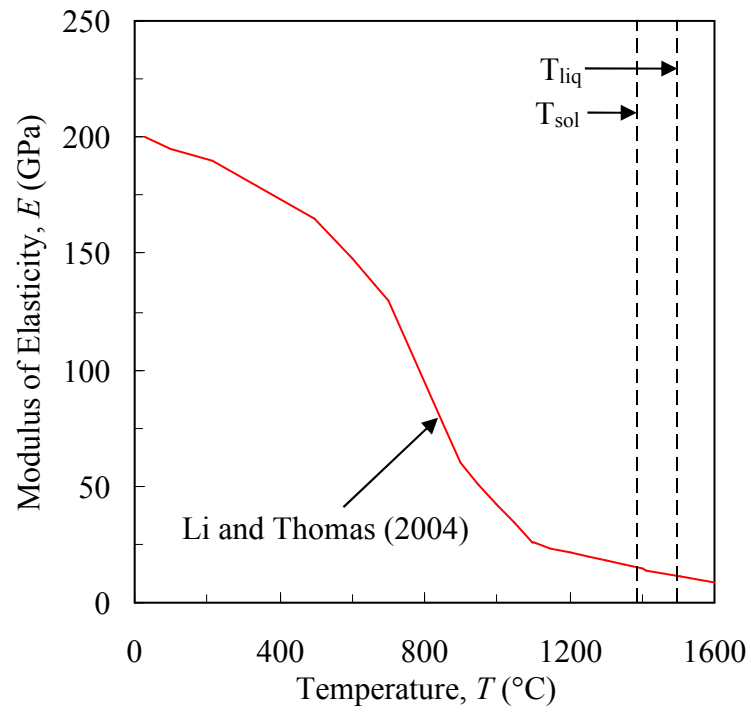
Figure 4.1.   Young's Modulus for the steel, taken from Li and Thomas [23].
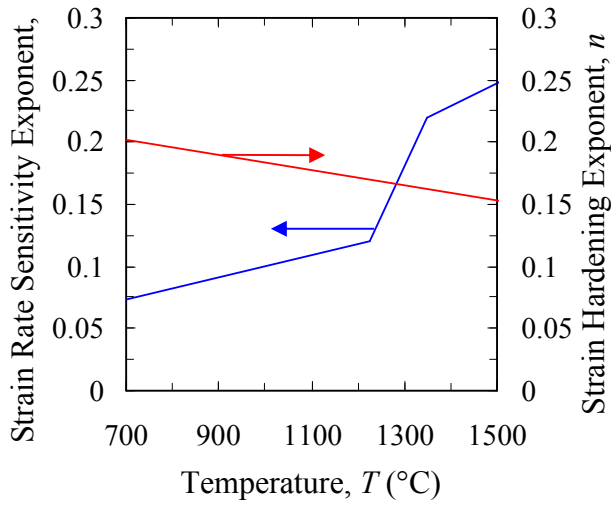
(a) Strain Rate Sensitivity and
Strain Hardening Exponents
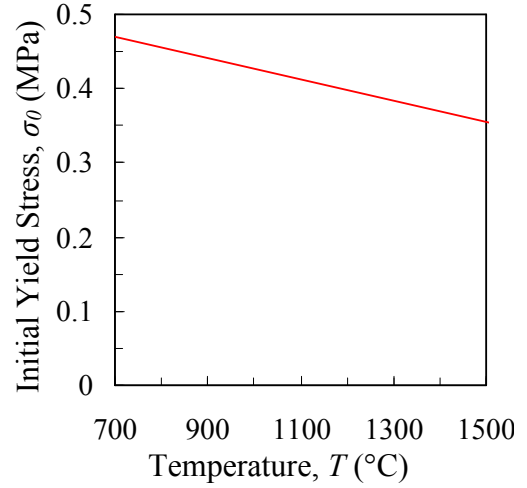
(b) Initial Yield Stress
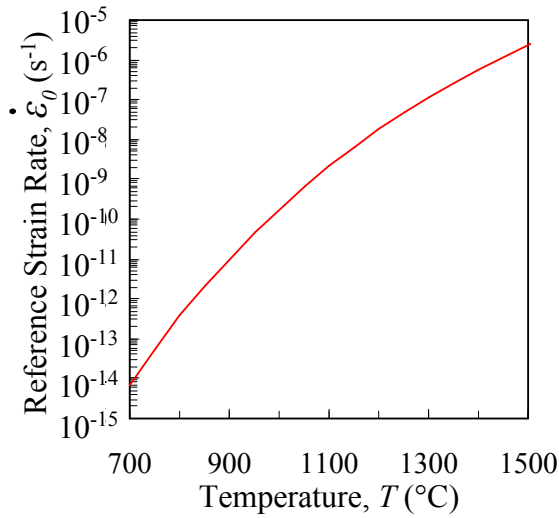
(c) Reference Strain Rate
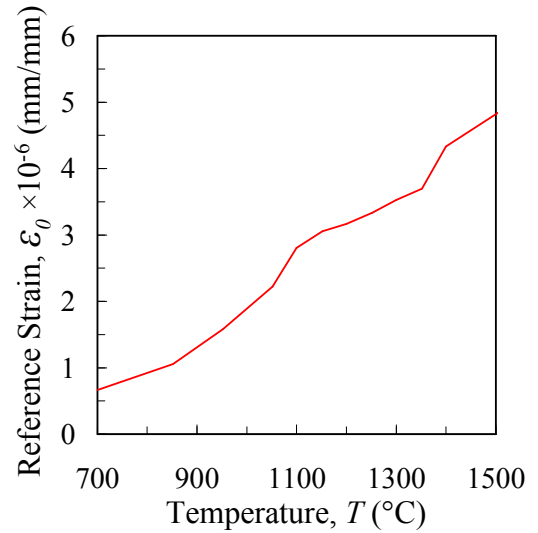
(d) Reference Strain

Figure 4.2.   Viscoplastic model parameters for steel.

49
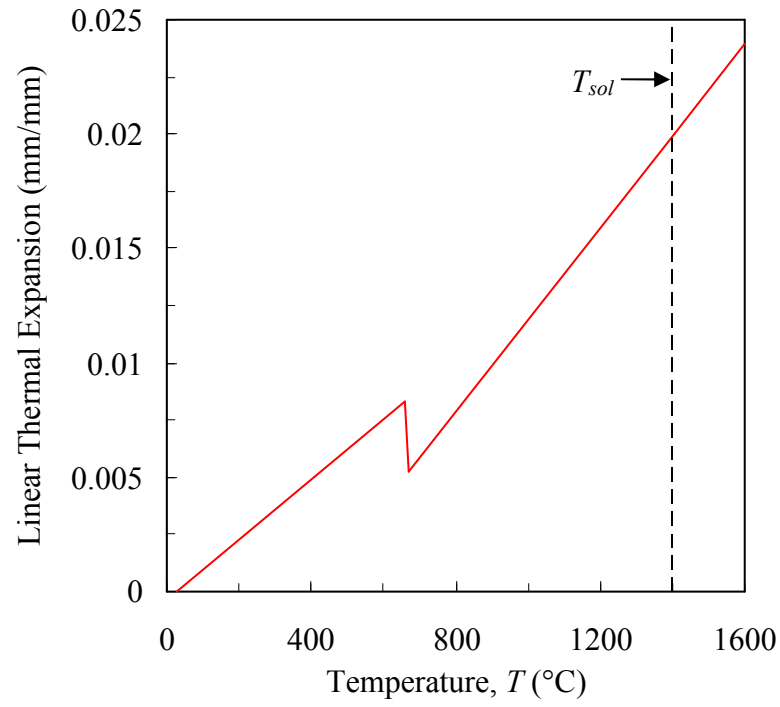
Figure 4.3.   Linear thermal expansion for the steel.

(a) Yield Surface in Meridional Plane

(b) Yield Surface in Deviatoric Plane

(c) Plastic Potential
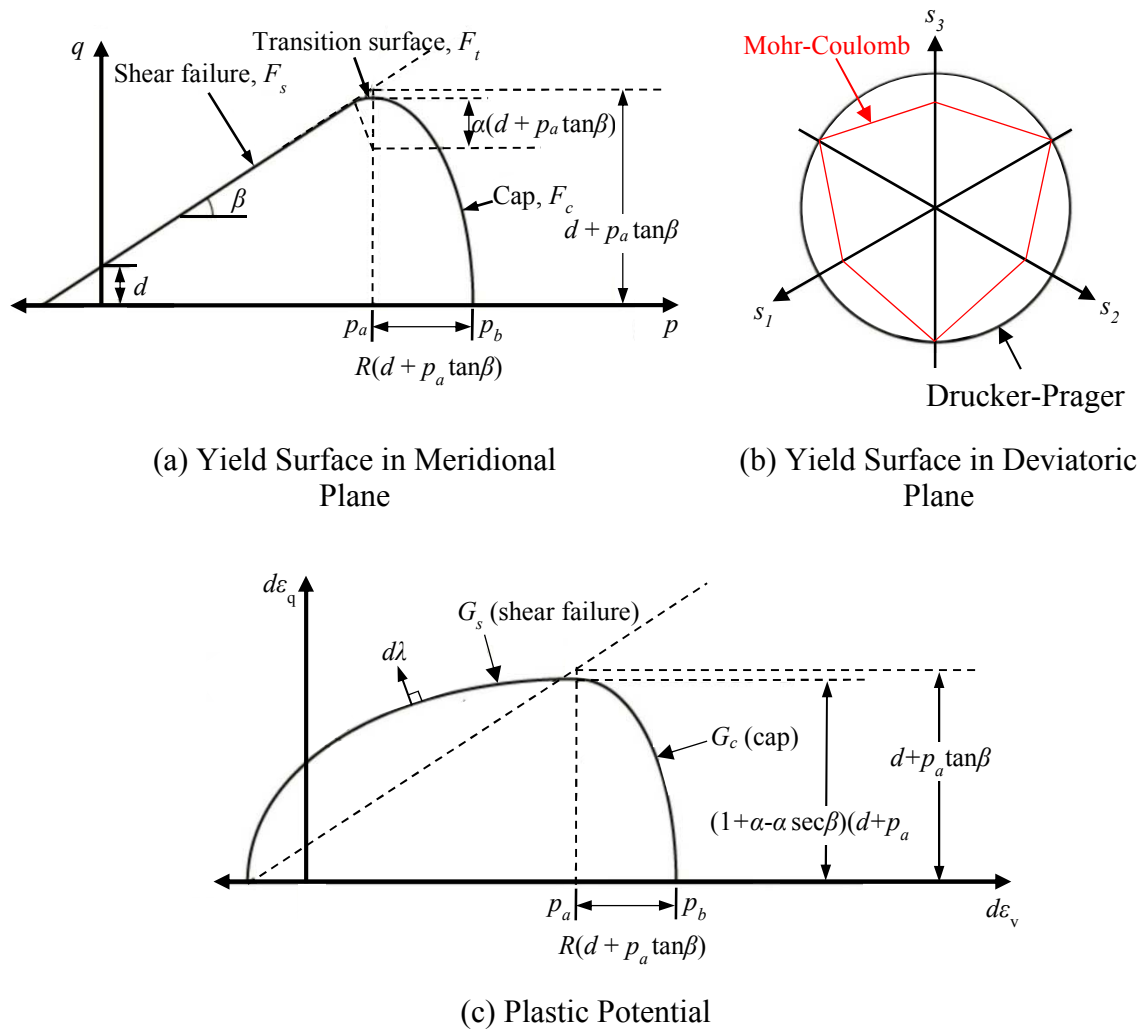
Figure 4.4. The Drucker Prager Cap yield surface in the meridional (a) and deviatoric (b) planes. The plastic potential (c) uses associated and non-associated flow rules for the cap and failure surfaces, respectively.

51
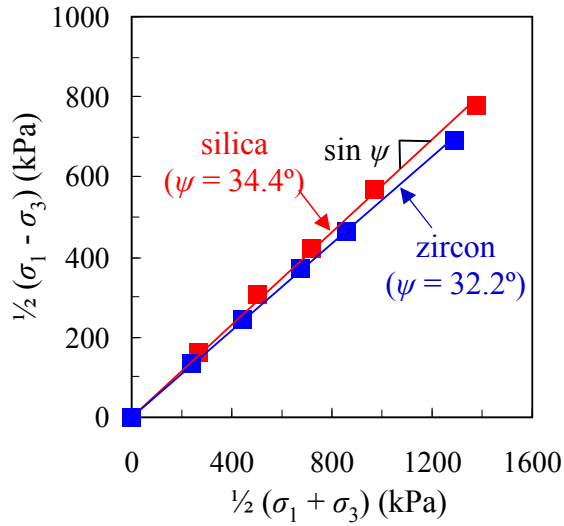
(a) Modifed Mohr-Coulomb Diagram
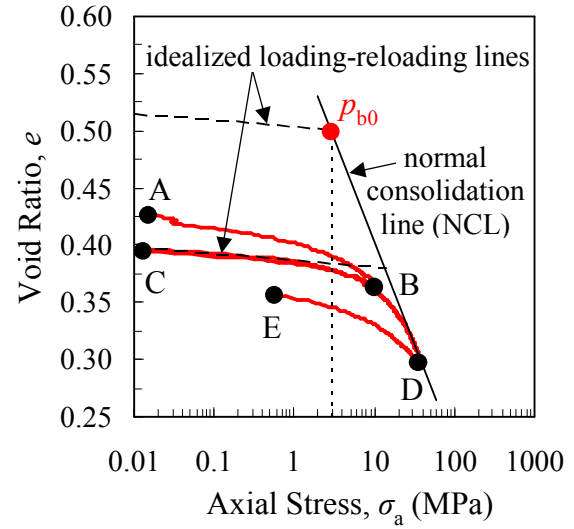
(b) 1-D Compression Test for Silica Sand
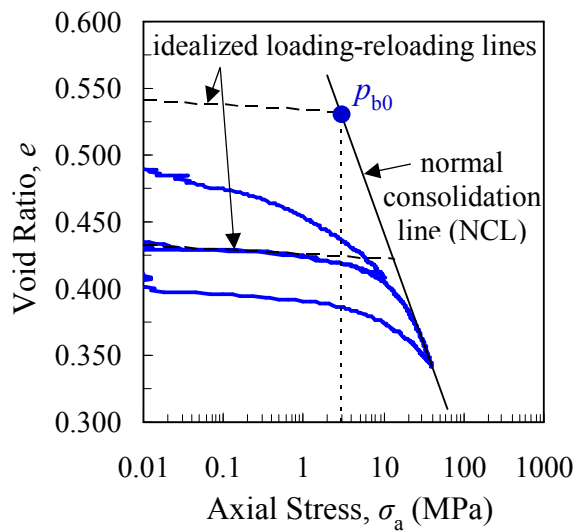
(c) 1-D Compression Test for Zircon Sand
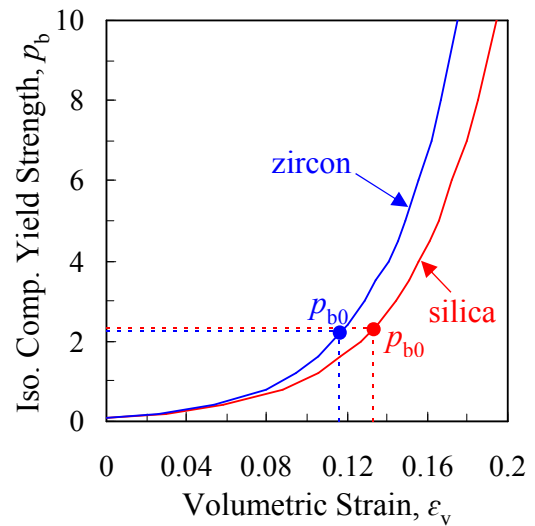
(d) Isotropic Compressive Yield Strength vs. Volumetric

Figure 4.5. Friction angles (ψ) for the Modified Mohr-Coulomb diagram (b) were determined from room temperature triaxial compression tests and then converted to Drucker-Prager friction angles. 1-D compression tests for silica (b) and zircon (c) sands determined the hardening behavior (d).

52

Table 4.1 Estimated mechanical properties and Drucker-Prager Cap parameters for the silica bonded sands.

Temperature (ºC)	E (MPa)	v	p_{b0} (MPa)	β	d (MPa)	R	α
20	3403	0.3	2.4	55º	1.15	0.45	0.01
180	60	0.3	2.4	55º	0.0	0.45	0.01
1600	60	0.3	2.4	55º	0.0	0.45	0.01

Table 4.2 Estimated mechanical properties and Drucker-Prager Cap parameters for the zircon bonded sands.

Temperature (ºC)	E (MPa)	v	p_{b0} (MPa)	β	d (MPa)	R	α
20	3403	0.3	2.3	55º	1.15	0.45	0.01
180	60	0.3	2.3	55º	0.0	0.45	0.01
1600	60	0.3	2.3	55º	0.0	0.45	0.01

53
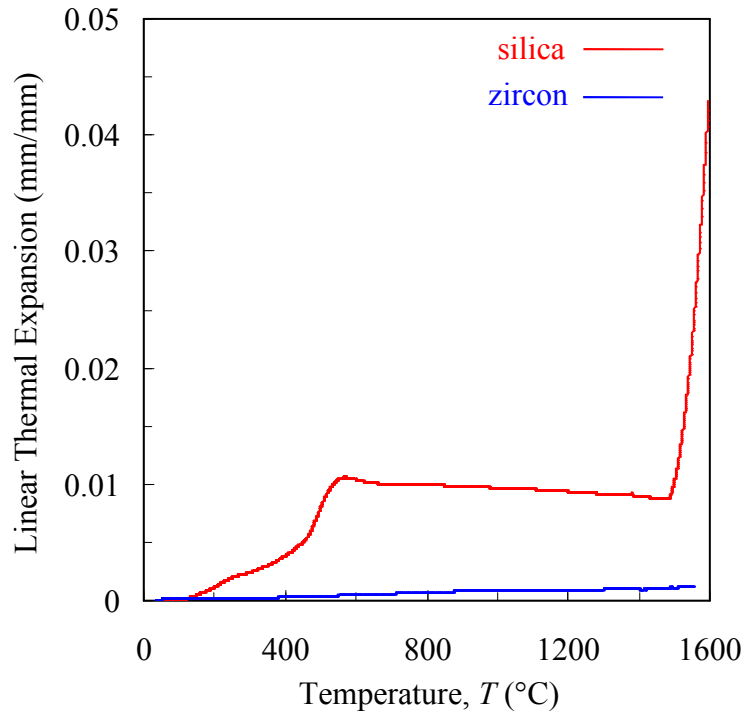
Figure 4.6.   Measured linear thermal expansion for silica and zircon bonded sands.

CHAPTER 5: STRESS IMULATIONS

5.1 Procedure

Stress simulations were performed using the general purpose finite element code ABAQUS®/explicit. An explicit integration scheme was chosen to avoid convergence issues associated with material softening when the material yields on the Drucker-Prager shear failure surface. The time step using the explicit method is conditionally stable. The critical time step is $\Delta t \leq 2/\omega_{max}$, where ω_{max} is the highest frequency (i.e., largest eigenvalue) of the system. This stability limit can be rewritten as

$$\Delta t = \min\left(\frac{L_e}{c_d}\right) \qquad [19]$$

where is L_e the characteristic element dimension and is derived from an analytic upper bound expression for the maximum element eigenvalue. The effective dilatational wave speed, c_d, of the material is defined as

$$c_d = \sqrt{\frac{\lambda + 2\mu}{\rho}} \qquad [20]$$

In Eq. [20], $\lambda = E\nu/[(1+\nu)(1-2\nu)]$ is the first Lamé constant, μ is the shear modulus, and ρ is the material density.

Inputting the mold and steel properties into Eq. [20] gives very large dilatational wave speeds that limit the time step and lead to impractical simulation times. For casting processes, however, inertial forces are not important, as deformations occur at rates much lower than the dilatational wave speed. Therefore, the time step may be substantially increased without significantly affecting the simulation results. This is achieved in ABAQUS®/explicit through "mass scaling" in which the mass is artificially increased. To ensure that mass scaling does not affect the results, the ratio of kinetic energy to total energy in the simulation should not exceed 5%.

www.manaraa.com

To save computational costs, the simulation models for the cylinder and bracket experiments were simplified. The cope can be expected to have minimal impact on distortions and was excluded from the cylinder and bracket models. The pouring cup and sprue were also excluded from the bracket model, as their impact on distortions of the bracket legs should not be important. Contact interactions between the casting, core, and drag were defined using the general contact algorithm in ABAQUS®/explicit, which employs a penalty method. The coefficient of friction between the contact surfaces was set to 0.4. First-order tetrahedral elements were used for the casting, core, and drag. Due to symmetry, only ¼ of both geometries were modeled. Using 8 processors, simulation times for the cylinder and bracket experiments were approximately 2 and 4 hours, respectively.

5.2 Cylinder Simulations

5.2.1 Prediction of thermal strains

Two preliminary finite element simulations predicted the evolutions of thermal strains in both the casting and core. The importance of these simulations is twofold. First, by subtracting the predicted thermal strains in the casting from the LVDT measurements, the evolution of casting distortions are revealed. Second, the predicted thermal strains in the core will verify whether the cylinder's inner diameter expansion during solidification is due solely to thermal expansion. If not, another mechanism must be considered. For each simulation, Minimal boundary conditions were enforced to prevent translations and rotations.

The predicted thermal strains for the cylinder are compared with the silica and zircon LVDT measurements on complete and 600 s time scales in Figure 5.1(a) and (b), respectively. Thermal strains were calculated using the linear thermal expansion of steel (shown in Figure 4.3), which was calibrated in a previous study [13]. During the initial 250 s, the simulation does not predict any change in the inner diameter, as the onset of thermal contraction for the steel does not begin until shortly before complete solidification (denoted

56

by a vertical dashed line in Figure 5.1(b)). Conversely, core expansion during this period caused the inner diameters to increase substantially, as shown by the LVDT measurements. The resulting divergence between the measurement and simulation curves during this time quantify the distortions. At 250 s, the thermal strain simulation curve begins to decrease, as the steel has reached coherency and begins to thermally contract. The onset of thermal contraction was set to a solid fraction of g_s=0.97 [13]. After complete solidification of the cylinder (at approximately 325 s), the thermal simulation curve decreases at the same rate as the silica and zircon LVDT measurements. The thermal strain simulation also predicts the inner diameter expansion associated with the solid state phase transformation at approximately 4000 s (shown in Figure 5.1(a)). It is obvious that the measured and simulated curves are parallel after 300 s and can be collapsed onto a single line. This important result verifies the previous speculation that all changes in the inner diameters after 300 s are solely due to thermal strains. In other words, core restraint did not generate any distortions. Instead, all distortions were created by core expansion before solidification had completed. This result is of great importance, as the earlier decision to adjust the LVDT curves at early times to match the measured pattern allowances was based on this idea.

The predicted thermal strains for the silica and zircon cores were calculated using the linear thermal expansion coefficients in Figure 4.6. The linear expansion curves illustrate the vast difference in thermal expansion between the different sands. In particular, phase changes in silica sand at 560ºC and 1470ºC generate considerable expansion, whereas no such events occur in zircon sand. The simulation results are compared to the LVDT measurements in Figure 5.2, which shows that the simulations greatly under-predict the measured core expansions for both silica and zircon sands. The simulation predicted only 0.5 mm (roughly 25% of the measurement) expansion for the silica core after 200 s. Similarly, the predicted thermal expansion at 200 s for the zircon core (~0.1 mm) is far less than the measured inner diameter expansions (~1.0 mm).

Such large discrepancies suggest that thermal expansion of the bonded sand was

not the only mechanism responsible for the core expansion. Initially, it was postulated that the cristobalite phase transformation in silica sand (see the sharp increase at approximately 1470ºC in Figure 4.6) may have been affected by atmospheric conditions inside the core, which in turn caused the transformation to occur at a lower temperature. Unfortunately, this argument cannot be made for the zircon core experiments because zircon sand does not experience phase changes. However, at the time, the zircon core experiments had yet to be performed. Therefore, through a parametric study, it was found that a cristobalite transformation temperature of 1300ºC was required to predict the measured expansion. Based on this result, a new experiment was designed and is depicted Figure 5.3(a). A rectangular plate (300×38 mm) was cast in a silica sand mold. Bonded sand samples were contained in thin-walled quartz tubes that butted up to the bottom casting surface. After the casting cooled to room temperature, the samples were carefully removed. 1 mm-thick layers were then extracted (see Figure 5.3(b)) and tested using x-ray diffraction. Cristobalite is quasi-stable at room temperature, as kinetic barriers prevent its transformation back to quartz. From the samples, the closest 1 mm layer from the mold-metal interface was found to contain less than 5% of the cristobalite phase. Smaller amounts were found in layers farther from the interface, as shown in Figure 5.3(b). Such small amounts of cristobalite could only account for about 0.01 mm of expansion in the experiment. This result suggests that the unexplained core expansion in the silica core experiments was not caused by cristobalite formation. Another explanation was needed.

A plausible explanation is that the unexplained core expansion can be attributed to sand dilation (see Figure 1.2). Recall that dilation is induced by shear forces, which can be expected at early times. The rapid flow of heat from the casting heats the refractory core from the outside inward and from the bottom of the mold cavity to the top, generating large temperature gradients. This uneven heating is conducive to the formation of shear forces. Fortunately, the Drucker-Prager Cap model features the ability to predict dilation. Therefore, dilation will be predicted by the stress simulations without any special

58

considerations.

5.2.2 Stress Simulations

In order to predict the inner diameter evolution for the cylinders, the stress simulations require several inputs. The elastic properties and material parameters for the steel and bonded sands are described Chapter 4.5. The thermal expansion coefficients for the steel and bonded sands are shown in Figure 4.3 and Figure 4.6, respectively. Finally, the calculated temperature fields were extracted from MAGMGASOFT® and copied onto the ABAQUS® mesh.

Using the inputs, the predicted inner diameter expansions far exceed the measurements, as shown in Figure 5.4. After 200 s, the silica and zircon cores expand by approximately 9.5 and 8 mm, respectively. This is in stark contrast to the thermal strain simulations for the cores that only predicted a small fraction of the measured expansions (see Figure 5.2). This vast additional expansion is the result of the volumetric expansion due to dilation that is predicted when using the Drucker-Prager Cap law. The excessive dilation that is predicted using the estimated properties can now be reduced through adjustments to the high temperature bonded sand properties.

In order to match the measured and simulated core expansions, parametric studies were performed to determine which parameter to adjust. At low temperatures (i.e., prior to binder pyrolysis), the core contains substantial strength and is unlikely to yield. Thus, only high temperature properties were considered. Also, only a single parameter was adjusted. Due to the uncertainties associated with the high temperature bonded sand properties, any attempt to modify more than one parameter would be arbitrary in nature. Parametric studies on the high temperature properties revealed that predicted and measured inner diameter evolutions could only be matched by modifying the cohesion parameter, d. The cohesion of bonded sands is determined by the binder. As the temperatures increase, the binder weakens and eventually pyrolizes, which in turn reduces d to a small value. Recall that the

high temperature cohesion was estimated from room temperature un-bonded sand, for which $d = 0$. The pyrolysis of binder is a kinetic process. Thus, the bonded sands likely yielded during this process before the cohesion had been completely degraded. In addition, it is possible that some small amount of cohesion remained in the bonded sands after pyrolysis. Evidence of this could be seen after shakeout, when the core sands still appeared somewhat "sticky". This behavior can be explained by binder residue that remained after pyrolysis. Therefore, using zero cohesion for the bonded sands at high temperature does not represent the actual behavior. Starting from $d = 0$, the high temperature cohesion, $d_{H.T.}$, was increased for the silica bonded sands (see Figure 5.5(a)) until the predicted inner diameter evolution matched the measurements at $d = 0.11$, as shown in Figure 5.5(b). Using the same procedure, $d_{H.T.}$ was adjusted to 0.08 to match the measured and predicted inner diameter evolutions for the zircon experiments.

Until now, it has been suggested that distortions were unlikely to occur in the bonded sands at lower temperatures before binder pyrolysis. To show this, a parametric study on the transition temperature was performed. Recall that the transition temperature defines the temperature at which the bonded sand is completely reduced to un-bonded sand as a result of binder pyrolysis. Starting from room temperature, the properties were linearly decreased to the high temperature properties at the transition temperature. Clearly, any change in the transition temperature will have a strong effect on the bonded sand properties at lower temperatures. Figure 5.5(c) illustrates how variations in the transition temperature between 50ºC and 400ºC affects the cohesion parameter. The other temperature-dependent properties will be affected in a similar manner. The sensitivity of the predicted inner diameter evolution to changes in the transition temperature is shown in Figure 5.5(d). The predicted inner diameter expansion varies less than 0.3 mm when the transition temperature is set to 300ºC or lower. This small amount of variation shows that the majority of yielding in the bonded sands occurs at temperatures above 300ºC.

Using the adjusted cohesion values for the silica and zircon bonded sands, the inner

diameter evolutions were predicted within the measurement scatter at all times, as shown in Figure 5.6. Recall that all changes in the inner diameter after solidification are due exclusively to thermal strains (see Figure 5.1). Thus, the adjustment to the cohesion parameter only affected the predicted inner diameter evolution before solidification. In addition, the pattern allowances were predicted with good accuracy, as shown in Figure 5.7. In particular, the barrel-shaped profiles were predicted. Only the zircon pattern allowances at the 5 mm location were not predicted within the scatter of the measurements. This disagreement can be attributed to uncertainties in the predicted temperatures. As previously stated, the evolution of the inner diameter into a barrel-shaped profile is the result of uneven cooling along the height of the cylinder. The smallest amounts of core expansion were observed near the ends where cylinder solidified earlier than near the middle. As a result, the pattern allowances near the ends were closer to the patternmaker's shrink.

Figure 5.8 shows contours of von Mises stress (a), pressure (b), equivalent plastic strains (c), and temperatures (d) at 50 s, 200 s, and 40,000 s (room temperature). The barrel-shaped profile can be seen for all contours after 50 s and is fully-evolved after 200 s. Large amounts of equivalent plastic strains can be seen in the core near the core-casting interface prior to this time, whereas far fewer equivalent plastic strains are predicted near the center of the core. This is particularly true at 50 s when temperatures near the core-casting interface exceed 500ºC and those near the center of the core are still close to room temperature. During early times, von Mises stresses and pressures are roughly 0.5 MPa in the areas of high equivalent plastic strains.

The estimated properties from Table 4.1 and Table 4.2 are updated to include the modified cohesion parameters. The final adjusted properties for the silica and zircon bonded sands are shown in Table 5.1 and Table 5.2, respectively.

5.2.3 Parametric Studies

The lack of high temperature mechanical measurements raises questions concerning the accuracy of the high temperature properties. Using room temperature un-bonded sand properties to estimate the high temperature values should only be viewed as a first estimate. Also, recall that the high temperature properties were set as constants. Certainly, some amount of temperature dependence can be expected. However, determining such properties would require additional experimentation that is beyond the scope of this study. Instead, parametric studies are performed in this section to show which high temperature parameters are most important. Through this study, the need for future mechanical testing for high temperature bonded sand properties can be assessed.

The sensitivity of the predicted inner diameter evolution to the high temperature Young's modulus ($E_{H.T.}$) and the cap eccentricity (R) are shown Figure 5.9. The complete temperature dependent curves for E used in the study are shown in Figure 5.9(a). Figure 5.9(b) shows that the change in inner diameter becomes increasingly sensitive as $E_{H.T.}$ decreases, particularly for values less than 100 MPa. For example, the predicted inner expansion at 200 s decreases from 1.9 mm to 1.25 mm (32% decrease) when $E_{H.T.}$ decreases from 60 to 25 MPa and 1.25 mm to 0.5 mm (65% decrease) when $E_{H.T.}$ decreases from 25 MPa to 10 MPa. However, for values of $E_{H.T.} > 100$ MPa, the predicted inner diameter is much less sensitive to $E_{H.T.}$.

The predicted inner diameter evolution was also sensitive to the cap eccentricity (which was varied from 0.45 to 3), as shown in Figure 5.9(c). This result is somewhat counter-intuitive, as the parameter R determines the shape of the cap surface. Yielding on this surface results in compaction of the bonded sands, which was not important for the cylinder experiments. However, an increase in R reduces the span of the shear failure surface, which in turn decreases the amount of predicted dilation. As a result, increasing the value of R decreases the maximum predicted core expansion.

The effect of changes in the normal consolidation line (NCL) were also investigated. Recall the 1-D compression tests in Figure 4.5(b) and (c). The NCL was

62

determined from the slopes of these curves at high pressures. Depending on the interpretation of these curves, it could be argued that the slope is too steep and should be reduced, as shown by the adjusted curve in Figure 5.10(a). The result of this adjustment is drastic, as the maximum predicted inner diameter expansion is roughly half of the simulation using the estimated value.

At high temperatures, the isotropic compressive strength of the bonded sand can be expected to decrease somewhat. This reduction can be modeled by shifting the NCL to the left at high temperatures as shown in Figure 5.10(c). In the figure, the "adjusted 1 NCL" curve reduces the high temperature isotropic compressive strength to 75% of the room temperature value, whereas the "adjusted 2 NCL" reduces the high temperature value by 50%. The effects of these reductions are shown in Figure 5.10(d). The predicted inner diameter expands less with decreasing high temperature isotropic compressive strength.

Two additional parametric studies investigated the effects of initial bulk density and coherency solid fraction of the steel. The initial bulk density was varied between 1700 and 1800 kg/m^3. Figure 5.11(a) shows that the predicted maximum inner diameter expansion varies by more than 1 mm due to these variations. These large variations illustrate the importance of controlling the mold filling process minimizing variability in the packing density. The coherency solid fraction has a minimal impact on the predicted inner diameter evolution, as shown in Figure 5.11(b).

5.3 Bracket Simulations

5.3.1 Prediction of Thermal Strains

As in the cylinder experiments, a preliminary finite element simulation calculated thermal strains in the steel bracket. For this simulation, the mold was excluded and minimal boundary conditions were applied to the bracket in order to prevent rigid body translations and rotations. Simulation results are shown in Figure 5.12. Shortly before complete solidification (approximately 300 s), thermal contractions commenced, after which the

change in outer length decreased until 2600 s. At all times prior to 2600 s, the measured curves can be seen to either converge to or diverge from the thermal strain simulation curve. This important observation shows that distortions are continuously generated and impact the change in outer length before 2600 s. From 2600 s to 3900 s, the simulated outer length increased due to the solid state phase transformation, after which it monotonically decreased until room temperature. The measured and bracket-only outer length curves are parallel at all times after 3900 s, which implies that all measured changes in the outer length after the solid state phase transformation were due to thermal strains.

5.3.2 Stress Simulations

For the stress simulations, the adjusted bonded sand properties from Table 5.1 were used. No bulk density measurements of the bonded sands were taken during the experiments. Therefore, a representative bulk density (ρ_b = 1710 kg/m^3) was estimated from a hand-packed bonded sand sample. From this initial bulk density, the initial isotropic compressive yield stress, p_{b0}, was determined from Figure 4.5(b) to be 1.7 MPa. Using these inputs, the pushout of the legs was under-predicted, as shown in Figure 5.13. Although the predictions showed that the bracket legs were pushed out somewhat, the observed magnitude could not be predicted. In particular, the observed rate at which the legs were pushed outward between 100 s and 1000 s was under-predicted.

During the experiments, the drag fractured at the location shown in Figure 5.14(a) shortly after pouring. Up until the time of fracture, the tensile strength of the mold provided restraint that prevented the bracket legs from being pushed outward. At the time of fracture, however, the outer mold tensile strength was reduced to a very small value, which essentially eliminated the mold restraint. Afterwards, the bracket legs could be easily pushed outward. To simulate this behavior, a crack plane was defined in the model at the observed location of fracture using surface-based cohesive behavior in ABAQUS®. The degradation of the cohesive bond is simply defined by the force-displacement behavior of

64

a uniaxial tensile test performed on a room temperature bonded sand sample after it reaches a maximum stress. In other words, the only input required to define the onset and propagation of the crack plane is the uniaxial softening behavior. Using reference [10], a maximum stress of 1.3 MPa was measured from a sodium silicate bonded sanded, after which the sample completely failed after the cracked opening reached 0.015 mm. From the LVDT measurements, the bracket legs for experiments 1, 2, and 4 begin to push out at approximately 100 s (see Figure 2.11(c)). However, the bracket legs for experiment 3 are pushed outward at about 75 s. This difference suggests that the mold fractured earlier during experiment 3 than for the other experiments. Most likely, the mold contained a defect that led to its premature failure. Rather than using the maximum stress from reference [10], a parametric study investigated the effect of the maximum uniaxial tensile stress. For each case (see Figure 5.14(b)), the bond was assumed to completely fail after the crack opened 0.015 mm. The area under each of these curves represents the fracture strength. The predicted distortions for each case is shown in Figure 5.14(c). The effect of maximum stress is two-fold. An increase in maximum stress 1) causes the mold to crack at a later time, which 2) results in less pushout of the bracket legs. Therefore, by simply adjusting the maximum uniaxial tensile stress as shown in Figure 5.14(c), the time at which the observed push-out of the bracket legs commenced can be predicted.

In order to simulate the cracking behavior, the model was modified as shown in Figure 5.15. Rather than modeling only ¼ of the model, now ½ of the setup was required in order to include the crack plane. Dynamic effects are important when the cohesive bond fails, which initially caused the bracket legs to rapidly push outward. In order to dissipate these dynamic effects, body forces were included and a coefficient of friction of 0.4 was specified between all contact surfaces (depicted as pink lines) shown in Figure 5.15. The refractory bricks were also included, for which zero displacement boundary conditions were specified on the bottom surfaces. The solid green lines in Figure 5.15 define the crack planes. A horizontal crack plane that spanned the bracket legs was defined at the bottom of

the casting. Without this plane, the vertical crack plane could not propagate. The pouring cup and metal inside it were not included in the model. Instead, their combined weight were modeled as a distributed load on top of the cope.

From Figure 5.14(c), the correct magnitude of pushout for the bracket legs for bracket 4 can predicted by increasing the fracture strength. However, this increase also causes the cohesive bond to fail later, causing disagreement between the measured and predicted changes in outer lengths for $t < 200$ s. Therefore, an additional modification is needed to achieve agreement for all times. Recall that the molds for the bracket experiments were hand packed. Hence, the initial bulk density likely varied somewhat for each experiment. The effect of the bulk density on the bonded sand strength is illustrated on the void ratio vs. log p plot shown in Figure 5.16. The initial isotropic compressive strength, p_{b0}, of the bonded sand is determined from the normal consolidation line (NCL). From the figure, it can be seen that as the density increases, p_{b0} also increases. In other words, if the bonded sand is tightly-packed, the bulk density and compressive strength are high. Conversely, for loosely-packed bonded sand, the bulk density and compressive strength are low. The effect of the initial isotropic compressive strength is shown in Figure 5.16(b). For this set of simulations, the maximum uniaxial stress was set to 1 MPa (i.e., case 2 from Figure 5.14(b) was used). Now it can be seen that through adjustments to the initial bulk density, the amount of predicted pushout of the bracket legs varies while the time of fracture remains the same.

In order to match the measured and simulated changes in outer lengths, the maximum uniaxial stress was first adjusted so that the measured and simulated times at the onset of bracket leg pushout were matched. Then, the density was adjusted so that the correct magnitude of pushout was predicted. The results are shown in Figure 5.17. The maximum tensile stress and bulk densities used for the simulations are listed for each bracket. Now, the measurements and simulations are in excellent agreement at all times, with the exception of brackets 2 (blue curve) and 4 (pink curve) between 1500 s and 4000

66

s. The disagreement at these times is due to differences in the casting chemistries that caused the solid state phase transformation to occur at different times.

The pattern allowances were also predicted. Comparisons between measured and predicted pattern allowances for bracket 1 (see Figure 5.18(a)) reveal excellent agreement. In addition, the significant difference between the inner and outer plane PAs that was observed for feature L_t is also predicted. Similar agreement was seen for all other brackets. Figure 5.18(b) shows the root mean square error of the predictions for all brackets. The figure shows that on average, the predicted pattern allowance error is roughly 0.5%. To give this number meaning, using the patternmaker's shrink gives a root mean square error of greater than 2%.

Finally, predicted von Mises stresses and equivalent plastic strains in the casting and mold are shown in Figure 5.19. In Figure 5.19(a), von Mises stresses exceeding 0.5 MPa are predicted at 200 s in the section of the mold between the bracket legs. These shear stresses are a necessary condition for dilation. After the casting cools to room temperature (60,000 s), residual stresses in excess of 40 MPa can be seen in the casting. Figure 5.19(b) shows equivalent plastic strain contours in the mold for yielding on the shear failure surface. Because dilation is associated with such yielding, the large amounts of equivalent plastic strain seen in this figure are indicative that significant amounts of dilation are occurring. In contrast, Figure 5.19(c) shows minimal plastic strains associated with the cap surface are being predicted in the mold. In other words, minimal compression is predicted in the bonded sand. Predicted equivalent plastic strains in the bracket are shown in Figure 5.19(d). The majority of plastic strains are predicted on the bottom casting surface between the legs.
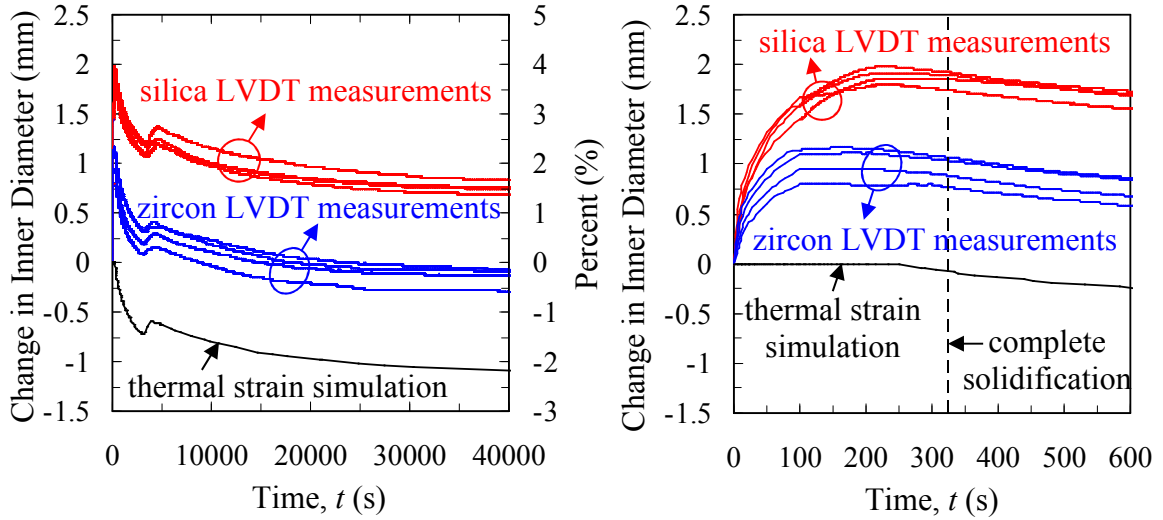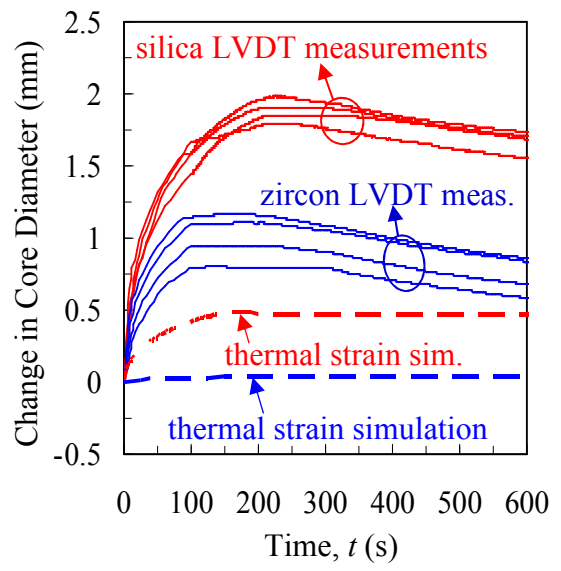
(a) Complete Time Scale   (b) 600 s Time Scale

Figure 5.1   Thermal strains for the cylinder were calculated using the inputted temperature fields from MAGMASOFT® and linear thermal expansion coefficient (c), which was calibrated by Galles and Beckermann [13].

68
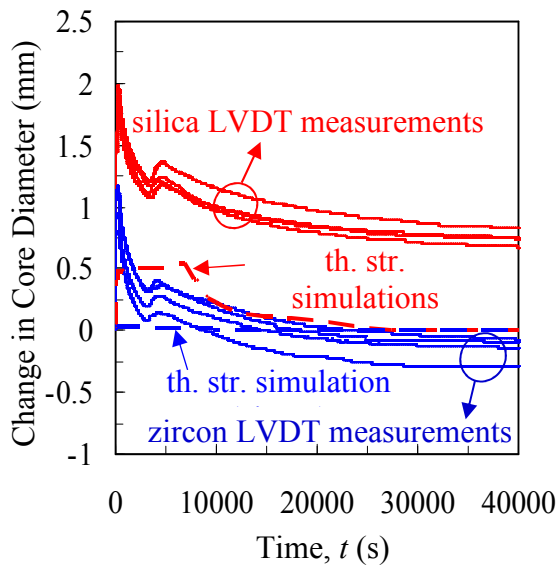
(a) Complete Time Scale   (b) 600 s Time Scale

Figure 5.2   Unconstrained expansions for the silica and zircon cores at the mid-height were predicted using the measured linear thermal expansions in (c).
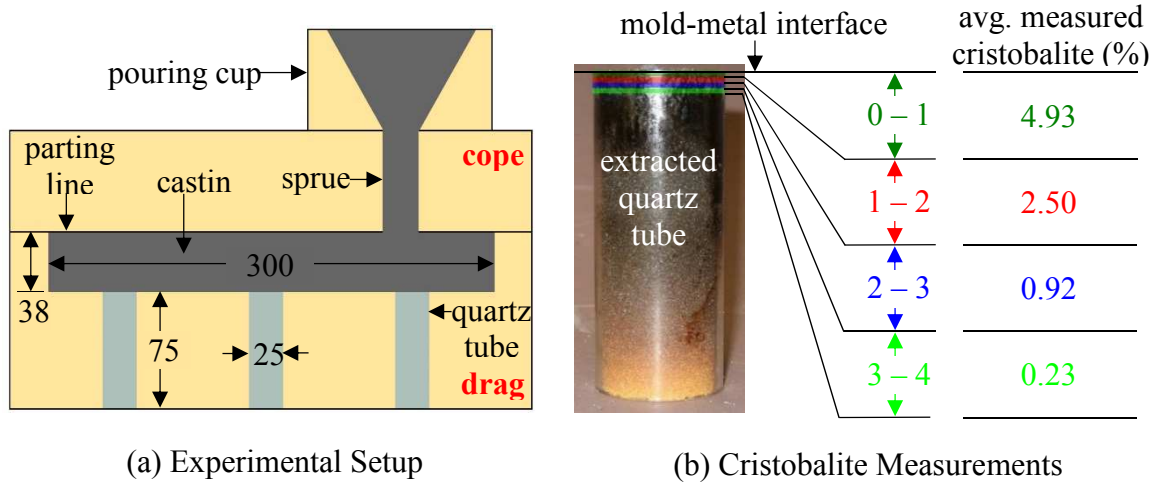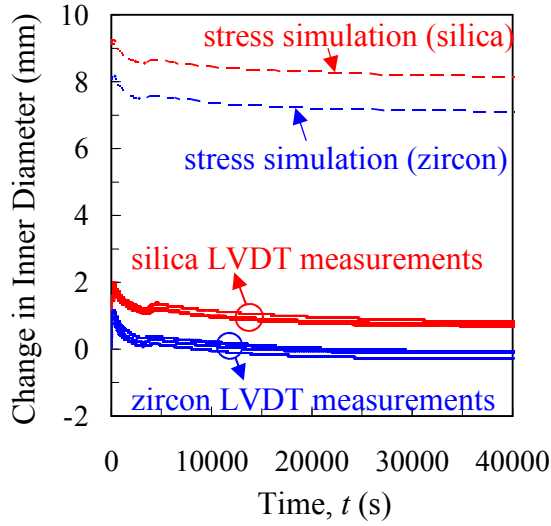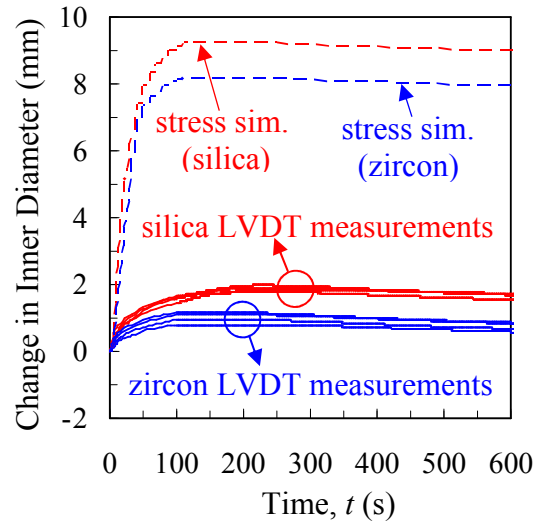
| (a) Experimental Setup | (b) Cristobalite Measurements |

Figure 5.3   Using the experimental setup depicted in (a), minimal amounts of cristobalite were measured from the silica sand contained the quartz tubes (b), which were extracted after the casting cooled to room temperature. All dimensions in mm.
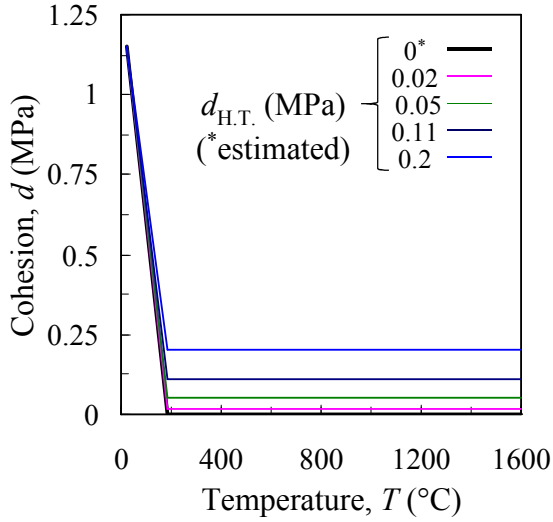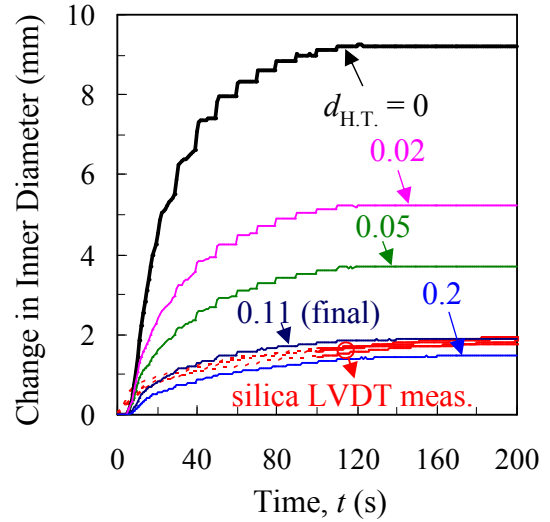
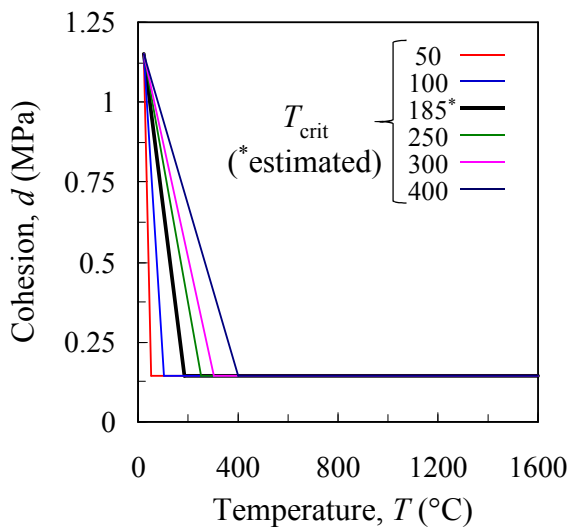(a) Complete Time Scale   (b) 600 s Time Scale

Figure 5.4   Predicted change in inner diameter using the estimated bonded sand properties shown on complete (a) and 600 s (b) time scales.
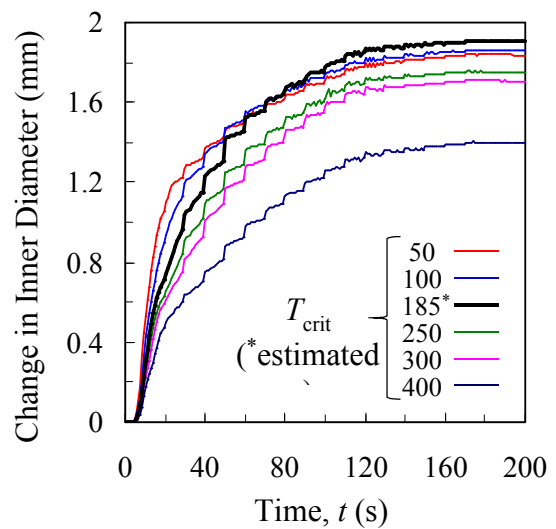
(a) Cohesion Parameter

(b) Effect of $d_{H.T.}$ on Silica Core Expansion
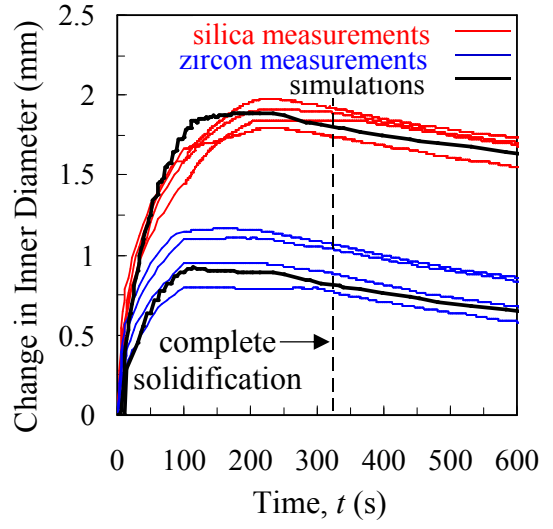
(c) Cohesion Parameter

(d) Effect of Critical Temperature on Silica Core Expansion

Figure 5.5 The high temperature cohesion parameter ($d_{H.T.}$), was adjusted (a) to match the simulated change in inner diameter to the measurements (b). The effect of variations in the critical temperature, T_{crit}, (c) on the predicted change in inner diameter (d) was investigated.
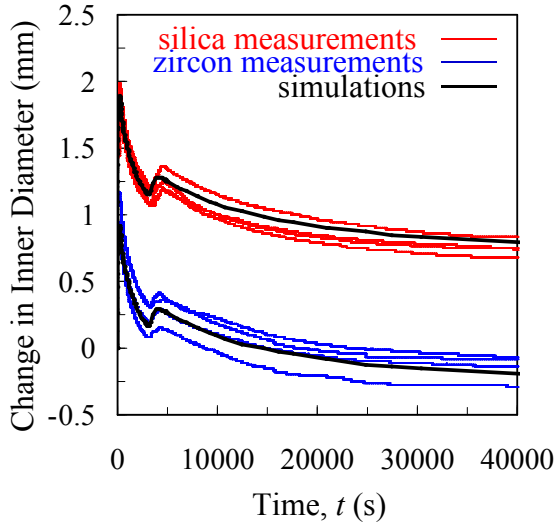
(a) Complete Time Scale   (b) 600 s Time Scale

Figure 5.6   Measured and predicted changes in the inner diameter were matched by adjusting the high temperature cohesion parameter, $d_{H.T.}$.
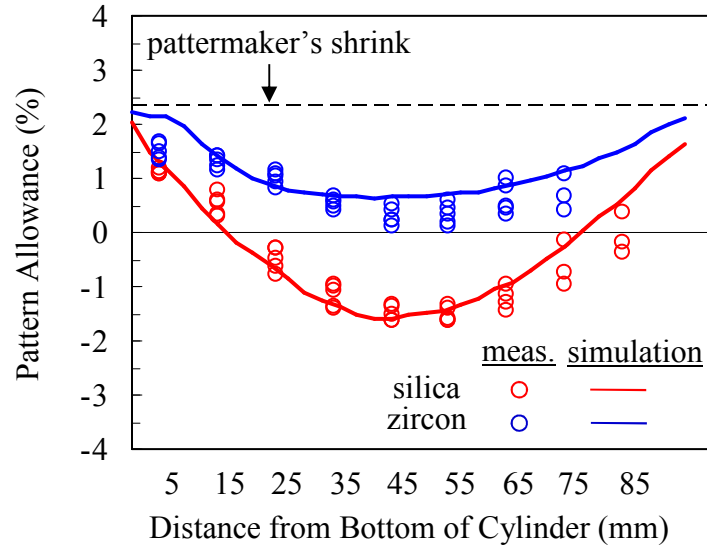
73

Figure 5.7   Comparison between measured and predicted pattern allowances.
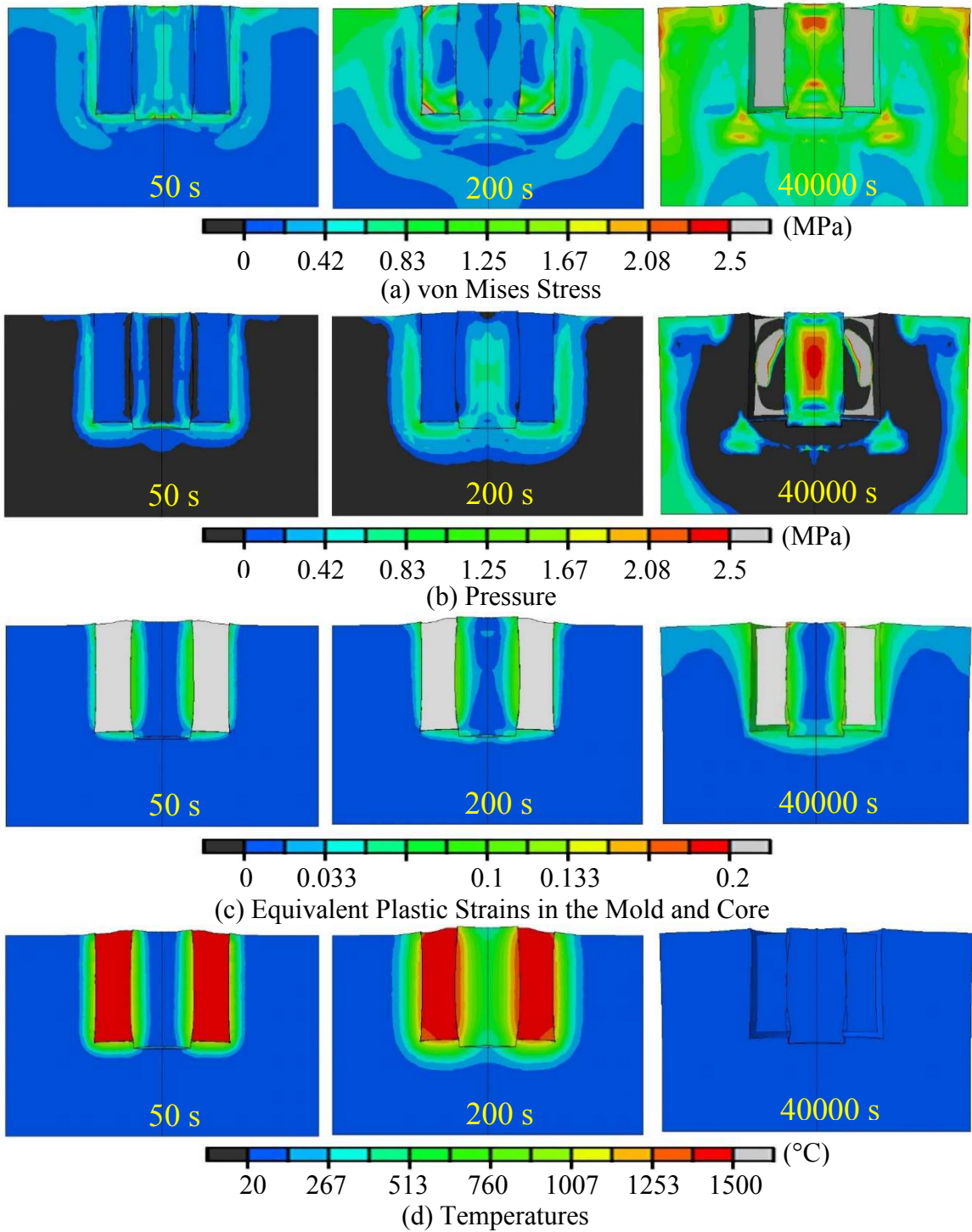
Figure 5.8   Contours of von Mises stress (a), pressure (b), equivalent plastic strains (c), and temperatures (d) at 50 s, 200 s, and 40,000 s (room temperature) for the silica core experiments. Distortions magnified by a factor of 5.

75

Table 5.1 Adjusted mechanical properties and Drucker-Prager Cap parameters for the silica bonded sands.

Temperature (ºC)	E (MPa)	v	p_{b0} (MPa)	β	d (MPa)	R	α
20	3403	0.3	2.4	55º	1.15	0.45	0.01
180	60	0.3	2.4	55º	0.11	0.45	0.01
1600	60	0.3	2.4	55º	0.11	0.45	0.01

Table 5.2 Adjusted mechanical properties and Drucker-Prager Cap parameters for the zircon bonded sands.

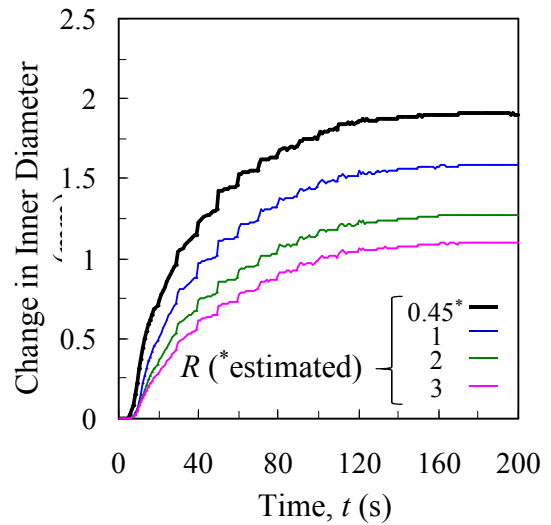| Temperature (ºC)	E (MPa)	v	p_{b0} (MPa)	β	d (MPa)	R	α
20	3403	0.3	2.3	55º	1.15	0.45	0.01
180	60	0.3	2.3	55º	0.08	0.45	0.01
1600	60	0.3	2.3	55º	0.08	0.45	0.01
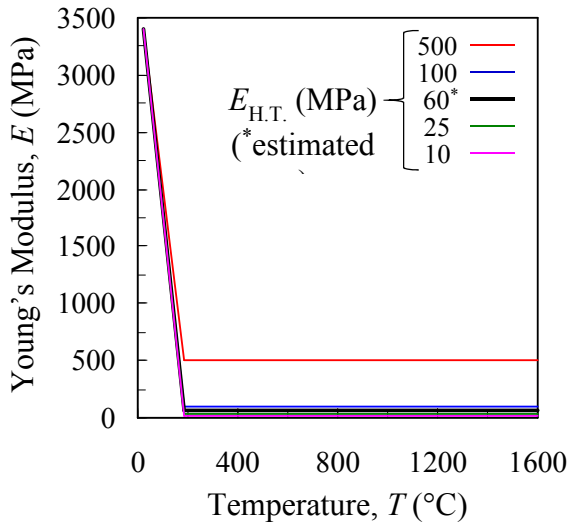
(a) Young's Modulus
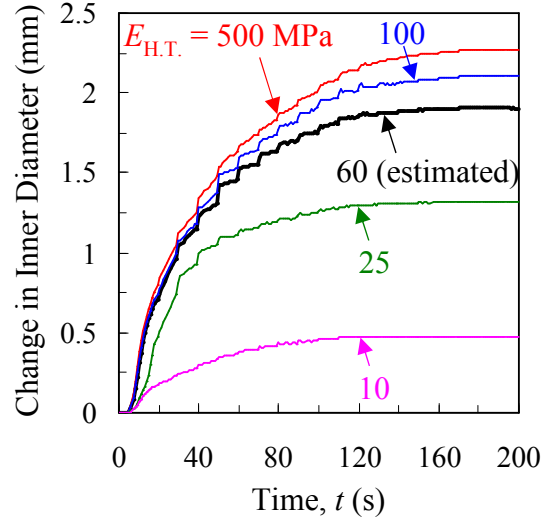
(b) Change in Inner Diameter
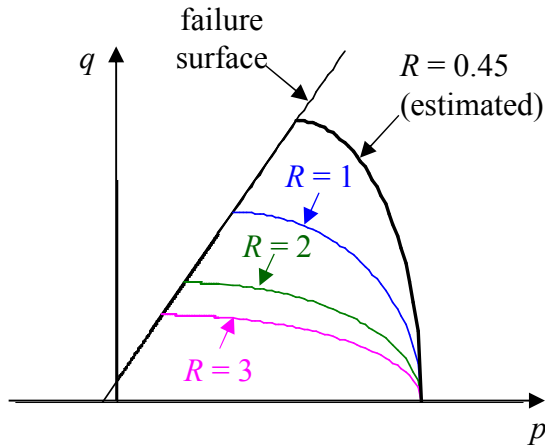
(c) Cap Eccentricity

(d) Change in Inner Diameter

Figure 5.9   Parametric studies showing the effect of high temperature Young's modulus ($E_{H.T.}$) and cap eccentricity (R) on the predicted change in inner diameter for the silica core experiments.
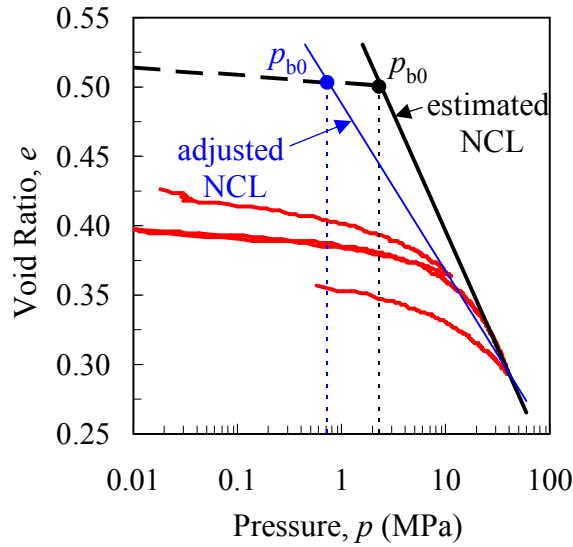
(b) Adjustment to Slope of
Normal Consolidation Line
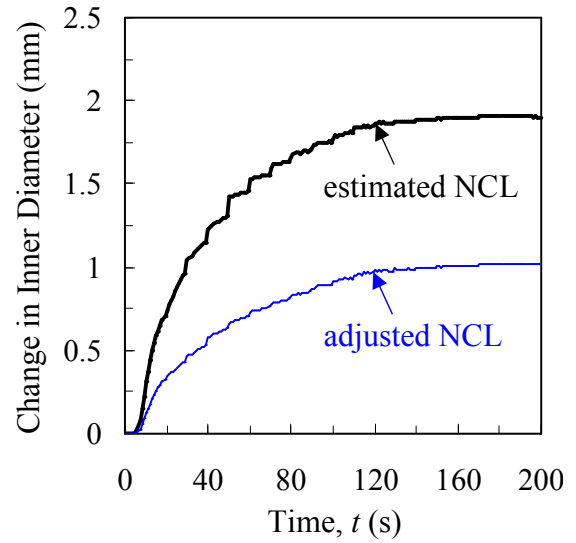
(a) Effect of Changes in Normal
Consolidation Line Slope
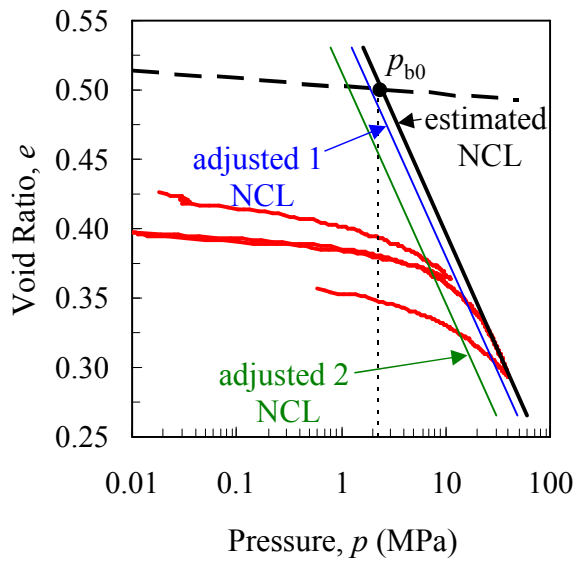
(d) Shifted Normal
Consolidation Lines
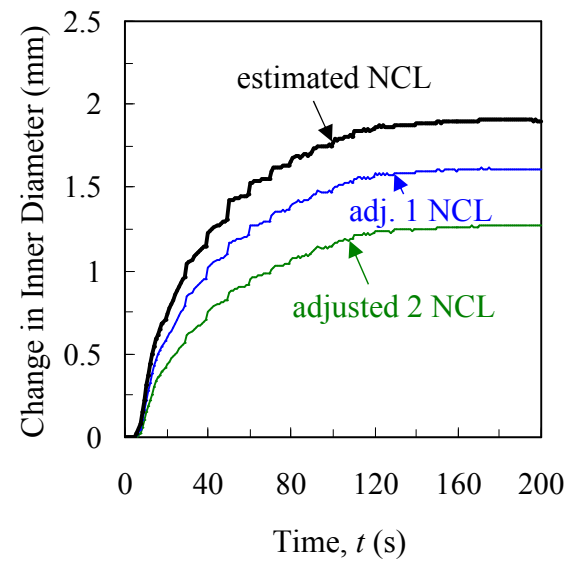
(c) Effect of Shifting the Normal
Consolidation Line

Figure 5.10   Parametric studies demonstrated the effect of variations in the normal consolidation line (NCL) for the silica core experiments.
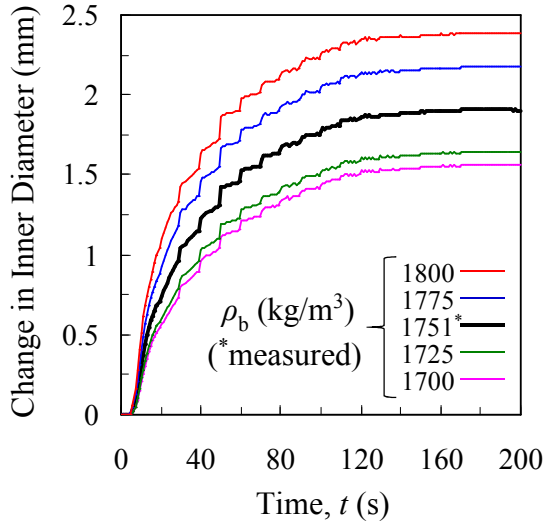
(b) Initial Bulk Density
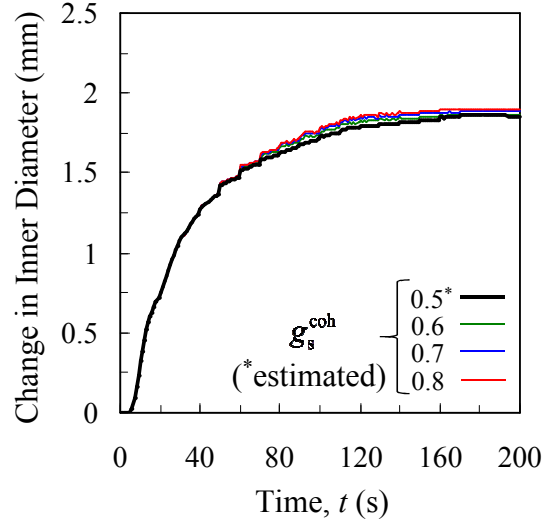
(d) Coherency Solid Fraction

Figure 5.11   Parametric studies demonstrated the effect of the initial bulk density (a) and coherency solid fraction (b) on the predicted change in inner diameter for the silica core experiments.

79
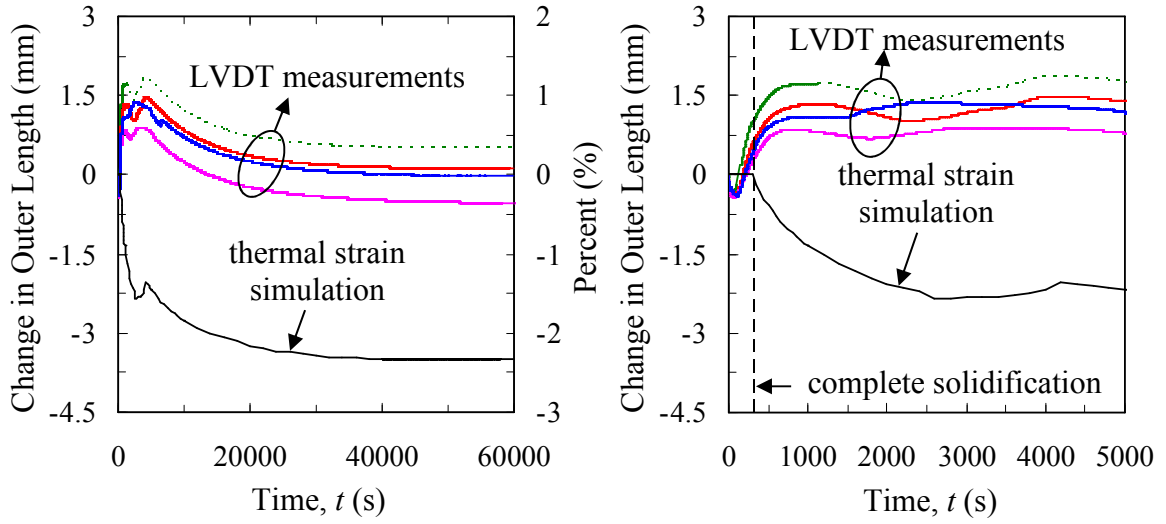
(a) Complete Time Scale

(b) 3000 s Time Scale
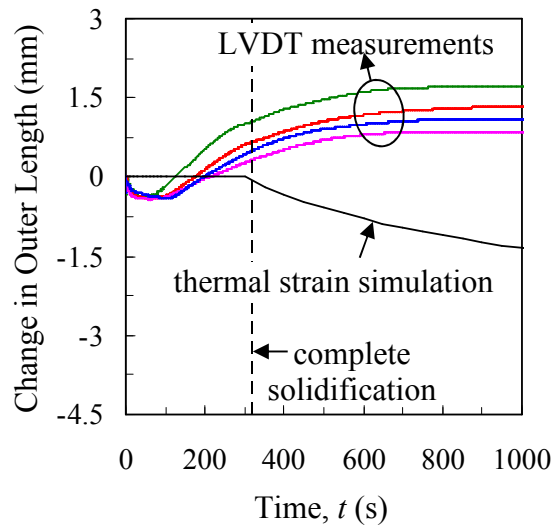
(c) 1000 s Time Scale

Figure 5.12   Predicted change in outer length due to thermal strains in the steel.
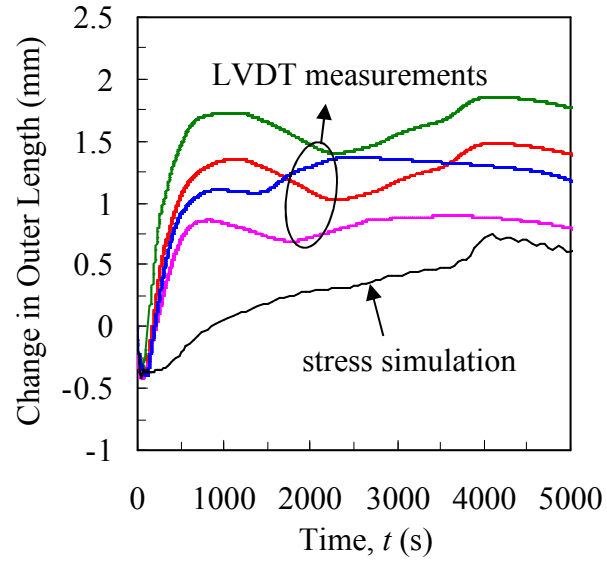
Figure 5.13   Comparison between measured and predicted changes in inner outer length using estimated bonded sand properties.
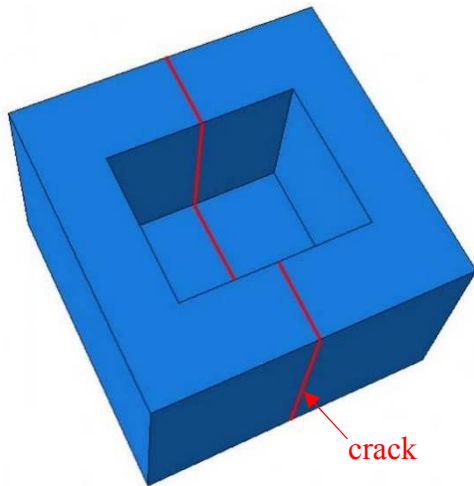
(a) Observed Crack Plane in Drag
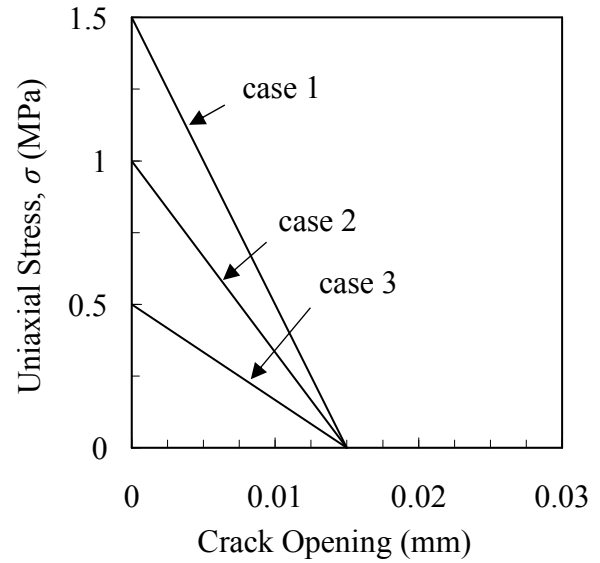
(b) Softening Behavior of Crack Plane
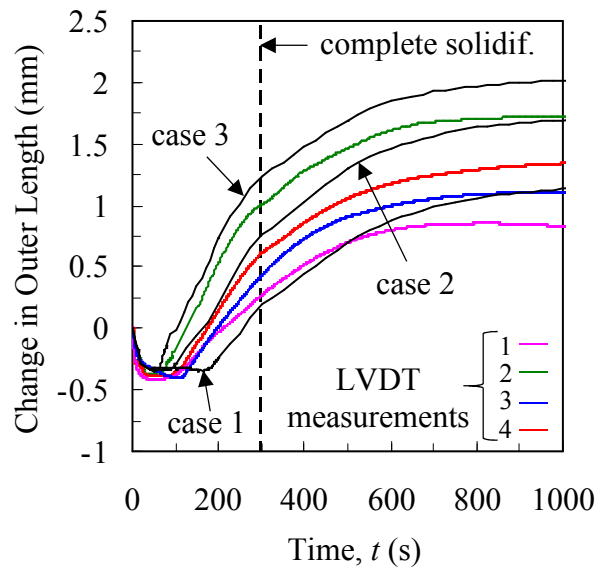
(c) 1000 s Time Scale

Figure 5.14 A crack plane (a) was modeled using softening behavior shown in (b). Sensitivity of the predicted push-out of the legs to the fracture strength is shown on 2500 s (c) and 1000 s (d) time scales.

82

distributed load to account for pouring
cup and steel in pouring cup

crack plane
contact surface
($\mu = 0.4$)

symmetry plane

$u_x = u_y = u_z = 0$ for bottom surfaces
of refractory bricks

(a) Front View

(b) Back View
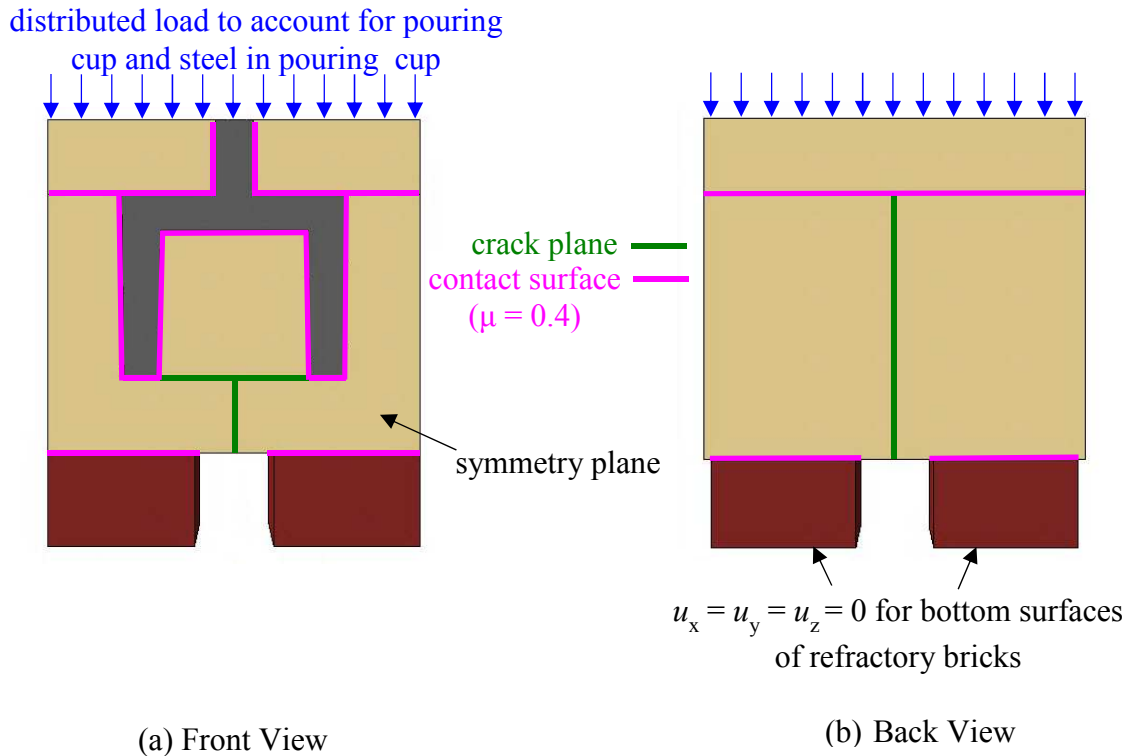
Figure 5.15   The finite element model was modified to include crack planes (green lines). Interactions between the casting, mold, and bricks were defined as contact surfaces (pink lines). Body forces were included.
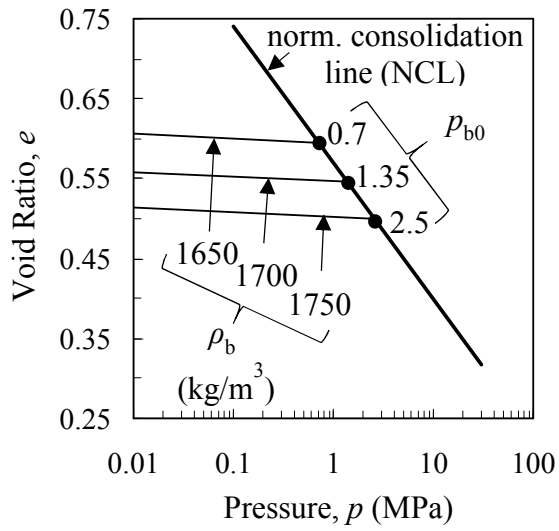
(a) Void Ratio (e) vs. log p
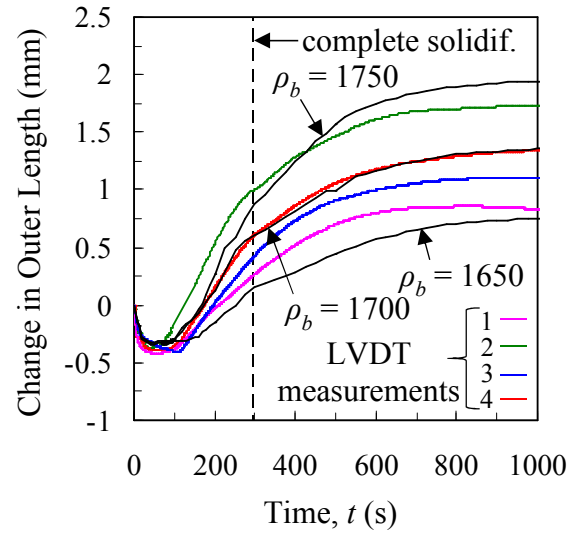
(c) 1000 s Time Scale

Figure 5.16   The room temperature bulk density has a strong effect on the predicted push-out of the bracket legs.

84
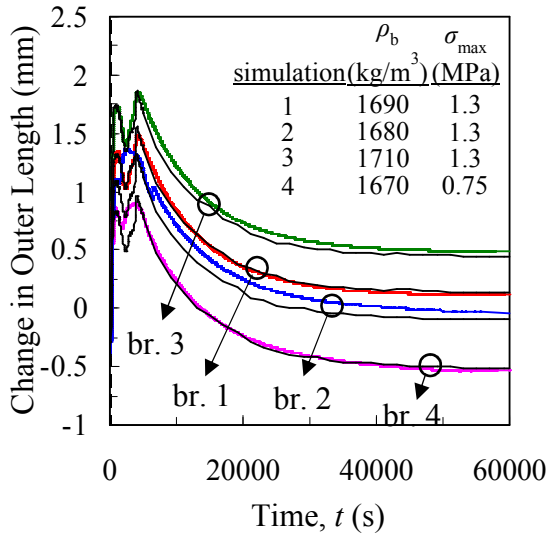
(c) 60000 s Time Scale
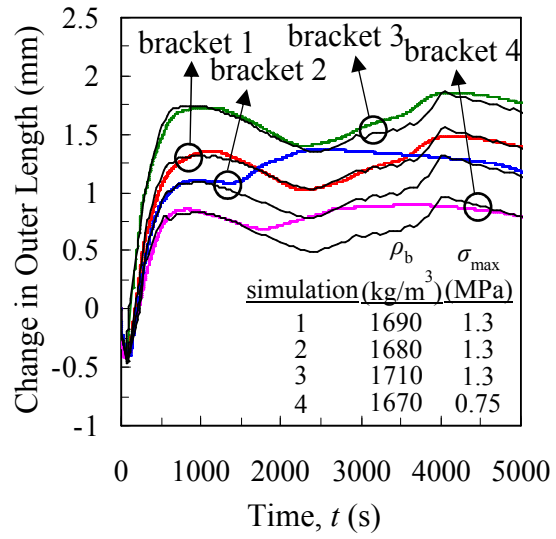
(c) 5000 s Time Scale
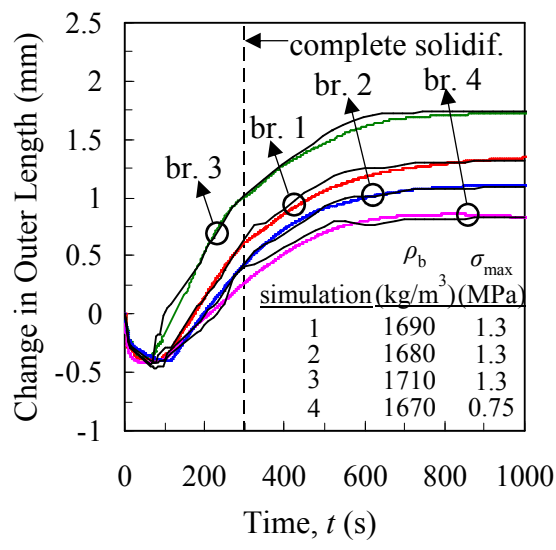
(c) 1000 s Time Scale

Figure 5.17   Final stress simulations for brackets.
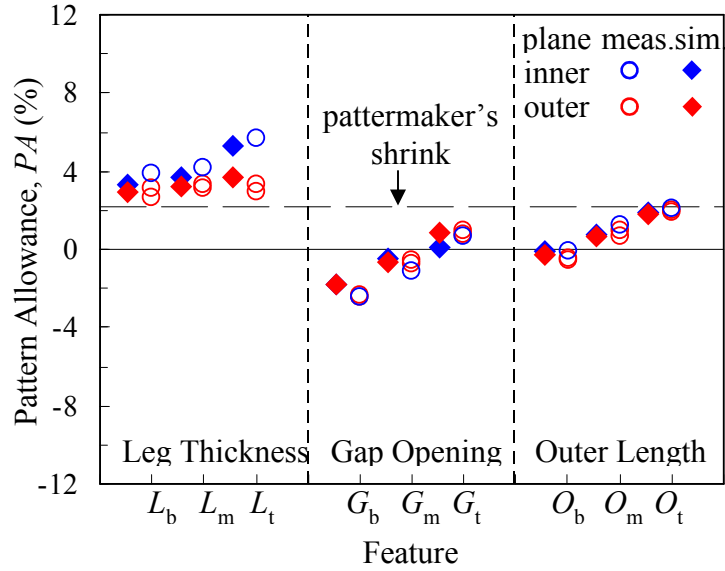
(a) Comparison between Measured and
Predicted Pattern Allowances for Bracket 1
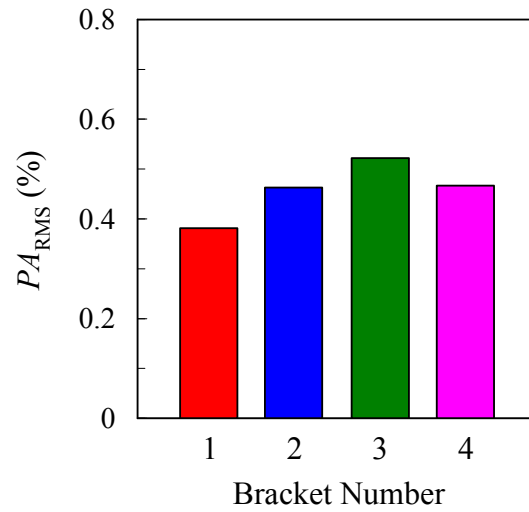
(b) Root Mean Square Error of
the Predicted Pattern Allowances
for all Brackets

Figure 5.18   Comparison between the average simulated and measured pattern allowances using bracket 1.

(a) von Mises Stress (units in MPa)

(b) Equivalent Plastic Strains in mold on the Drucker-Prager Shear Failure Surface

(c) Equivalent Plastic Strains in mold on the Drucker-Prager Cap Surface

(d) Equivalent Plastic Strains in the Bracket
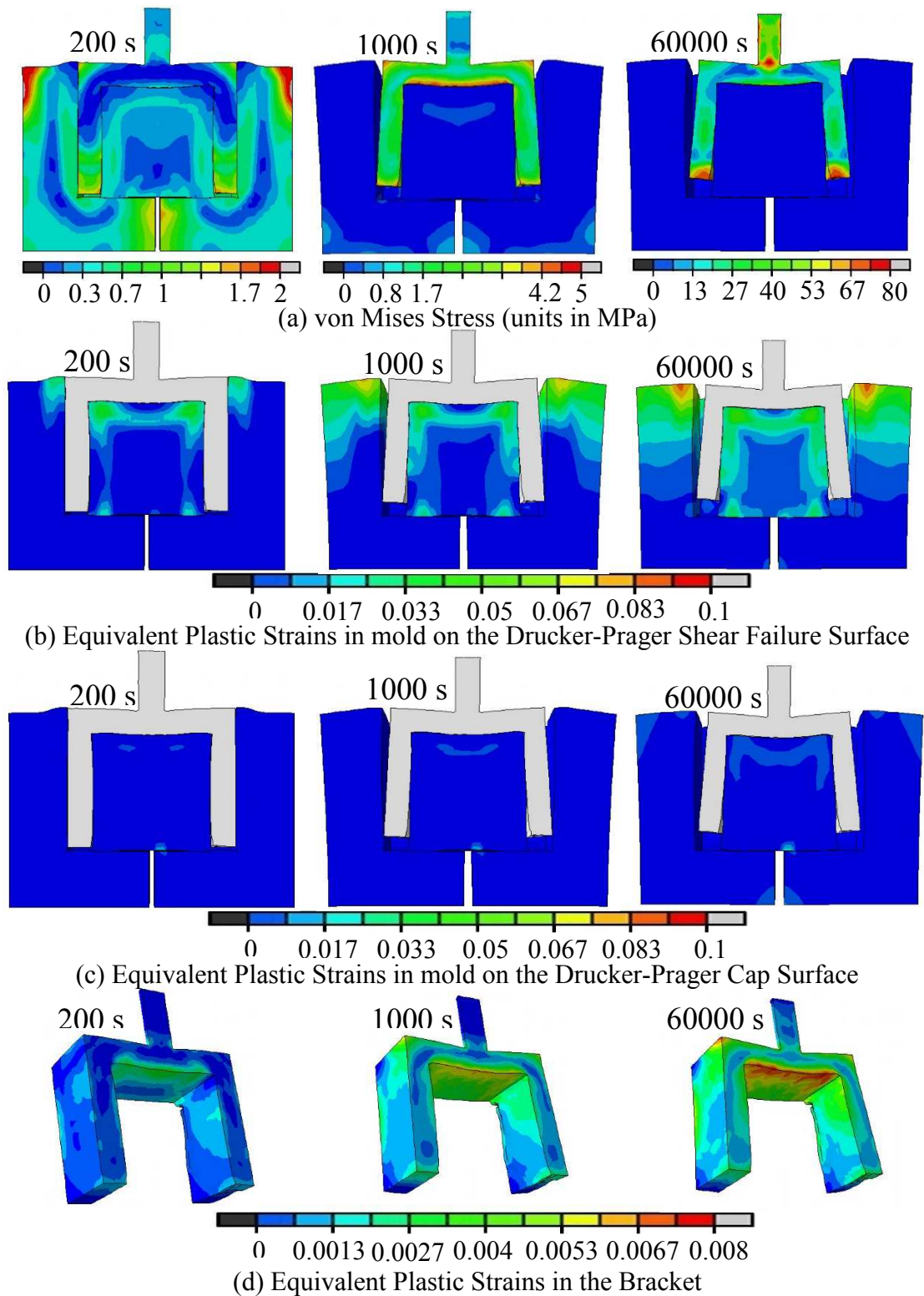
Figure 5.19 Contours of von Mises stress (a), equivalent plastic strains for the shear failure surface (b), and equivalent plastic strains for the cap surface (c) at 200 s, 1000 s, and 60,000 s (room temperature) for the bracket experiments. Distortions magnified by a factor of 5.

87

CHAPTER 6: CASE STUDY FOR A PRODUCTION STEEL CASTING

6.1 Introduction

The part to be analyzed is a drag socket, which is used on a mining excavator to splice cables together. It was cast at the Bradken foundry in London, Ontario. The casting (shown in Figure 6.1) has outer dimensions (in meters) of $1.91 \times 0.29 \times 0.6$ ($6.27 \times 0.95 \times 1.97$ ft) and weighs approximately 940 kg (2068 lbs). The drag socket contains several characteristics that makes it susceptible to distortions. For example, cores are needed to create the hollow interior of the main body as well as the two holes on the right side of Figure 6.1(b). Uneven cooling is also likely to generate distortions in the varying section thicknesses of the casting as well as the gating and risers (which are not shown).

6.2 Description of Part

A dimensional analysis was performed after shakeout, for which several casting features were measured. Using these measurements, pattern allowances (PA) were then calculated using the Eq. 1. In total, ten features were selected from the part drawing and are numbered in Figure 6.1. The measured pattern allowances are summarized in Figure 6.2. Features 1, 2, 4, and 8 have pattern allowances greater than the patternmaker's shrink. This result can be explained by mold expansion. From Figure 6.1, it can be seen that these features are measured on the outer surface of the casting. During solidification, the rapidly heating mold expands and pushes the outer walls of the casting inward to reduce feature lengths (i.e., pattern allowances are increased). These features are unconstrained and therefore, will shrink an additional 2.1% (i.e., the patternmaker's shrink) after the initial "push-in" of the outer walls, resulting in pattern allowances greater than the patternmaker's shrink. Similarly, features 3, 7, and 10 are also measured from the outer surface and can be expected to experience a reduction in length during solidification. However, these features are also influenced by core restraint. In contrast to mold expansion, distortions created from core restraint increase the feature lengths (i.e., reduce pattern allowances). Therefore, for

88

features 3, 7, and 10, distortions created by mold expansion and core restraint distortions cancel each other out to some degree. For these situations, the pattern allowances should be viewed with caution; even if the patternmaker's shrink is measured, significant distortions may have occurred but are hidden due to the "canceling out" explained above. Therefore, although the measured pattern allowances are close to the patternmaker's shrink for features 7 and 10 (1.95%), larger distortions may have occurred and potentially caused damage in the part. For situations in which features are measured on internal surfaces (i.e., features 5, 6, and 9), mold expansion increases the feature lengths (i.e., reduces pattern allowances). For example, mold expansion will expand the diameter of the large hole (feature 5) in Figure 6.1. Because core restraint will also expand the diameter, pattern allowances for features measured on internal surfaces should always be less than the patternmaker's shrink. This is indeed the case for this study, as the maximum pattern allowance of features 5, 6, and 9 is 0.62%. Because the features are affected by different phenomena and in different ways, their pattern allowances vary over a large range, as seen in table 1 ($-0.89 < PA < 3.11$). For validation purposes, this variation is desirable for this case study.

6.3 Thermal Simulations

Temperatures were predicted using the casting simulation software package MAGAMSOFT®. The input parameters for the simulation (including temperature dependent thermophysical properties for the mold and casting, solid fraction, latent heat, and interfacial heat transfer coefficient) are summarized in chapter 4 (see Figure 3.1 - Figure 3.3). All components of the casting system (i.e., mold, casting, cores, risers, chills, etc.) were included in the simulation. Predicted temperature fields were output at a sufficient number of time steps to give a smooth temperature profile at every location in the model. The results were copied onto the finite element mesh used in the stress simulations.

89

6.4 Stress Simulations

To predict distortions, stress simulations were performed using the general purpose finite element code ABAQUS®. The mold, gating, and risers were included in the simulations, as they their contributions to distortions could not be discounted. However, in order to protect the confidentiality of the casting design, these components will not be shown in the results. The constitutive models for the steel and bonded sands is described in chapter 5. Due to its complex geometry, tetrahedral elements were used to build the mesh. The model contained approximately 200,000 nodes and 1.1 million elements.

To quantify the distortions created by each phenomenon (i.e., mold expansion, core restraint, uneven cooling), three simulations were performed. The first simulation (termed "thermal") calculated thermal strains only. The pattern allowances predicted in this simulation are equal to the patternmaker's shrink. The thermal simulation serves as a baseline; any predicted feature length that deviates from that in the thermal simulation is a distortion. In the second simulation (termed "casting only"), the outer mold was excluded. Here, distortions due to mold expansion and core restraint are not considered. Thus, distortions can only be created by uneven cooling in this simulation. The third simulation (termed "full") includes the complete casting system and therefore, considers all the phenomena responsible for distortions. The predicted pattern allowances from this simulation will be compared to the measurements to determine the predictive capability of the computational model.

6.5 Results and Discussion

Predicted temperature contours from the thermal simulations are shown at 500 s and 5000 s in **Error! Reference source not found.**. Large temperature gradients can be seen throughout the casting at both times. For example, the body of the casting (left side of **Error! Reference source not found.**) cools much faster than the section near large hole on the right side. After 500 s, temperatures throughout the casting range from

90

approximately 900°C to over 1400°C. Even after 5000 s (~1.5 hours), temperatures vary by over 400°C. As a result of these variations, distortions can be expected from this uneven cooling.

The deformed shape at room temperature predicted by the finite element stress simulation is shown in Figure 6.4. The deformations are magnified by a factor of 10. The distorted shape (green) is overlaid onto the undeformed shape to illustrate where distortions occur. For example, the arm on the right side is distorted outward. Most likely, the mold impedes the thermal contractions to generate this distortion. However, uneven cooling could also have an impact. The predicted pattern allowances (shown below) will give insight to which the responsible phenomenon. Also, the holes on the right side of the casting appear to be enlarged. This is expected, as mold expansion and core restraint both can be expected to contribute to distortions of these features.

The predicted temporal evolution of feature length 3 (location shown on Figure 6.1) is plotted on complete (400,000 s) and 5000 s time scales in Figure 6.5. The complete time scale represents the time needed to cool the casting to room temperature. For the thermal simulation (shown as the green curve), the feature length begins decreasing at approximately 500 s, which represents the approximate solidification time and is denoted by the vertical dashed line in Figure 6.5(b). Between 500 and 400,000 s, feature length 3 decreases approximately 41.5 mm, as seen on the complete time scale in Figure 6.5(a). This decrease occurs in the absence of distortions and represents the patternmaker's shrink. The increase in length change between 40,000 and 50,000 s is due to the solid state phase transformation from austenite to pearlite and ferrite. Differences between the casting only simulation (pink curve) and the thermal simulation can be seen beginning at 500 s. The curves gradually diverge until the end of the solid state phase transformation (at 50,000 s), after which the difference between the curves (approximately 4 mm) remains constant. Because the mold is not included in this simulation, this difference is due to uneven cooling, which distorts the arm inward. Therefore, the outward distortion observed in

91

Figure 6.4 must be caused by mold/core restraint. For the full simulation (blue curve), the length change during the initial 500 s (approximately -2 mm) is created by mold expansion. This expansion occurs during solidification. Once solidified, the casting has gained sufficient strength to resist any farther push-in from the mold. Beginning at 500 s, the full simulation feature length decreases at a slower rate than the thermal simulation feature length. This reduced contraction rate is due to core/mold restraint, which impedes thermal contractions and causes the feature to decrease at a slower rate than if it were unconstrained. As a result, the thermal and full simulation curves converge beginning at 500 s until they predict the same length change at 1000 s and then diverge until the beginning of the solid state transformation (~35,000 s). Throughout this time period, considerable distortions are generated by core/mold restraint. After the solid state transformation is complete (~50,000 s), the feature lengths in the full and thermal simulation contract at the same rate, signifying that no distortions are predicted after 50,000 s. When the casting has cooled to room temperature (after approximately 400,000 s), the full simulation has reduced in length by 34 mm (see Figure 6.5(a)). This value is very close to the measured reduction of feature length 3, which is denoted by the symbol in Figure 6.5(a) at 400,000 s.

Similar plots for feature 5 are shown in Figure 6.6. Very little difference can be seen between the thermal and casting only curves, which indicates that distortions created by uneven cooling are negligible for this feature. Also similar to feature 3, the solidification time occurs at approximately 500 s. Prior to 500 s, mold expansion increases feature length 5 by approximately 2.5 mm (see the full simulation curve in Figure 6.6(b)). This result is in contrast to mold expansion for feature 3, for which mold expansion causes a decrease in the length. Recall that this is because feature length 3 is measured on the outer casting surface, whereas feature length 5 is measured on an internal surface. After feature 3 expands to a maximum value at 2000 s, its length decreases at the same rate as the thermal simulations, indicating that no distortions are predicted after 2000 s.

Through the analysis performed on feature lengths 3 and 5, several conclusions can

92

be drawn. First, mold expansion considerably impacts feature lengths at early times. The features may either increase or decrease in length depending where they are located on the casting surface. Core/mold restraint also has a significant impact on features and always leads to increased feature lengths (i.e., decrease in pattern allowances). Finally, no distortions were predicted after the solid state phase transformation. This is not unreasonable, as the solid state phase transformation is associated with a significant increase in the casting strength.

Comparisons between all predicted pattern allowances are compared to the measurements in Figure 6.7. In general, the pattern allowances were predicted with good accuracy. The free shrink line is denoted by a dashed horizontal line and represents the predicted pattern allowances using the patternmaker's shrink. All of the pattern allowances (measured and predicted) are different from the free shrink. In other words, every feature chosen for this study has some amount of distortion associated with it. These distortions increase the pattern allowances for some features and decrease them for others. Even for situations where the predicted pattern allowances don't agree with the measurements, they predict the correct trends.

The difference between the measured and predicted pattern allowances determines the accuracy of the model. Clearly, some features were predicted more accurately than others, which can make it difficult to evaluate the overall performance of the simulation. As a solution, a suitable figure of merit that combines the predicted pattern allowances of all features into a single value should be used. However, because pattern allowances can either be positive or negative, simply taking the average of all values is not appropriate. For such cases, the root mean square (RMS) can be used. The RMS is defined as

$$PA_{RMS}[\%] = \sqrt{\frac{1}{n}\sum_{i=1}^{n}\left(PA_{measured} - PA_{predicted}\right)^2} \qquad [21]$$

where n is the number of features, and $PA_{measured}$ and $PA_{predicted}$ are the measured and predicted pattern allowances, respectively. This number can be viewed as the average difference between measured and predicted pattern allowances. For the simulation, $PA_{RMS} = 0.29\%$. This small value demonstrates that the simulation predicts the pattern allowances with very good accuracy. Using the RMS value, the performance of different simulations can be compared.

Contours of equivalent plastic strain and von Mises residual stress (shown in MPa) are shown in Figure 6.8. Residual stresses are those that remain in the as cast part (i.e., before heat treatment) at room temperature. The largest residual von Mises stresses and strains occur in the body of the casting (on the left side in Figure 6.8). Considerable plastic strains are also predicted near the two holes in the casting arm (i.e., features 5 and 6). These areas of high residual von Mises stress and strain are near locations containing cores and thus, not unexpected.
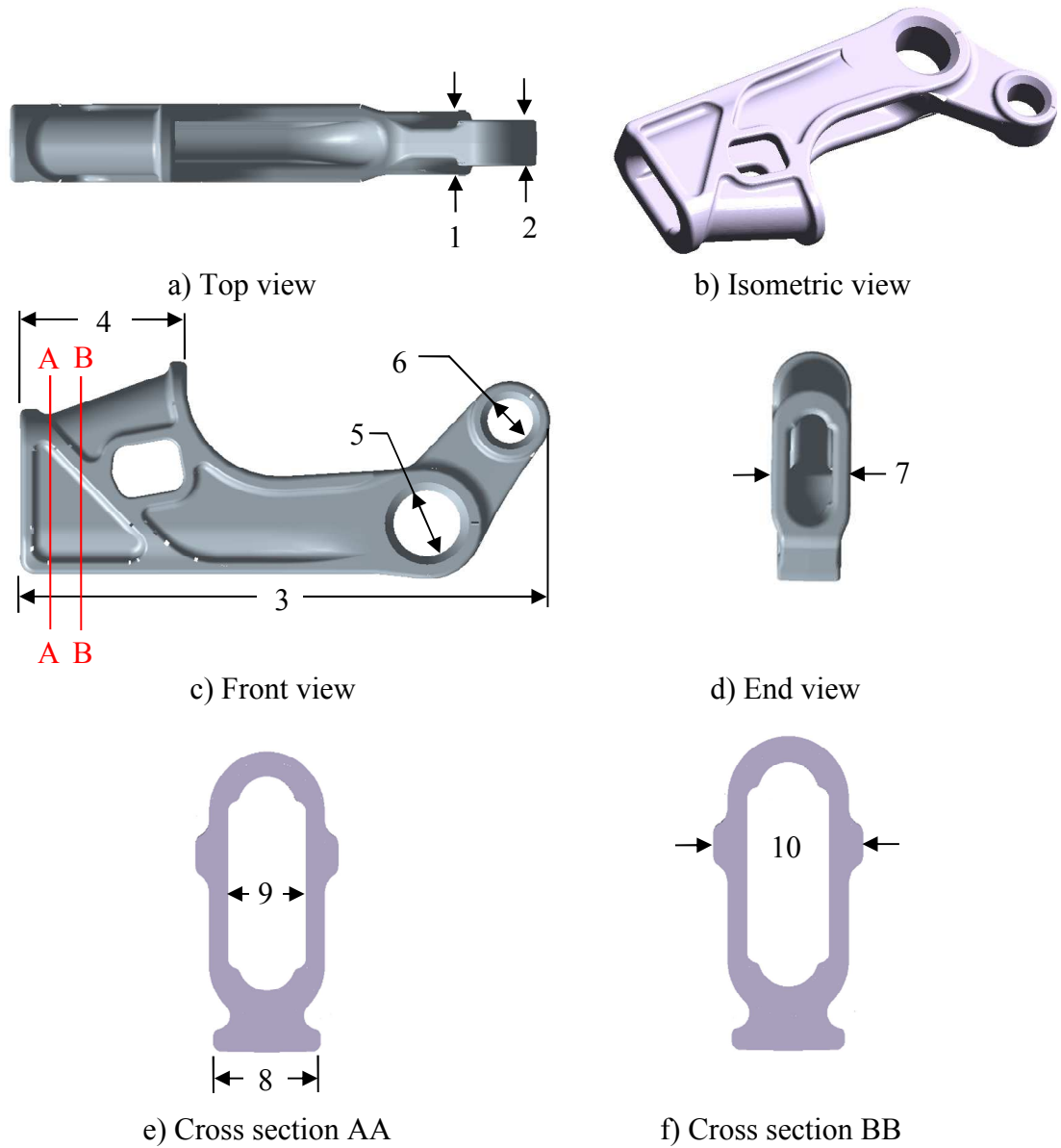
a) Top view

b) Isometric view

c) Front view

d) End view

e) Cross section AA

f) Cross section BB

Figure 6.1   Casting geometry and feature locations.
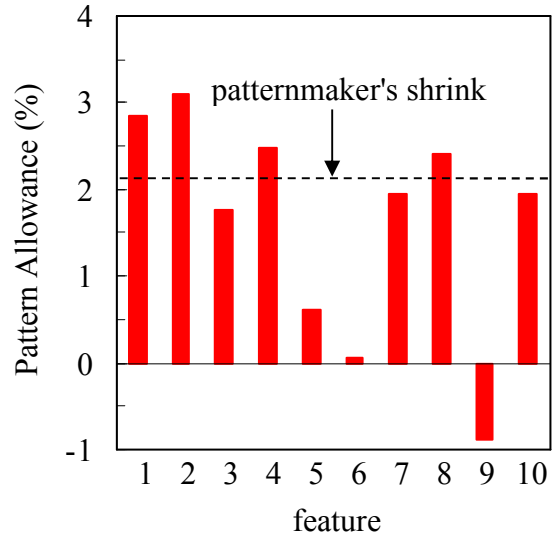
Figure 6.2   Measured pattern allowances.

Temperature (ºC)
(Avg: 75%)
+1.484e+03
+1.450e+03
+1.388e+03
+1.325e+03
+1.262e+03
+1.200e+03
+1.138e+03
+1.075e+03
+1.012e+03
+9.500e+02
+8.875e+02
+8.250e+02
+7.625e+02
+7.000e+02

a) 500 s

b) 5000 s
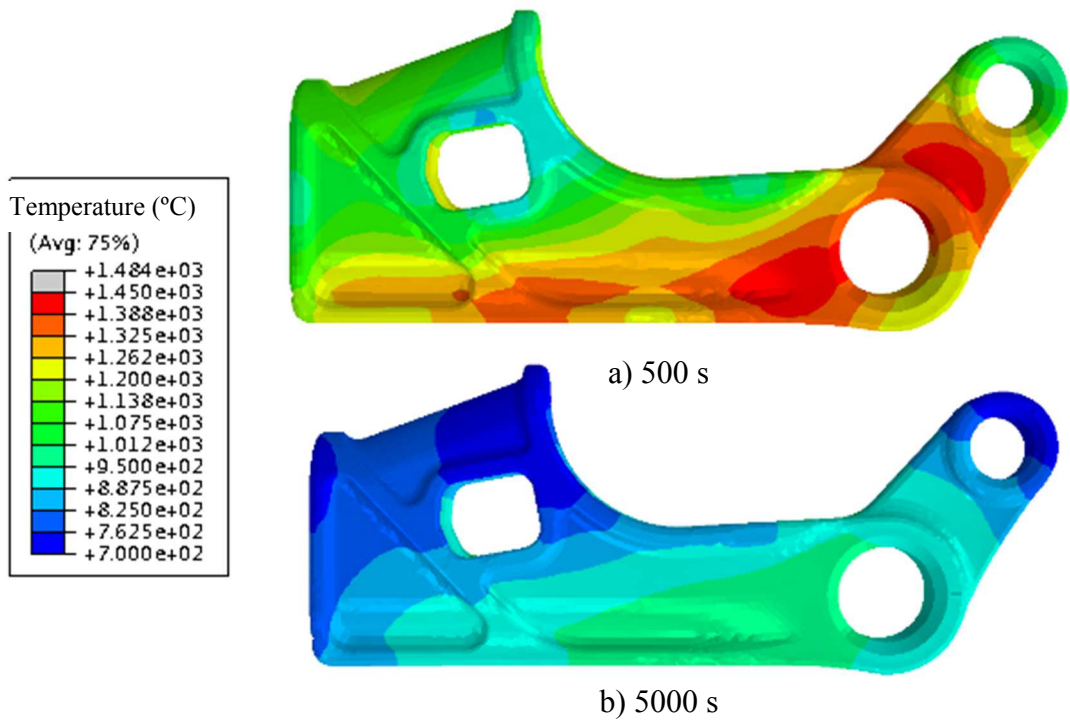
Figure 6.3   Predicted temperatures at 500 (a) and 5000 (b) s.

97

Figure 6.4 Deformed casting at room temperature.

a) Complete time scale

b) 5000 s time scale

Figure 6.5   The predicted length changes for feature length 3 shown on complete (a) and 5000 s (b) time scales. The complete time scale represents the time needed to cool the casting to room temperature.
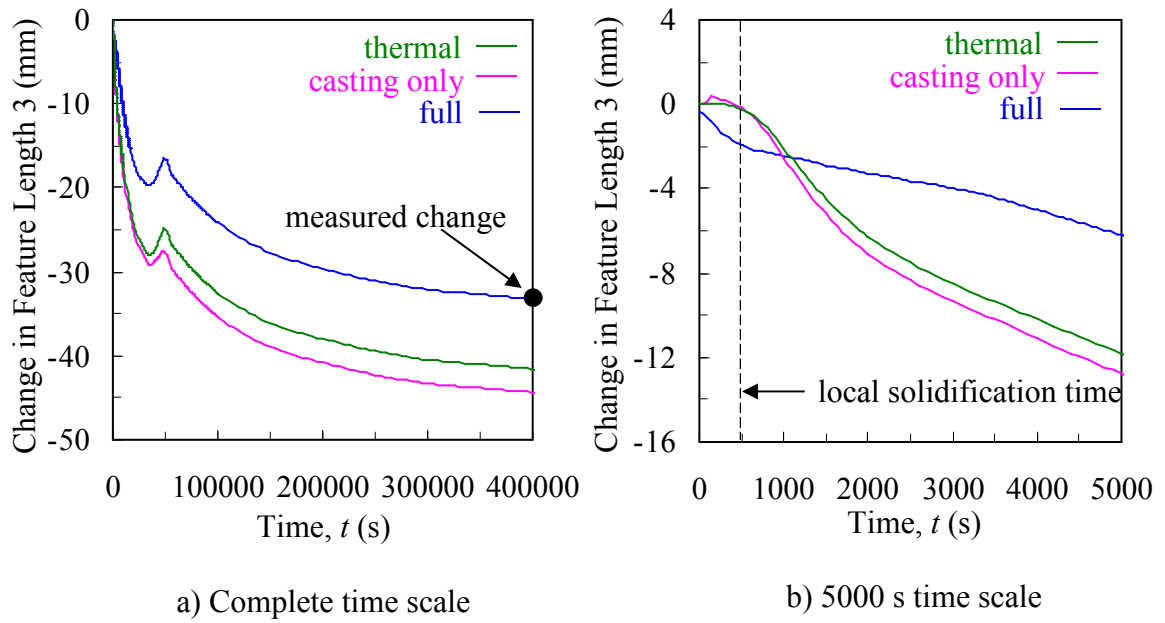
99

a) Complete time scale

b) 5000 s time scale
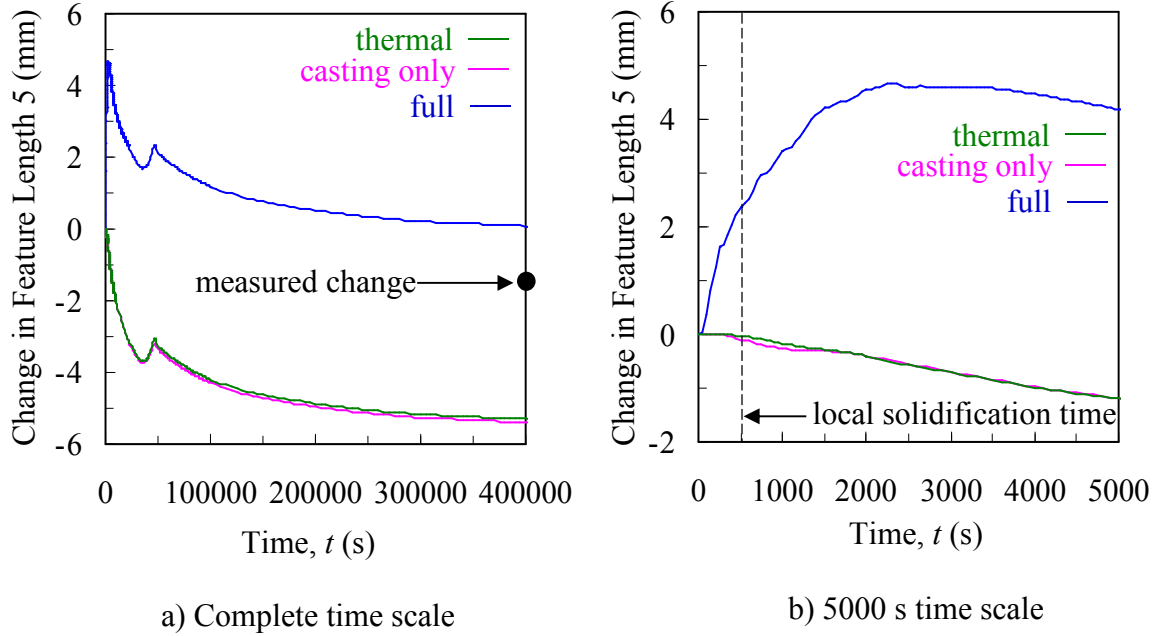
Figure 6.6   The predicted length changes for feature length 5 shown on complete (a) and 5000 s (b) time scales. The complete time scale represents the time needed to cool the casting to room temperature.

100
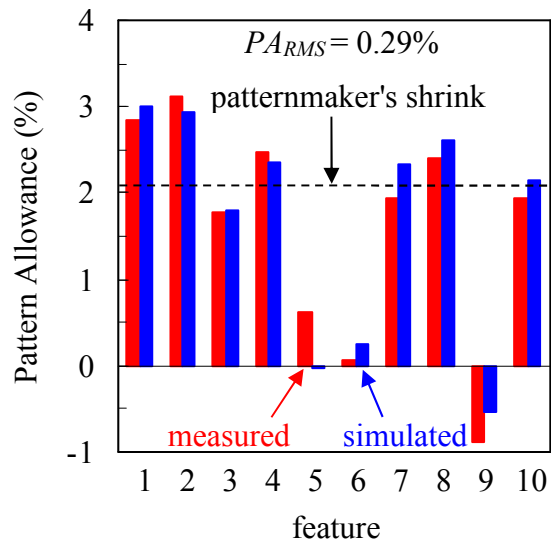
Figure 6.7   Comparison between measured and predicted pattern allowances. PA_{RMS} is the root mean square of the difference between predicted and measured pattern allowances.

a) Equivalent plastic strain

b) Residual von Mises stress

Figure 6.8   Predicted equivalent plastic strain and residual von Mises stress (units in MPa).

CHAPTER 7: CONCLUSIONS AND FUTURE WORK

7.1 Conclusions

In this study, the thermomechanical behavior of bonded sands was investigated for the purpose of predicting pattern allowances for steel sand castings. Two sets of *in situ* experiments involving a hollow cylinder and U-shaped brac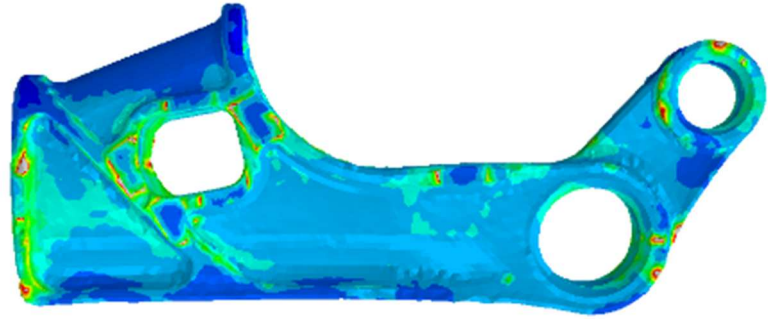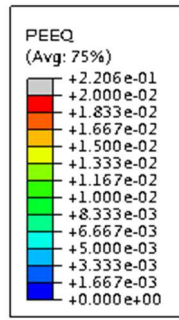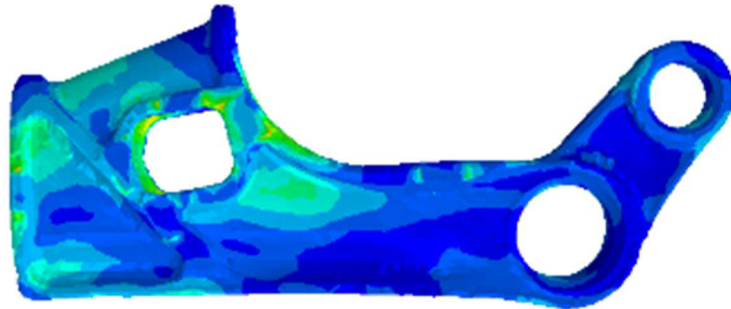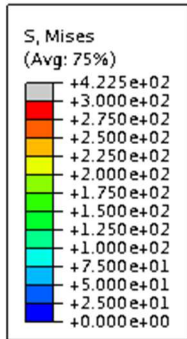ket were produced in sand molds to measure distortions created by core expansion and core restraint, respectively. For the cylinder experiments, distortions were generated by core expansion during solidification. However, the finite element simulations revealed that only a small amount of this expansion could be attributed to thermal expansion of the bonded sands. It was found that dilation must be considered. Otherwise, the observed core expansion could not be predicted. In order to predict dilation in the stress simulations, the Drucker-Prager Cap model was utilized for the bonded sands. Now the measured and predicted inner diameter evolutions could be matched. In addition, the barrel-shaped profile of the inner diameter that evolved during solidification was also predicted. For the bracket experiments, core restraint pushed the bracket legs outward, generating distortions. Using the model parameters calibrated for the cylinder experiments, stress simulations initially under-predicted distortions in the bracket, as the room temperature tensile strength of the bonded sands provided restraint and prevented the pushout of the bracket legs. It was found that the mold fracture that was observed during the experiments had a significant impact on the predictions. By implementing a crack plane into the model, the observed pushout was predicted. Finally, a case study for a production steel casting demonstrated excellent predictive capability of the computational model, as the root mean square between measured and predicted pattern allowances was 0.29%.

Accurate stress modeling for the bonded sands used in sand casting is of utmost importance for the prediction of distortions and pattern allowances. The present study has resulted in the development of a constitutive dataset that can be used to model the bonded

sands used for sand casting. Most importantly, it was found that unless sand dilation was considered, pattern allowance predictions were grossly inaccurate. The importance of mold fracture was also demonstrated. Although the significance of these physical phenomena have been exposed, additional work is still needed to address the uncertainties associated with the high temperature properties of the bonded sands. It is envisioned that the findings from this study will have an immediate impact on eliminating the inefficiencies and waste in industry.

7.2 Future Work

Due to the limitations of geological testing machines, no high temperature properties could be determined in this study (recall that the high temperature properties were estimated from room temperature un-bonded sands). This shortcoming raises questions concerning the validity of the high temperature properties for the bonded sands that were used in the simulations. Through a parametric study, several high temperature parameters, including Young's modulus, cohesion, and the cap eccentricity were shown to have a large impact on the predicted distortions. Based on these findings, it is obvious that the high temperature properties play a critical role determining an accurate solution. Future testing is needed to determine these properties. By devising high temperature apparatuses (i.e., triaxial tests, 1-D compression tests), the uncertainties associated with the high temperature properties can be mitigated, which in turn will lead to better predictions.

The mold fracture that was observed in the bracket experiments revealed a deficiency in the Drucker-Prager Cap model regarding the prediction of casting distortions. Upon yielding in tension, the Drucker-Prager Cap model predicts perfect plasticity. In other words, the tensile strength of the bonded sand remains constant for any amount of plastic straining. In reality, however, tensile yielding for bonded sand results in quasi-brittle failure, during which the tensile strength in the bonded sands degrades and is eventually eliminated. Modeling this behavior was found to be essential for the prediction of

104

distortions in the bracket experiments. For future work, a user material subroutine will be needed to reflect this brittle behavior. By modifying the Drucker-Prager Cap model to include a tension cap, the effect of mold fracture can be included in the model. Yielding on the tension cap would cause it to translate inward and reduce the tensile strength, thus providing a mechanism to simulate the cracking. A constitutive relation employing fracture mechanics techniques could also be explored. However, implementation of such a material model would be more difficult than adding the tension cap.

REFERENCES

1. R. Voigt, Pennsylvania State University, personal communication, 2012.

2. R.N. Parkins and A. Cowan: *Proceedings of the Institute of British Foundation*, paper no. 1062, pp. A101-9, 1953.

3. C.S.E. Mkumbo, B.B. Nyichomba, J. Campbell and M. Tiryakioglu: *Int. J. Cast Metals Res.*, 2002, vol. 14, no. 4, pp. 225-34.

4. B.B. Nyichomba, I.M. Cheya and J. Campbell, *Int. J. Cast Metals Res.*, 1998, vol. 11, pp. 179-86.

5. B.B. Nyichomba and J. Campbell, *Int. J. Cast Metals Res.*, 1998, vol. 11, pp. 163-7.

6. Y. Inoue, Y. Motoyama, H. Takahashi, K. Shinji, and M. Yoshida: *J. Materials Processing Techology*, 2013, vol. 213, pp. 1157-65.

7. C. Monroe, and C. Beckermann: *61st Steel Founders Society of America Technical and Operating Conference*, paper no. 5.7, Steel Founders' Society of America, Chicago, IL, 2006.

8. F. Peters, R. Voight, S.Z. Ou, and C. Beckermann: *Int. J. Cast Metals Res.*, 2007, vol. 20, no. 5, pp. 275-87.

9. O. Yamamoto, H. Yamada, and M. Saito: *Japanese Foundry*, 1978, vol. 50, pp. 14-18.

10. I. Caylek and R. Mahnken: *Int. J. Cast Metals Res.*, 2010, vol. 23, no. 3, pp. 176-84.

11. J. Thole and C. Beckermann: *Int. J. Metalcasting*, 2010, vol. 4, no. 4, pp. 7-18.

12. R. Ami Saada, G. Bonnet, and D. Bouvard: *Int. J. Plasticity*, 1996, vol. 12, no. 3, pp. 273-94.

13. D.Galles and C. Beckermann: *Metall. Mater. Trans. A*, 2016, vol. 47A, pp. 811-29.

14. MAGMASOFT® v4.6, Magma GmbH, Aachen, Germany.

15. J. Miettinen: *Metall. Mater. Trans. B*, 1997, vol. 28, no. 2, pp. 281-97.

16. D. Galles and C. Beckermann: *66th Steel Founders Society of America Technical and Operating Conference*, Paper No. 5.2, Steel Founders' Society of America, Chicago, IL, 2012.

17. K.D. Carlson and C. Beckermann: *Int. J. Cast Metals Res.*, vol. 25, 2012, pp. 75-92.

18. J. Bluhm and R. DeBoer: *ZAMM – J. Appl. Math. Mech.*, 1997, vol. 77, no. 8, pp. 563-77.

19. A.P. Roberts and E.J. Garboczi: *J. American Ceramic Soc.*, vol. 83, no. 12, 2000, pp. 3041-48.

20. R.A. Hardin and C. Beckermann: *Metall. Mater. Trans. A,* 2007, vol. 38A, pp. 2992-3006.

21. C. Monroe: Ph.D. Thesis, University of Iowa, Iowa City, Iowa, 2009.

22. M. Pokorny, C. Monroe and C. Beckermann: *Int. J. Metalcast.*, 2008, vol. 2, no. 4, pp. 41-53.

23. C. Li and B.G.Thomas: *Metall. Mater. Trans. B*, 2004, vol. 35B, pp. 1151-72.

24. ABAQUS®, Abaqus, Inc., Providence, RI.

25. S. K. Saxena, R. K. Reddy and A. Sengupta: *Proceedings of the International Workshop on Constitutive Equations for Granular Non-Cohesive Soils*, pp. 629-45, 1989.

26. A. Hettler and I. Vardoulakis: *Geotechnique*, 1984, vol. 2, pp. 183-98.